

AD-A144 053

TAPERED-WIGGLER FREE-ELECTRON LASER OSCILLATOR PROGRAM

1/2

(U) MATHEMATICAL SCIENCES NORTHWEST INC BELLEVUE WA

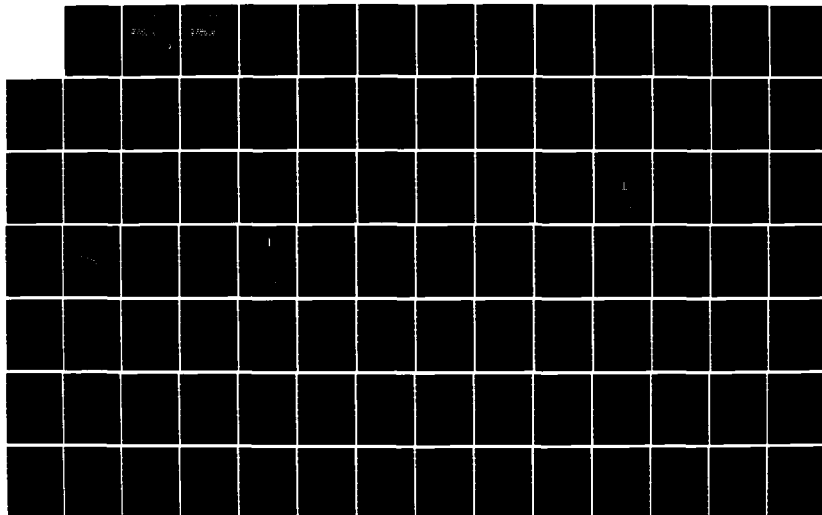
J SLATER ET AL. MAY 84 MSNW-C.11.198.01

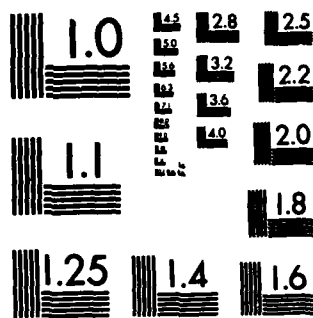
UNCLASSIFIED

AFOSR-TR-84-0623 F49620-01-C-0079

F/G 20/5

NL





MICROCOPY RESOLUTION TEST CHART
NATIONAL BUREAU OF STANDARDS-1963-A

13

AD-A144 053

 **MSNW**

**FINAL REPORT
FOR THE MSNW TAPERED-WIGGLER
FREE-ELECTRON LASER
OSCILLATOR PROGRAM**

DTIC
ELECTE
AUG 9 1984
S **D**
OK **A**

DTIC FILE COPY

Submitted to
AIR FORCE OFFICE OF SCIENTIFIC RESEARCH

Submitted by
**MATHEMATICAL
SCIENCES
NORTHWEST, INC.**

*Approved for Distribution
Distribution unlimited.*

May 1984

84 08 07 141



FINAL REPORT FOR THE MSNW TAPERED-WIGGLER FREE-ELECTRON LASER OSCILLATOR PROGRAM

**Submitted to
AIR FORCE OFFICE OF SCIENTIFIC RESEARCH**

**Submitted by
MATHEMATICAL
SCIENCES
NORTHWEST, INC.**

May 1984

AIR FORCE
NOTICE
Chief, Technical Information Division
MATTHEW J. ...
Chief, Technical Information Division

UNCLASSIFIED

SECURITY CLASSIFICATION OF THIS PAGE (When Data Entered)

REPORT DOCUMENTATION PAGE		READ INSTRUCTIONS BEFORE COMPLETING FORM	
1. REPORT NUMBER AFOSR-TR. 84-0623	2. GOVT ACCESSION NO. A144 033	3. REPORT'S CATALOG NUMBER	
4. TITLE (and Subtitle) Final Report for the MSNW Tapered-Wiggler Free-Electron Laser Oscillator Program		5. TYPE OF REPORT & PERIOD COVERED Final Report	
7. AUTHOR(s) J. Slater, W. Grossman, D. Quimby, A. Vetter, and J. Wilcoxon		6. PERFORMING ORG. REPORT NUMBER C.11.198.01	
9. PERFORMING ORGANIZATION NAME AND ADDRESS Mathematical Sciences Northwest, Inc. 2755 Northup Way Bellevue, WA 98004		8. CONTRACT OR GRANT NUMBER(s) F49620-81-C-0079	
11. CONTROLLING OFFICE NAME AND ADDRESS USAF, AFSC Air Force Office of Scientific Research Bldg. 410, Bolling AFB DC 20332		10. PROGRAM ELEMENT, PROJECT, TASK AREA & WORK UNIT NUMBERS 61102F 2301/A1	
14. MONITORING AGENCY NAME & ADDRESS (if different from Controlling Office) DCASMA Seattle Bldg. 35, Naval Support Activity Seattle, WA 98115		12. REPORT DATE May 1984	
		13. NUMBER OF PAGES 136	
		15. SECURITY CLASS. (of this report) Unclassified	
		15a. DECLASSIFICATION DOWNGRADING SCHEDULE	
16. DISTRIBUTION STATEMENT (of this Report) 16 copies to Directorate of Physical and Geophysical Science Air Force Office of Scientific Research ATTN: NP, Bldg. 410 Bolling AFB DC 20332 Approved for public release; distribution unlimited.			
17. DISTRIBUTION STATEMENT (of the abstract entered in Block 20, if different from Report)			
18. SUPPLEMENTARY NOTES			
19. KEY WORDS (Continue on reverse side if necessary and identify by block number) Free electron laser, oscillator, mode structure, tapered wiggler, diffraction, sideband instability			
20. ABSTRACT (Continue on reverse side if necessary and identify by block number) The purpose of this program is to provide data and analysis for assessing the potential of tapered-wiggler free-electron laser (FEL) oscillators as high- efficiency sources of coherent radiation. It is expected that the tapered- wiggler concept will lead to the development of high-efficiency FELs by provid- ing substantial energy extraction in a single pass of the e-beam through the wiggler magnet. The work consists of parallel experimental and theory tasks. (continued next page)			

DD FORM 1473

EDITION OF 1 NOV 65 IS OBSOLETE

SECURITY CLASSIFICATION UNCLASSIFIED (When Data Entered)

UNCLASSIFIED

SECURITY CLASSIFICATION OF THIS PAGE(When Data Entered)

20. (continued)

The experimental work involves parameterization of the FEL interaction on a single pass basis. Measurements of a net electron energy extraction of 4.2 percent and a peak extraction of 9 percent have been made; these results being the largest net and peak extraction ever achieved using a Compton-regime FEL. Electron energy spectra, extraction as a function of electron beam energy, and extraction as a function of optical power were measured and are consistent with theoretically predicted performance. This work validates the concept of the tapered-wiggler FEL as a high-extraction device and provides data which confirms elements of models used to predict single-pass oscillator performance.

The theoretical work conducted under this program has provided some of the first insight into the transverse-mode structure in tapered-wiggler FEL oscillators. The analysis developed has been applied to the near-concentric cavity geometries of interest for high average power FELs, and has also now been extended to three dimensions. This 3-D model has been used to analyze cavity alignment tolerances including the effects of diffraction. An interesting result of the analysis is the finding that near-concentric FEL cavities can have alignment tolerances which are much less stringent than predicted by geometrical (ray optics) analyses. This is particularly important in view of the extremely small tolerance of the near-concentric cavity.

An additional model has been developed to study longitudinal mode structure. This model is used to study a predicted, but not yet observed, instability known as the sideband instability. This instability is important in that it threatens to limit the electron energy extraction in tapered-wiggler oscillators. Results of this sideband analysis have recently been obtained for parameters appropriate for high-power, visible-wavelength systems. Simulations show sideband growth with associated loss of extraction by one-half or more. The instability can be suppressed, however, by use of frequency-selective optical elements in the laser resonator, with recovery to full extraction.



Accession No.	
NRIC	GRAI <input checked="" type="checkbox"/>
DE	TAB <input checked="" type="checkbox"/>
Unannounced	
Justification	
P-	
Distribution/	
Availability Codes	
Dist	Avail and/or Special
A-1	

UNCLASSIFIED

SECURITY CLASSIFICATION OF THIS PAGE(When Data Entered)

FINAL REPORT
FOR THE MSNW TAPERED-WIGGLER FREE-ELECTRON LASER
OSCILLATOR PROGRAM

Submitted to
AIR FORCE OFFICE OF SCIENTIFIC RESEARCH
AFOSR Contract No. F49620-81-C-0079

By
J. Slater, W. Grossman, D. Quimby, A. Vetter and J. Wilcoxon
MATHEMATICAL SCIENCES NORTHWEST, INC.
2755 Northup Way
Bellevue, Washington 98004

May 1984

TABLE OF CONTENTS

		Page
Section		
1	PROGRAM SUMMARY FOR THE MSNW TAPERED-WIGGLER FEL OSCILLATOR PROGRAM	1-1
	1.1 Overview	1-1
	1.2 Experiment Summary	1-4
	1.3 Transverse-Mode Structure Summary	1-7
	References	1-13
2	SIDEBAND SUPPRESSION SIMULATION	2-1
	2.1 Description of Model	2-2
	2.2 Simulation of Sideband Evolution	2-10
	2.3 Simulation of Sideband Suppression Techniques	2-21
	References	2-27
3	WAVELENGTH-SELECTIVITY OPTIONS	3-1
	3.1 Thin-Film Mirror Coatings	3-1
	3.2 Birefringent Filters	3-8
	3.3 Angularly-Dispersive Elements	3-12
	3.3.1 Grating Design for FEL Applications	3-13
	3.3.2 Production of Concave Blazed Gratings	3-15
	3.3.3 Practical Performance of Interference Gratings	3-17
	3.4 Frequency Selectivity Through a Dispersive Optical Mode Size	3-18
	References	3-25
Appendices		
A	Demonstration of Large Electron-Beam Energy Extraction by a Tapered-Wiggler Free-Electron Laser	
B	Electron-Beam Quality Requirements for Tapered-Wiggler Free-Electron Lasers	
C	Mode Structure of a Tapered-Wiggler Free-Electron Laser Stable Oscillator	
D	Scaling of Alignment Tolerances for Free-Electron Laser Oscillators	
E	Publications and Presentations	

LIST OF FIGURES

Figure		Page
1-1	Extraction as a Function of Input Energy.	1-5
1-2	Extraction as a Function of Laser Power in the Wiggler.	1-6
1-3	Mode Evolution for Various Cavity Lengths and 10 Percent Gain Per Pass.	1-9
1-4	Mode Content Depends on Cavity Length and Gain.	1-10
1-5	One-Way Gain Medium Results in Asymmetric Intensity Distribution Within Wiggler of Near-Concentric Cavity with 10 Percent Gain.	1-12
2-1	Electron Energy Extraction as a Function of Sideband Wavelength for 4 Percent of the Optical Power in a Single, Well Separated Sideband.	2-12
2-2	Time-Dependent Evolution of Optical Spectrum for Long, Highly-Tapered Wiggler.	2-15
2-3	Optical Field Amplitude and Phase at Pass Number 120 Showing Modulation Due to Sideband Instability.	2-17
2-4	Power Level as a Function of Time for the Simulation Shown in Figure 2-2.	2-18
2-5	Extraction as a Function of Time Showing Loss of Extraction as Sidebands Grow After Main Line Achieves Trapping.	2-19
2-6	Extraction Degradation Due to Sidebands.	2-20
2-7	Wavelength Selectivity Function Used to Model Performance of (a) Birefringent Filter and (b) Multilayer Dielectric Coating for Sideband Suppression.	2-22
2-8	Comparison of Quasisteady State Optical Spectra (at Pass Number 300) for Cases With and Without Wavelength Selectivity.	2-23
2-9	Introduction of Wavelength Selectivity Eliminates Loss of Extraction Efficiency Due to Sidebands.	2-25
3-1	Dependence of Coating Reflectivity on Ratio of High Index to Low Index Ratio (n_H/n_L) for a Ten Period $3/4$ -Wave Stack.	3-4

3-2	Dependence of Reflectivity and Bandwidth on Number of Periods N for $ZrO_2 + SiO_2$ Quarter-Wave Stack.	3-5
3-3	Dependence on Reflectivity on Film Thickness for $ZrO_2 + SiO_2$ Ten Period Stack.	3-6
3-4	Five Period Edge Filter Design for Two Layer Thicknesses of $ZrO_2 + SiO_2$.	3-7
3-5	Orientation of Tilted Birefringent Plate in FEL Cavity.	3-9
3-6	Birefringent Plate Transmission Functions for Various Plate Thicknesses, t .	3-11
3-7	Illustration of Diffraction Grating Used in Littrow Mounting.	3-14
3-8	Calculation of FEL Gain in a Near-Concentric Cavity with Variable Mode Size.	3-20
3-9	Near-Concentric Cavity Geometry for Use of Dispersive Lens for Mode Size Variation.	3-22
3-10	Calculation of Net FEL Gain Variation Due to Change in Mode Size.	3-23

LIST OF TABLES

Table		Page
2-1	Preliminary Point Design for Visible Oscillator Experiment	2-13
3-1	Parameters of Gain Calculation with Variable Mode Size	3-21

Section 1

PROGRAM SUMMARY FOR THE MSNW TAPERED-WIGGLER FEL OSCILLATOR PROGRAM

1.1 OVERVIEW

The basic goal of this program is to provide data and analysis for assessing the potential of the tapered-wiggler⁽¹⁻¹⁾ FEL oscillator as a high-efficiency source of coherent radiation. The advantage of the tapered-wiggler FEL, as compared to the original⁽¹⁻²⁾ fixed pitch device demonstrated at Stanford, is that of high electron kinetic-energy extraction in a single pass. It is expected that the tapered-wiggler concept will lead to development of high-efficiency free-electron lasers if an e-beam recovery stage is added downstream of the wiggler.

The fact that large deceleration of electrons could be achieved with a tapered-wiggler design was first demonstrated in the Mathematical Sciences Northwest/Boeing Aerospace Company program, and since then MSNW/BAC have measured⁽¹⁻³⁾ extraction as large as 4 percent in an amplifier configuration, and recently 1 percent has been realized⁽¹⁻⁴⁾ in oscillators. The amplifier gain is too low to be of practical interest, hence realistic systems will probably be configured as high-extraction oscillators. There is therefore incentive to determine whether the oscillator can be made to work at extraction comparable to that achieved in amplifier experiments. This AFOSR program is directed toward bridging the gap between the current single pass measurements and high-extraction oscillators. It embodies complementary experimental and theoretical tasks which are intended to assess oscillator potential in the near term using single-pass data.

The experimental task involves measurement of the FEL interaction as a function of several basic parameters for the purpose of verifying understanding of the basic interaction. These parameterization experiments

were completed for high optical flux conditions with measurements of extraction as a function of electron beam energy and extraction as a function of optical power. The data obtained confirms elements of models used to predict single-pass oscillator performance.

The theoretical work conducted under this program has provided some of the first insight into the transverse-mode structure in tapered-wiggler FEL oscillators. The analysis developed has now been applied to the near-concentric cavity geometries of interest for high average power FELs, and also extended to three dimensions. This 3-D model has been used to analyze cavity alignment tolerances including the effects of diffraction. An interesting result of the analysis is the finding that near-concentric FEL cavities can have alignment tolerances which are much less stringent than predicted by geometrical (ray optics) analyses. This is particularly important in view of the extremely small tolerance of the near-concentric cavity.

An additional model has been developed to study longitudinal mode structure. This model is used to study a predicted, but not yet observed, instability known as the sideband instability.⁽¹⁻⁵⁾ This instability is important in that it threatens to limit the electron energy extraction in tapered-wiggler oscillators. The sideband instability results from a resonance between the rocking frequency of electrons in the ponderomotive potential well, and the beat wave produced from the optical wave and its sidebands. The sideband modulates the optical wave in such a manner as to increase the amplitude of the rocking in the potential well, leading eventually to detrapping. Results of this sideband analysis have recently been obtained for parameters appropriate for high-power, visible-wavelength systems. Simulations show sideband growth with associated loss of extraction by one-half or more. The instability can be suppressed, however, by use of frequency-selective optical elements in the laser resonator, with recovery of full extraction.

The remainder of Section 1 contains a brief summary of the experimental work, its interpretation, and the transverse-mode modeling. Details of these topics have been published, and for convenience these publications are included in this report as appendices. Appendix A describes the MSNW/BAC single-pass amplifier experiment used for the parameterizations. The model developed to fit the parameterizations is described in Appendix B. Appendix C contains the transverse-mode analysis, and the use of that analysis to identify diffractive effects on cavity alignment tolerances is given in Appendix D. Publications and presentations resulting from research conducted under this contract are listed in Appendix E.

The longitudinal-mode analysis used for the sideband instability work has not yet been published, and is described in detail in Section 2 of this report. In addition to the modeling, practical considerations for providing frequency selectivity in FEL optical cavities are addressed in Section 3.

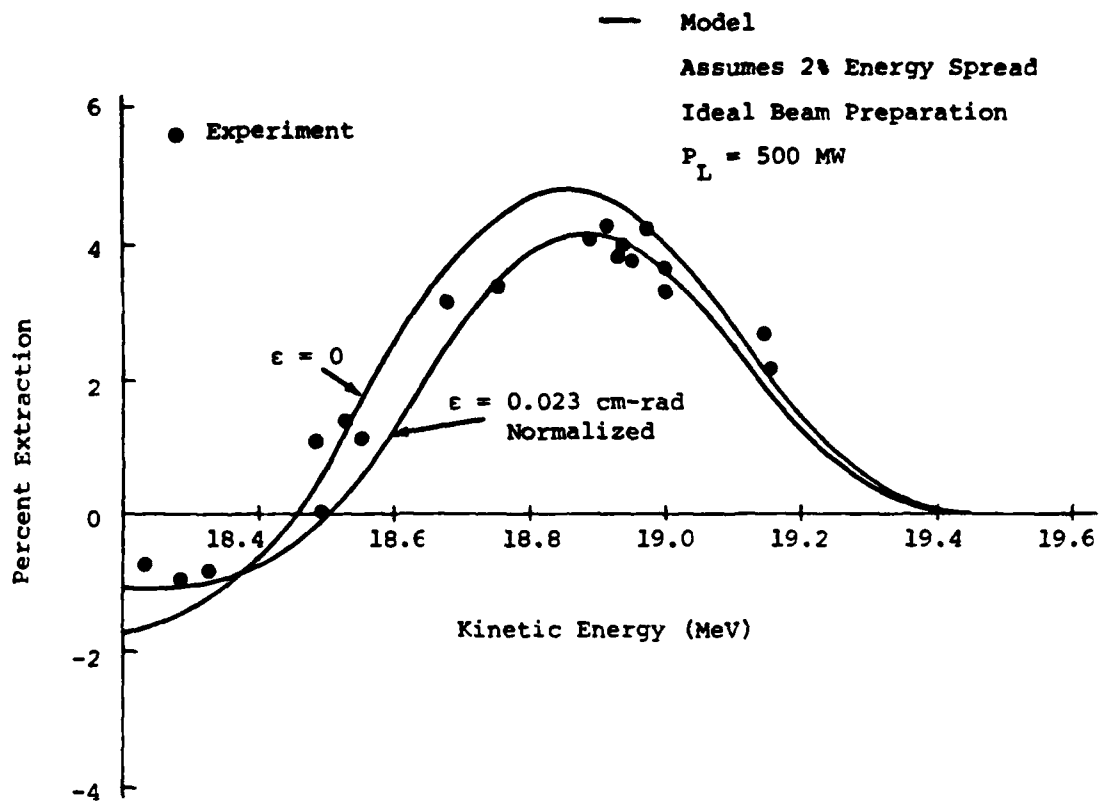
Section 2 deals with development of the basic numerical model of the instability and calculation of suppression afforded by various cavity schemes. The calculations differ from others in that the case of long length wigglers and long electron micropulse length is treated, these being the most probable parameters for near-term visible-wavelength high-extraction systems. The suppression calculations are made for both edge and bandpass filter functions of various slopes, and show the degree of filtering necessary to achieve a given suppression.

Section 3 is a discussion of wavelength-dispersive optical elements. One straightforward approach considered is the use of wavelength-selective dielectric coatings on the end mirrors. Another promising technique involves insertion of a birefringent filter into the cavity. Spatially-dispersive schemes are also considered. This includes gratings and a novel approach based on optical mode size variation with wavelength.

1.2 EXPERIMENT SUMMARY

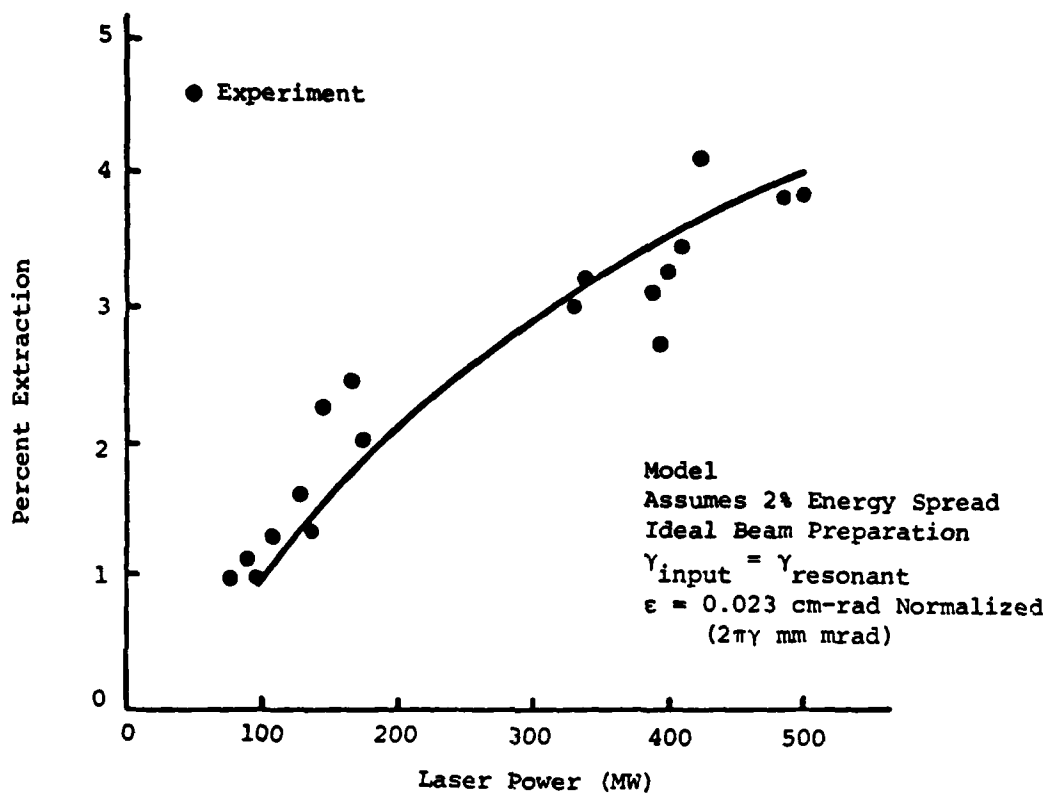
The experimental tasks involve parameterization of the FEL interaction in terms of parameters useful to oscillator calculations. Single pass measurements of the variation of the FEL interaction, with respect to photon intensity and photon wavelength, have been made at high flux levels using the MSNW/BAC 10 μm amplifier hardware.⁽¹⁻³⁾ The wavelength parameterization is necessary because of an expected tendency of tapered-wiggler devices to chirp during start-up, and it has been measured on a single-pass basis not by variation of wavelength, but by variation of the electron energy. The interaction can be measured in terms of either the net electron energy loss or equivalently the photon gain. Measurement of the energy loss has been made over a range of photon intensities spanning the onset of trapping to saturation.

The parameterizations obtained are shown in Figures 1-1 and 1-2. The electron energy extraction, as a function of e-beam energy, is shown in Figure 1-1. Peak extraction is observed near 19 MeV. When the electron energy is detuned below 18.4 MeV, net acceleration of the electrons is seen. Electron deceleration and energy extraction is observed over a 3 percent range in energy, corresponding to a 6 percent equivalent range in the optical spectrum. The data are in good agreement with the theoretical curves drawn, under the assumption of perfect focusing, perfect alignment, and a diffraction-limited optical beam. Emittance (defined as $\gamma\pi r\theta$) values of 0 and 0.023 cm-rad are used. The latter value is consistent with the estimated combined effect of emittance and misalignment. The energy scale of the theoretical curves has been downshifted 1.5 percent to provide an improved fit. This shift is within the uncertainty of the electron spectrograph calibration. The points shown do not include all the data taken. With misalignment, poor focusing, or other problems, it is always possible to achieve results in which the extraction values are low, but it is not possible to achieve extraction results that are artificially high except by actual measurement errors.



83 07026

Figure 1-1. Extraction as a Function of Input Energy.



83 07035

Figure 1-2. Extraction as a Function of Laser Power in the Wiggler.

Electron energy extraction has also been measured as a function of laser power as shown in Figure 1-2. The extraction is seen to increase with laser power as expected. The onset of trapping is predicted at roughly 50 MW, and the trapping fraction increases steadily to about 60 percent at 500 MW. The data shown is taken from three time-resolved electron energy spectrum records. Since the laser power is also measured as a function of time, it is a simple matter to determine extraction as a function of power. Again, perfect focusing and alignment are assumed for the theoretical curve, and a 0.023 cm-rad normalized emittance is used as a rough estimate of combined emittance and misalignment effects. When the calculation is repeated with zero emittance, the result is a curve parallel to that shown and about 1 percent higher extraction.

1.3 TRANVERSE-MODE STRUCTURE SUMMARY

The FEL requires good transverse optical mode quality to provide a uniform, high photon intensity within the wiggler and thereby maximize the interaction with the electrons. In addition, production of a nearly diffraction-limited beam will imply good output beam quality. Recent calculations of mode evolution in injected linear cavities are summarized as follows. The code numerically solves Maxwell's equations for cylindrically-symmetric geometries. It allows one to follow development of the mode structure of the tapered-wiggler oscillator, starting with an initial injected wave at saturation intensity. This injected wave develops over many round trips of the optical cavity according to the influence of the FEL interaction, diffraction, and interaction with other elements of the optical cavity. The e-beam radius is typically less than that of the photon beam and the size mismatch drives higher order modes in addition to TEM_{00} . Of additional interest is the effect of apertures on the mode structure, especially those associated with the wiggler magnets. E-field truncation at the ends of the wiggler causes mode-dependent cavity losses which of course are higher for higher-order modes. The truncation also causes mode mixing, which transfers power from low to high order modes. Optimization studies have shown that the minimum wiggler bore, consistent

with acceptable distortion due to clipping, yields the largest FEL interaction.

Evolving phase and amplitude profiles of the optical beam are calculated by direct integration of Maxwell's equations with the electrons providing the driving term. A convenient tool for understanding this evolution is the projection of the optical wave into normal modes of the optical cavity. That is, the fraction of total optical power in any particular cavity mode can be observed as a function of the round-trip number. One sees, for example, that a pure TEM_{00} wave injected into the optical cavity at the start of the calculation evolves an appreciable fraction of TEM_{10} mode over the course of several round trips. This mode mixing is caused primarily by the nonuniform gain medium, and to a lesser extent, by the presence of the wiggler entrance and exit apertures.

The mode evolution during the first 35 round trips after TEM_{00} mode injection is shown in Figure 1-3 for three different cavity lengths, each with 10 percent output coupling. Higher-order mode content is especially evident in confocal cavities (those with mirror separation equal to the radius of curvature), and concentric cavities (those with mirror separation equal to twice the radius of curvature). These cavities can support unusual mode structure because the relative phase slippage between cavity modes over one round trip is an integral multiple of 2π , allowing constructive interference between higher-order modes produced on each round trip. As the cavity length is changed away from the confocal or concentric condition without changing the degree of mode selectivity due to aperturing, the fraction of TEM_{10} mode decreases dramatically.

Significant higher order mode content may also be found in high-gain systems. As shown in Figure 1-4, higher gain systems will tend to exhibit unusual mode structure even at intermediate cavity lengths. Systems with high steady-state gain also have large output coupling and therefore have a short ring down time. Constructive interference between higher-order modes

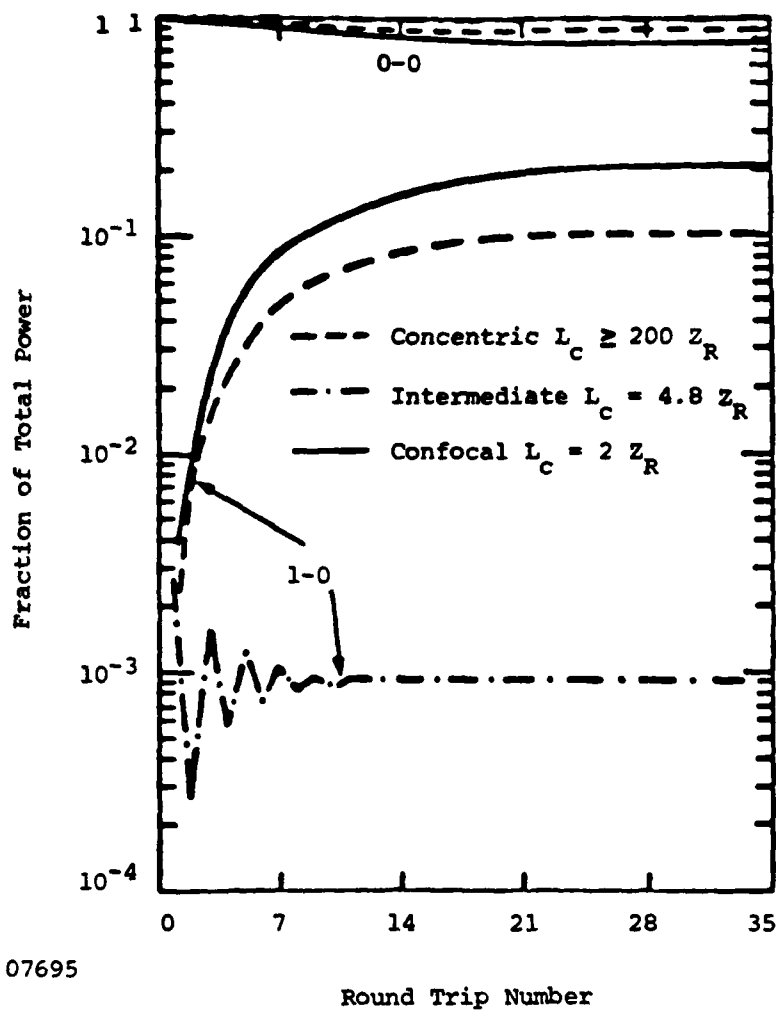


Figure 1-3. Mode Evolution for Various Cavity Lengths and 10 Percent Gain Per Pass.

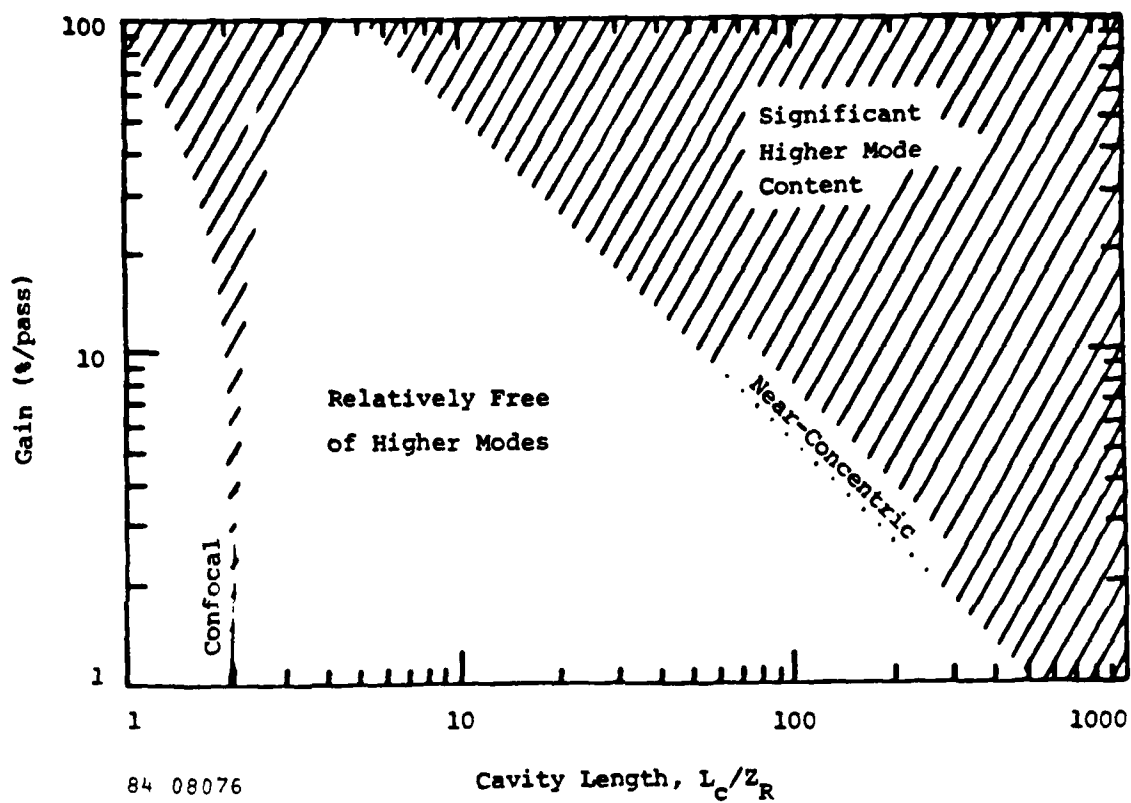


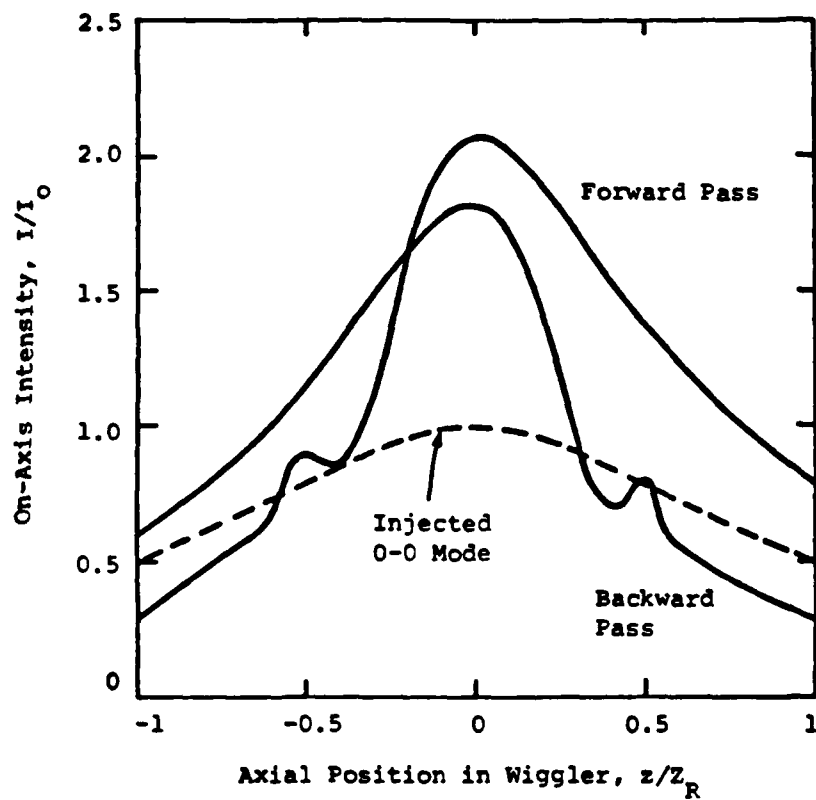
Figure 1-4. Mode Content Depends on Cavity Length and Gain.

produced over many round trips is not required for significant higher-order mode content in these systems.

Figure 1-5 compares the steady-state on-axis intracavity photon intensity with that of the initially injected TEM_{00} mode in a near-concentric cavity. High average power FELs with linear cavities require near-concentric cavities due to mirror loading. The rapid variations in intensity are due to diffraction effects from the truncation at the ends of the wiggler. The truncation occurs at radius $h = 1.8 w$, where w is the $1/e$ point in E-field for a TEM_{00} wave at the aperture. The TEM_{10} mode content results in the striking asymmetry between the forward and backward moving waves in the wiggler. Such an asymmetry can be supported in the FEL since the gain mechanism is active in one direction only.

The quality of the output beam is excellent for each of the cases studied, being of nearly diffraction-limited quality. This result is somewhat surprising in view of the TEM_{10} mode content which complicates the intracavity structure, but in reality the higher-mode content is an indication of mode mismatch within the cavity, rather than wave front aberration. For the example shown in Figure 5, the focused output beam has a Strehl ratio of about 98 percent.

A three-dimensional version of this wave front propagation analysis has been developed and can be used for mode analysis similar to that shown previously, but additional important effects such as misalignment can be included. In addition, the 3-D code provides for analysis of complex cavities such as ring cavities employing glancing-incidence mirrors intended for use at high average power. Results of including diffraction in mirror alignment tolerance analysis of linear cavities are given in Appendix D. Tolerance to cavity misalignment is generally studied with geometrical optics codes, but the low Fresnel number FEL cavities are dominated by diffraction and one finds that the alignment tolerances do not follow conventional rules based on ray tracing.



83 07694

Figure 1-5. One-Way Gain Medium Results in Asymmetric Intensity Distribution Within Wiggler of Near-Concentric Cavity with 10 Percent Gain.

REFERENCES

- 1-1. N.M. Kroll, P.L. Morton, and M.N. Rosenbluth, "Variable Parameter Free Electron Laser," in Free-Electron Generators of Coherent Radiation, Physics of Quantum Electronics, Vol. 7, S.F. Jacobs, H.S. Pilloff, M. Sargent, M.O. Scully, and R. Spitzer, eds., (Addison-Wesley, 1980), p. 89.
- 1-2. D.A.G. Deacon, L.R. Elias, J.M.J. Madey, G.J. Ramian, H.A. Schwettman and T.I. Smith, "First Operation of a Free-Electron Laser," Phys. Rev. Lett., 38, 892 (1977).
- 1-3. W.M. Grossman, J.M. Slater, D.C. Quimby, T.L. Churchill, J. Adamski, R.C. Kennedy, and D.R. Shoffstall, "Demonstration of Large Electron-Beam Energy Extraction by a Tapered-Wiggler Free-Electron Laser," Appl. Phys. Lett., 43, 745 (1983).
- 1-4. C.A. Brau, LANL, private communication, and J.A. Edighoffer, G.R. Neil, C.E. Hess, T.I. Smith, S.W. Fornaca, and H.A. Schwettman, "Variable-Wiggler Free-Electron Laser Oscillation," Phys. Rev. Lett., 52, 344 (1984).
- 1-5. N.M. Kroll and M.N. Rosenbluth, "Sideband Instabilities in Trapped Particle Free-Electron Lasers," in Free-Electron Generators of Coherent Radiation, Physics of Quantum Electronics, Vol. 7, S.F. Jacobs, H.S. Pilloff, M. Sargent, M.O. Scully, and R. Spitzer, eds. (Addison-Wesley, 1980), p. 147.

Section 2

SIDEBAND SUPPRESSION SIMULATION

A simulation model has been developed for study of the potentially serious Raman sideband instability first described by Kroll and Rosenbluth.⁽²⁻¹⁾ The instability is characterized by development of longitudinal amplitude and phase modulation in the optical pulse due to the generation of new frequency components or "sidebands" in the laser spectrum. The instability is expected to become evident in FEL oscillators at optical powers high enough to trap electrons in the ponderomotive potential well of the FEL interaction, because synchrotron oscillations of trapped electrons lead to axial modulation of the gain.

The instability is predicted to result in a loss of electron trapping efficiency in multi-pass FELs using highly-tapered wigglers. Simulations of untapered wigglers^(2-2,2-3) show that the sideband instability actually leads to enhanced extraction by promoting chirp to the frequency of peak saturated gain. But tapered wigglers rely upon trapping of electrons in decelerating ponderomotive potential wells to achieve enhanced extraction efficiency. Highly-tapered wigglers trap the electrons for many synchrotron periods. The sideband instability can cause detrapping within a distance as short as one synchrotron period, thus potentially leading to severe loss of extraction in highly-tapered systems.

This study has provided the first simulation of the time-dependent sideband evolution for parameters of a visible long-pulse tapered-wiggler FEL oscillator, where there are three or more synchrotron periods within the wiggler length. Simulations show sideband growth with associated loss of extraction efficiency by one-half or more. The same simulation shows that the instability can be suppressed by use of frequency-selective elements in the optical cavity, with full recovery of the extraction efficiency. These analyses will be highly relevant for interpretation of

experimental results as they become available and for guidance of future oscillator design work.

2.1 DESCRIPTION OF MODEL

The mathematical basis for the sideband instability has been summarized by Goldstein and Colson.⁽²⁻²⁾ The electron motion in the ponderomotive well, for small deviations from the resonant phase and an unmodulated E-field, may be described by a harmonic oscillator equation. This implies that such electrons might be expected to couple to light whose wavelength λ'_s is slightly shifted from the original resonant wavelength λ_s :

$$\lambda'_s = \lambda_s \left[1 \pm \frac{\lambda_w}{L_{sy}} \right], \quad [2-1]$$

where λ_w is the wiggler wavelength, L_{sy} is the spatial period of the harmonic behavior for an electron near the bottom of the bucket

$$L_{sy} = \lambda_w \left[\frac{\pi [1 + a_w^2]}{2\lambda_s G a_w e_s \cos \psi_r} \right]^{1/2}, \quad [2-2]$$

$G = J_0(y) - J_1(y)$ is the coupling factor for a planar wiggler given by the difference between two Bessel function factors, $y = a_w^2/2(1+a_w^2)$, ψ_r is the synchronous phase angle for trapped electrons

$$\psi_r = \sin^{-1} \left[\frac{e_s^*}{e_s} \right], \quad [2-3]$$

and the optical electric field amplitude E_0 and peak wiggler magnetic field B_0 are measured by (cgs units)

$$e_s = \frac{eE_o}{2^{1/2} m_o c^2} , \quad [2-4]$$

and

$$a_w = \frac{eB_o \lambda_w}{2^{3/2} \pi m_o c^2} , \quad [2-5]$$

respectively. The quantity e_s^* is the minimum E-field for electron trapping

$$e_s^* = \frac{\lambda_w \left[1 + a_w^2 \right]}{2 \lambda_s G_a L_w} \left[\frac{\Delta \gamma_r}{\gamma_r} \right] \quad [2-6]$$

for a wiggler of resonant energy γ_r , fractional energy taper $\Delta \gamma_r / \gamma_r$, and length L_w . In actuality, many electrons undergo large amplitude phase oscillations, which means that their motion is described by a more complex nonlinear pendulum equation. Such electrons couple to a continuum of light waves of different frequencies close to that given by Equation [2-1]. Kroll's analysis⁽²⁻¹⁾ predicts a spectrum of unstable waves with the largest growth rates for waves satisfying Equation [2-1] with the positive sign. Thus one expects gain for lower frequency sidebands (longer wavelengths) and absorption for higher frequencies. Another way to describe this phenomenon is that light at λ_s is Raman shifted to $\lambda_s' > \lambda_s$ along with excitation of increased sloshing of electrons in the ponderomotive well.

The spatial modulation period, λ_m , associated with generation of a sideband satisfying Equation [2-1] is given by

$$\lambda_m = \lambda_s \left[\frac{L_{sy}}{\lambda_w} \right] . \quad [2-7]$$

This is to be compared with the slippage distance

$$s = \lambda_s \left[\frac{L_w}{\lambda_w} \right] \quad [2-8]$$

which is the distance by which a resonant electron slips back relative to a plane wave in one transit through the wiggler. Most previous simulations of sideband evolution⁽²⁻⁴⁾ have observed initial onset of modulation with a period approximately equal to the slippage distance, which corresponds to a synchrotron period comparable to the wiggler length. Evidently sideband growth does not occur until the optical power grows to the point where the synchrotron period becomes comparable to or shorter than the wiggler length. The fractional frequency shift of the sideband is then of order $1/N$, where N is the number of wiggler periods. These simulation studies have considered short, mildly-tapered wigglers in which there is only about one synchrotron period within the wiggler length.

Linearly-tapered wigglers may be characterized by the single dimensionless parameter^(2-5,2-6)

$$\delta = 4\pi N \frac{\Delta\gamma}{\gamma_r} \quad [2-9]$$

This work differs from others primarily in that we consider a long, highly-tapered wiggler appropriate for a high-efficiency visible-wavelength FEL, for which $\delta \approx 125\pi$. This is an order of magnitude larger than the mildly-tapered wigglers of $\delta \leq 15\pi$ for which simulations of time-dependent oscillation behavior for long electron pulses have previously been presented in the literature.^(2-7,2-8) Examination of Equations [2-2], [2-3], and [2-6] reveals that the number of synchrotron periods within the wiggler length is given by

$$N_{sy} = \left[\frac{\delta}{4\pi^2 \tan \psi_r} \right]^{1/2} \quad [2-10]$$

Thus we see that at any given resonant phase angle ($\psi_r \approx 40$ degrees maximizes the product of electron trapping fraction and deceleration rate per unit E-field⁽²⁻⁹⁾), the wiggler considered in this study has roughly three times as many synchrotron periods within the wiggler length. For

such long, highly-tapered wigglers, the fractional frequency shift of the sideband given in Equation [2-1] will be approximately

$$\frac{\Delta\lambda_s}{\lambda_s} = \frac{N_{sy}}{N} \quad [2-11]$$

Time-dependent sideband evolution in longer, more highly-tapered wigglers has previously been simulated,⁽²⁻¹⁰⁾ but only under the assumption of an electron pulse length comparable to or shorter than the slip length. The codes used may be applied to the much longer pulse experiments of interest to DOD goals in which the pulse length is 20 or more slippage distances,⁽²⁻⁷⁾ but the computer time requirements are very large. In this work, we consider very long pulses by use of periodic boundary conditions^(2-3,2-8) to examine the pulse modulation. The periodic boundary condition model allows treatment of a short section of much longer electron and optical pulses, thus greatly reducing computer time requirements.

The modulation of the optical pulse is studied directly in the space-time domain. The one-dimensional model for the time-dependent evolution of the optical field modulation is developed under the assumptions of a plane-polarized tapered wiggler field

$$B = B_0(z) \cos k_w z \quad [2-12]$$

and diffraction-limited plane-polarized optical field

$$E_x = E_0(r,z) \cos[k_s z - \omega_s t + \phi_0(r,z) + \phi(z)] \quad [2-13]$$

Arbitrary wiggler tapering is provided by prescribing the axial variation in the magnetic field amplitude B_0 . The spatial variation in amplitude and phase for a TEM_{00} beam of Rayleigh range Z_R focused at the wiggler center is given by the functions⁽²⁻¹¹⁾

$$e_s = e_{s0}(z) e^{-(r/w)^2} \left[\frac{w_0}{w} \right] \quad [2-14]$$

$$\phi_0 = \left(\frac{r}{w}\right)^2 \left[\frac{z}{z_R} - q\right] - \tan^{-1} \left[\frac{z}{z_R} - q\right], \quad [2-15]$$

where $q = L_w/2z_R$, z is measured from the wiggler entrance, the $1/e$ amplitude radius of the beam is

$$w = w_0 \left[1 - \left[\frac{z}{z_R} - q\right]^2\right]^{1/2}, \quad [2-16]$$

and

$$w_0 = \left[\frac{\lambda_s z_R}{\pi}\right]^{1/2}. \quad [2-17]$$

Optical field evolution due to the FEL interaction is included by the axial variation in the E-field amplitude e_{s0} and phase ϕ explicitly shown in the equations.

The electron beam is assumed to also be axisymmetric and to have a parabolic density profile

$$n_e = \frac{2I}{ce\pi r_{eb}^2} \left[1 - \left[\frac{r}{r_{eb}}\right]^2\right], \quad [2-18]$$

where I is the beam current and r_{eb} is the beam radius. The parabolic density profile is a close approximation to the distribution resulting from uniformly-filled emittance phase space. The beam radius is related to the normalized emittance $\epsilon_N = \gamma\pi r\theta$ by

$$r_{eb} = \left[\frac{\epsilon_N}{\gamma\pi k_\beta}\right]^{1/2}, \quad [2-19]$$

where

$$k_{\beta} = \frac{a k_w}{2^{1/2} \gamma}$$

[2-20]

is the wavenumber for betatron oscillations resulting from distributed two-plane focusing⁽²⁻¹²⁾ in the wiggler.

Electron energy spread and emittance are important effects which tend to reduce the FEL interaction strength for the visible FEL parameters considered here.⁽²⁻¹²⁾ Energy spread can be included directly in the model by introducing a dispersion of the initial energies of the sample electrons used to drive the optical wave. However, it is not possible to directly include transverse beam effects such as emittance in a 1-D axial model. E-beam emittance results in loss of interaction strength due to introduction of both effective electron energy spread and less than ideal overlap of the electron and photon beams. For the conditions considered here, loss of overlap is of far more significance than effective energy spread.⁽²⁻¹²⁾ Consequently, effective energy spread has been neglected but overlap effects have been included in an approximate way using appropriate weighted averages. The column-averaged E-field amplitude and phase seen by the e-beam are given by

$$e_{sa} = \frac{\int_0^{r_{eb}} e_s(r, z) n_e(r) 2\pi r dr}{\int_0^{r_{eb}} n_e(r) 2\pi r dr} \quad [2-21]$$

$$= \frac{2e_{so} w_o w}{r_{eb}^2} \left[1 - \left(\frac{w}{r_{eb}} \right)^2 \left[1 - e^{-[r_{eb}/w]^2} \right] \right]$$

$$\phi_{oa} = \frac{\int_0^{r_{eb}} \phi_o(r, z) n_e(r, z) 2\pi r dr}{\int_0^{r_{eb}} n_e(r) 2\pi r dr} \quad [2-22]$$

$$= \frac{1}{3} \left[\frac{r_{eb}}{w} \right]^2 \left[\frac{z}{z_R} - q \right] - \tan^{-1} \left[\frac{z}{z_R} - q \right] .$$

In the limit of zero e-beam radius, e_{sa} reduces to $e_{so} w_o / w$. The Lorentz force equation describing the motion of a sample electron in the ponderomotive potential well formed by the wiggler and optical fields may be written in terms of the column-averaged quantities

$$\frac{d\gamma}{dz} = \frac{-Ge_{sa} a_w}{\gamma} \sin [\psi + \phi + \phi_{oa}] \quad [2-23]$$

$$\frac{d\psi}{dz} = k_w - \frac{k_s}{2\gamma^2} \left[1 + a_w^2 \right] , \quad [2-24]$$

where $\psi = (k_w + k_s)z - \omega_s t$ is the phase of the electron relative to a plane wave.

The evolution of the optical wave is determined based on the self-consistent interaction with a number of sample electrons. The sample electrons are injected into the wiggler on each pass uniformly distributed in ψ and distributed in γ according to the energy spread of the electron beam. In the slowly varying phase and amplitude approximation, (2-13) the driven wave equation, in a reference frame moving with the photons, reduces to

$$\frac{de_{so}}{dz} = \frac{2eGa_w If}{m_o c^3 r_{eb}^2} \left\langle \frac{\sin [\psi + \phi + \phi_{oa}]}{\gamma} \right\rangle \quad [2-25]$$

$$e_{so} \frac{d\phi}{dz} = \frac{2eGa_w}{m_o c r_{eb}} \frac{If}{\gamma^2} \left\langle \frac{\cos [\psi + \phi + \phi_{oa}]}{\gamma} \right\rangle, \quad [2-26]$$

where f is a geometrical "fill factor"

$$f = \frac{2 r_{eb}^2}{w_o^2} \left\langle \frac{e_{sa}}{e_{so}} \right\rangle \quad [2-27]$$

$$= 4 \left[\frac{w}{w_o} \right] \left[1 - \left[\frac{w}{r_{eb}} \right]^2 \left[1 - e^{-[r_{eb}/w]^2} \right] \right]$$

and the averages indicated by the angular brackets are made over the set of sample electrons.

We study the evolution of a long optical pulse by considering a length W near the center of the pulse and imposing periodic boundary conditions at each end. The window width is chosen to be at least as long as the slip length, since this is an important characteristic distance in the problem. Because of the periodic boundary conditions, the optical pulse may be decomposed into a set of discrete optical frequencies. The choice of the width of the window between the periodic boundaries and the number of spatial grid points within the window, N_p , defines the discrete frequencies which are handled in the model.

$$\frac{\Delta \lambda_s}{\lambda_s} = \pm \frac{ns}{NW} \quad n = 0, 1, 2, 3, \dots, N_p/2. \quad [2-28]$$

The center wavelength is taken to be the resonant wavelength, defined to be

$$\lambda_r = \frac{\lambda_w}{2\gamma_o} \left[1 + a_{wo}^2 \right], \quad [2-29]$$

where γ_o is the mean initial electron energy and a_{wo} is the a_w value at the wiggler entrance. For a window width of one slip length and a system

with four synchrotron periods along the wiggler length, the sideband may be expected to be separated from the main line by four of the discrete frequency intervals. Longer windows provide better frequency resolution at the expense of increased computer time requirements.

The electron slippage is included by allowing the sample electrons to drift across the optical field window as the electron and optical pulses propagate down the wiggler. In accordance with the periodic boundary condition model, those electrons which slip out of one side of the window reappear at the opposite side of the window. In order to simplify the bookkeeping, the rate of slippage for all electrons is taken to be the rate for a resonant electron. This approximation neglects the actual distribution of electron axial velocities, which may be fairly appreciable in a tapered wiggler. The difference in slippage lengths between trapped and untrapped electrons, for example, is

$$\frac{\Delta s}{s} = \frac{\Delta \gamma}{\gamma} \frac{r}{r} . \quad [2-30]$$

For the cases shown here, the taper is about 10 percent. Nevertheless, this approximation appears to be acceptable considering that untrapped particles appear to play a very minor role in the sideband instability.

Evolution of the modulation due to the sideband instability is studied by solving the driven wave equation within the window over many passes through the oscillator. After each pass the E-field amplitude is renormalized to account for round-trip losses such as output coupling. After many passes the optical pulse reaches a steady state in which the single-pass gain equals the losses.

2.2 SIMULATION OF SIDERAND EVOLUTION

Oscillators incorporating long, highly-tapered wigglers can be expected to be subject to somewhat more severe detrapping should sidebands

appear, since there is more opportunity for the instability to drive sloshing in the potential well. Figure 2-1 presents results of an early study to evaluate the possible extraction degradation, should sidebands appear. This calculation is not self-consistent in that it does not predict the magnitude or wavelength offset of the sidebands. It is simply assumed that a single, well-separated sideband is present at a very modest power level, 4 percent of the power at the carrier frequency. The E-field of the sideband is then 20 percent of the carrier E-field. Figure 2-1 shows the electron energy extraction as a function of the wavelength offset of the sideband, calculated for a single pass through each of two wigglers of different length. For the longer wiggler, a very distinct resonance is found, which occurs for a sideband wavelength offset of approximately

$$\frac{\Delta\lambda_s}{\lambda_s} = \frac{\lambda_w}{L_{sy}} \quad [2-31]$$

This offset is at a frequency which causes the modulation due to the sideband to be in phase with the synchrotron oscillations of trapped electrons and is in agreement with the predicted sideband offset given in Equation [2-9]. The instability has a finite bandwidth because of the range of synchrotron periods due to anharmonicity of the bucket and the range of a_w and e_g values within the wiggler. E-field phase modulation due to the sideband results in side-to-side motion of the ponderomotive well. In the longer wiggler, the shaking of the well induces large amplitude sloshing of trapped electrons, causing detrapping and the loss of extraction shown. The parameters assumed for the longer wiggler in this calculation are very similar to those of the preliminary design of a high-extraction visible oscillator experiment described in Table 2-1.

These calculations give an indication of the possible serious impact of the sideband instability for conditions of a visible-wavelength tapered-wiggler FEL. With as little as 4 percent of the total optical power in the sideband, the extraction could be lowered from the design value of 5 percent to a value of only 3 percent. But these calculations are not self-

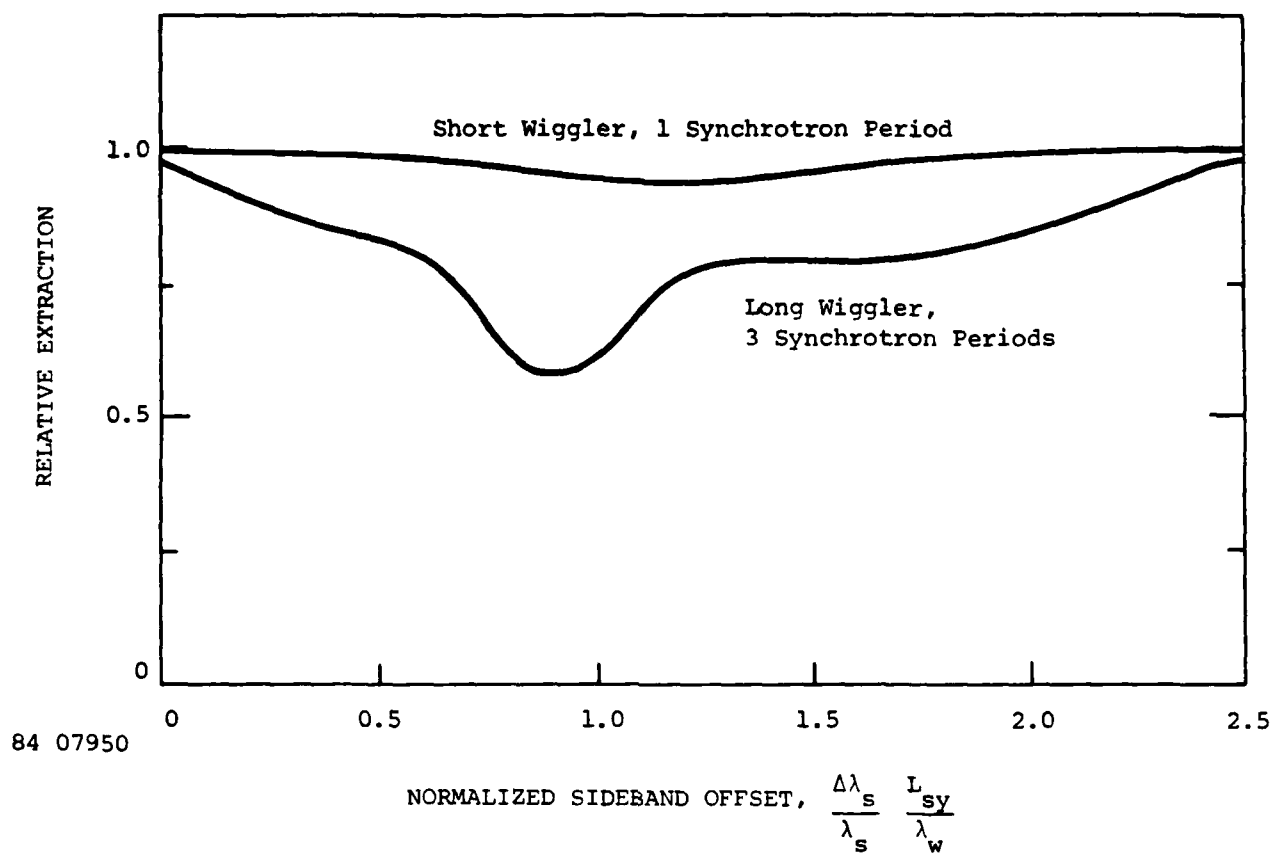


Figure 2-1. Electron Energy Extraction as a Function of Sideband Wavelength for 4 Percent of the Optical Power in a Single, Well Separated Sideband. $\Psi_r = 36^\circ$

Table 2-1

PRELIMINARY POINT DESIGN FOR VISIBLE
OSCILLATOR EXPERIMENT

Electron Beam

Initial Energy	120 MeV
Peak Current	>100 A
Pulse Length	25 ps

Wiggler

Length	5 m
Taper ($\Delta\gamma/\gamma$)	12 Percent
Wavelength	2.02 cm
Peak Field Strength	10.0 T
a_w	1.33

Optical Cavity

Resonant Wavelength	0.5 μ m
Rayleigh Range	2.4 m
Length	60 m
Outcoupling	Variable

Derived Quantities^(a)

Slippage Lengths per Pulse	65
E-field for 5 percent Extraction, e_s	20 cm ⁻¹
Photon Power for 5 Percent Extraction	3.3 GW
Synchrotron Period at 5 Percent Extraction	1.34 m
Expected Number of Modulation Periods per Slip Distance	3.7
Expected Frequency Offset of Sideband	1.5 Percent

(a) Without allowance for emittance and energy spread.

consistent in that they do not include the influence of the electron dynamics on the optical E-field evolution.

Results of a calculation of the self-consistent evolution of the optical spectrum for the parameters of Table 2-1 are shown in Figure 2-2. In this simulation the electron beam is assumed to be of ideal quality, that is, energy spread and emittance are neglected. The simulation assumes an electron beam current of 200 A and round-trip cavity losses (output coupling) of 10 percent. The wiggler taper consists of a 0.75 m uniform section followed by a 4.25 m linearly-tapered section of 12.5 percent resonant energy change. The inclusion of a short constant section in the wiggler prescription allows enhancement of the small-signal gain to above the saturated gain level at the expense of a modest reduction in small-signal linewidth. The power levels shown on the figure refer to the instantaneous power of the optical pulse within the cavity. The initial optical field is arbitrary. To roughly approximate the initial incoherent properties of the E-field, the simulation is initiated with all possible frequencies present, but randomly phased with respect to each other. The simulation is seeded at a power level of approximately 1 watt per frequency channel, which is representative of the spontaneous emission power level. Use of various representations of the initial spectrum result in somewhat different details in the spectral evolution but do not change the qualitative results. A window width of twice the slippage distance and 64 spatial grid points are used in the simulation. The simulation is thus conducted within a frequency bandwidth of approximately 12 percent full width.

After a number of passes through the oscillator, the laser picks a narrow line from the initial seed. The frequency and shape of the line is consistent with the small-signal gain curve, as shown in Figure 2-2. The power level of this line exponentiates at the small-signal gain rate of about 65 percent per pass. As the power level approaches saturation, the line chirps slightly by growth of the longer wavelength wing of the line. Upon reaching a power level of several GW, sufficient to trap electrons, an

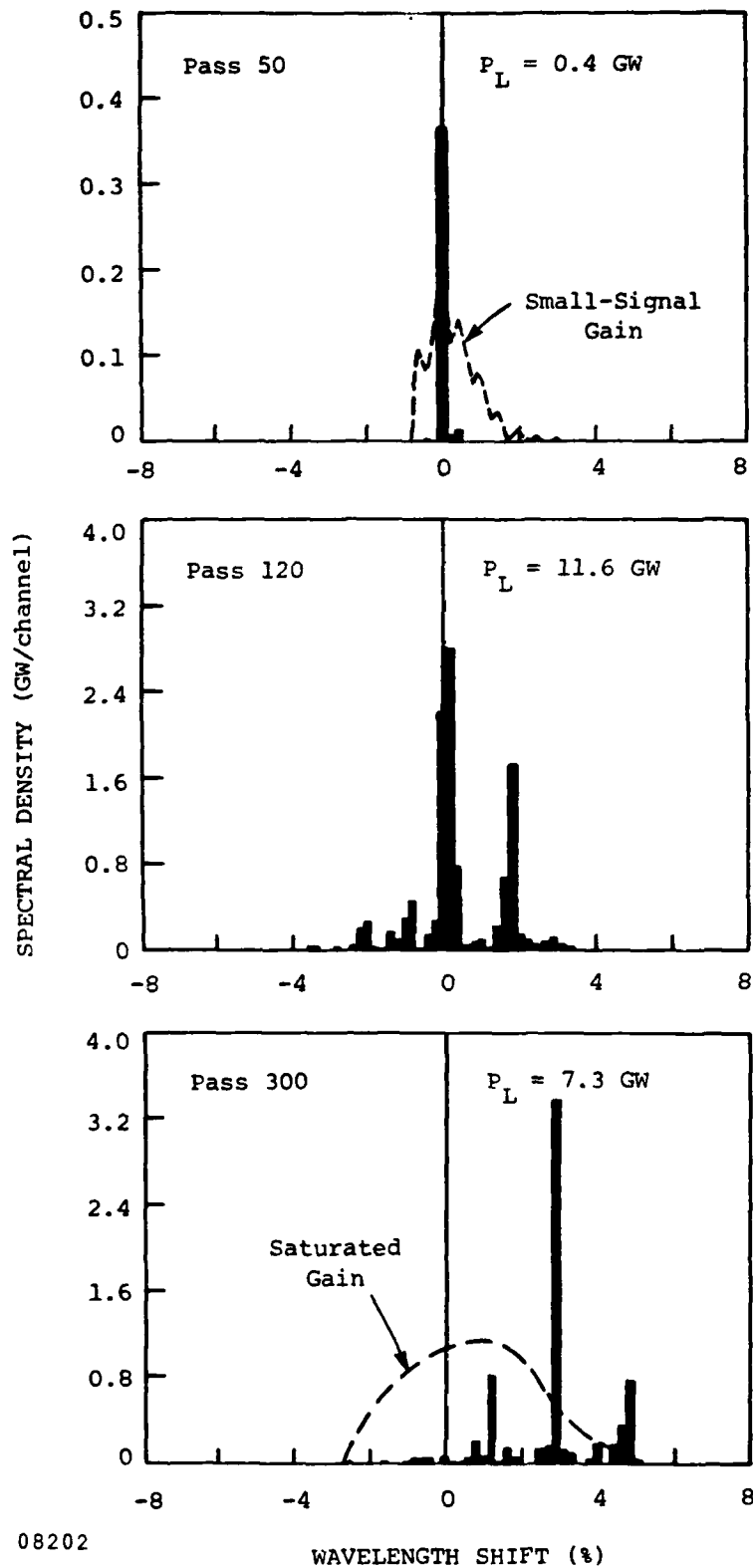


Figure 2-2. Time-Dependent Evolution of Optical Spectrum for Long, Highly-Tapered Wiggler. Simulation parameters given in Table 2-1. $I = 200\text{A}$, 10 percent output coupling.

upper sideband begins to form. By pass number 120, shown in Figure 2-2, the sideband has grown to the point where the electron trapping efficiency is seriously degraded. The sideband offset of about 1.5 percent is consistent with the number of synchrotron periods (~ 4) at this power level. As predicted by Kroll,⁽²⁻¹⁾ the upper sideband is dominant, although both upper and lower spectral features appear. The E-field amplitude and phase modulation due to the sideband is shown in Figure 2-3. The modulation period is about one-fourth the slippage distance which is consistent with Equation [2-7]. The sidebands continue to evolve to higher wavelength and the spectrum develops multiple features.

The buildup of the sideband results in a loss of trapping efficiency and a corresponding decay of the laser power. As shown in Figure 2-4, a true steady state is not reached. The laser reaches an oscillatory quasi-steady state in which it vacillates around an average power of about 7 GW. The power oscillations correspond to slow growth and decay of various spectral features. The extraction efficiency as a function of time is shown in Figure 2-5. The loss of extraction upon buildup of the sideband instability is clearly shown in the figure. The extraction efficiency in quasi-steady state averages about 3 percent, considerably lower than the ideal value of about 7 percent which would be obtained if the laser were operating with a narrow line at the frequency of peak gain. As may be seen by comparison with the saturated gain curve for a single narrow line of equal power shown in Figure 2-2, the operating spectrum is not only complex but at a longer than optimum wavelength.

Results of a study of the degradation of extraction efficiency due to the sidebands as a function of output coupling is shown in Figure 2-6. There are a range of output couplings for which the laser will evolve to power levels sufficient for trapping. The ideal extraction efficiency at saturation for operation with a single narrow line which is allowed to chirp is indicated by the solid line. When the effect of the sidebands is included, the extraction is reduced to approximately 40 percent of the

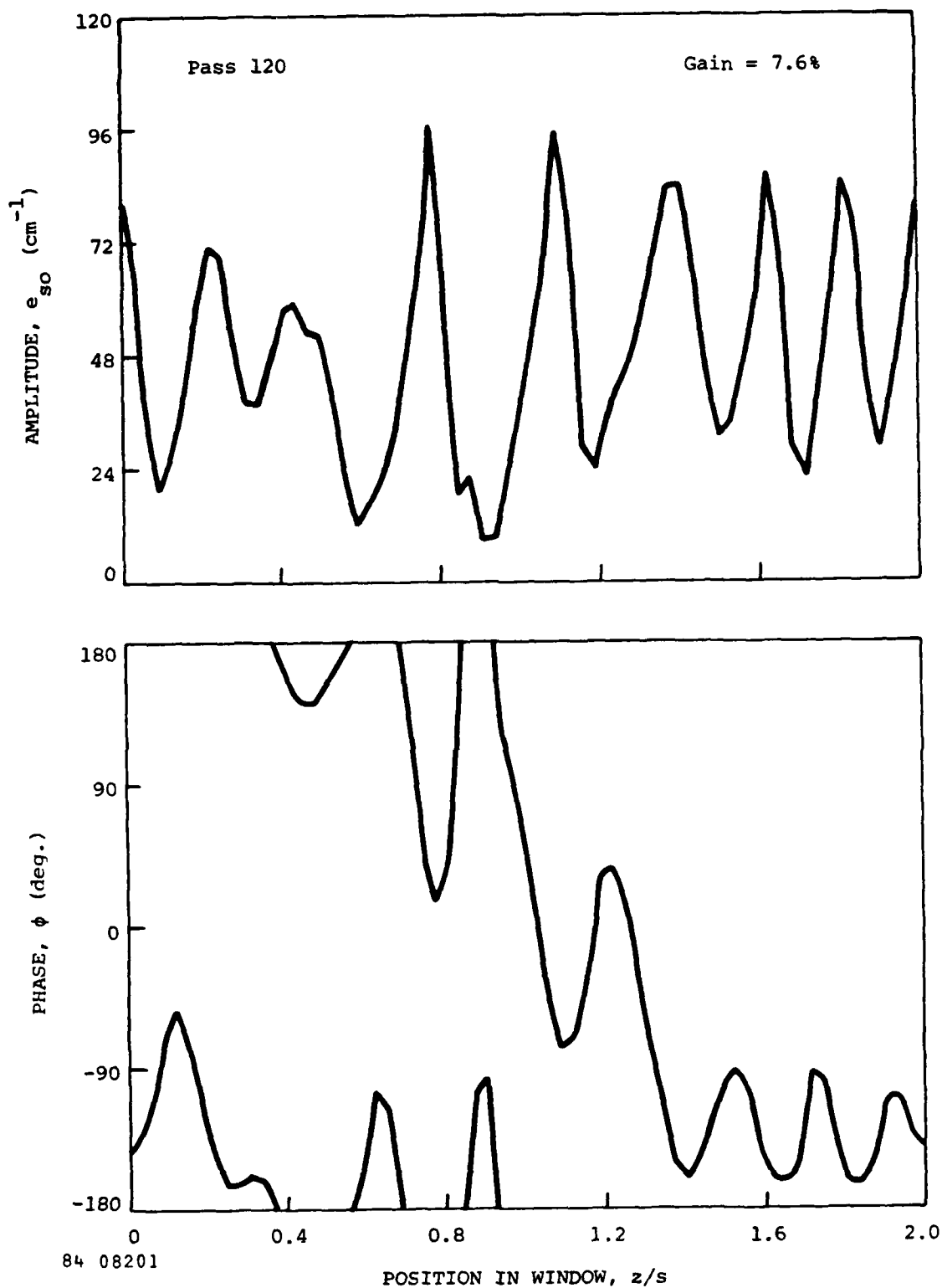


Figure 2-3. Optical Field Amplitude and Phase at Pass Number 120
Showing Modulation Due to Sideband Instability.

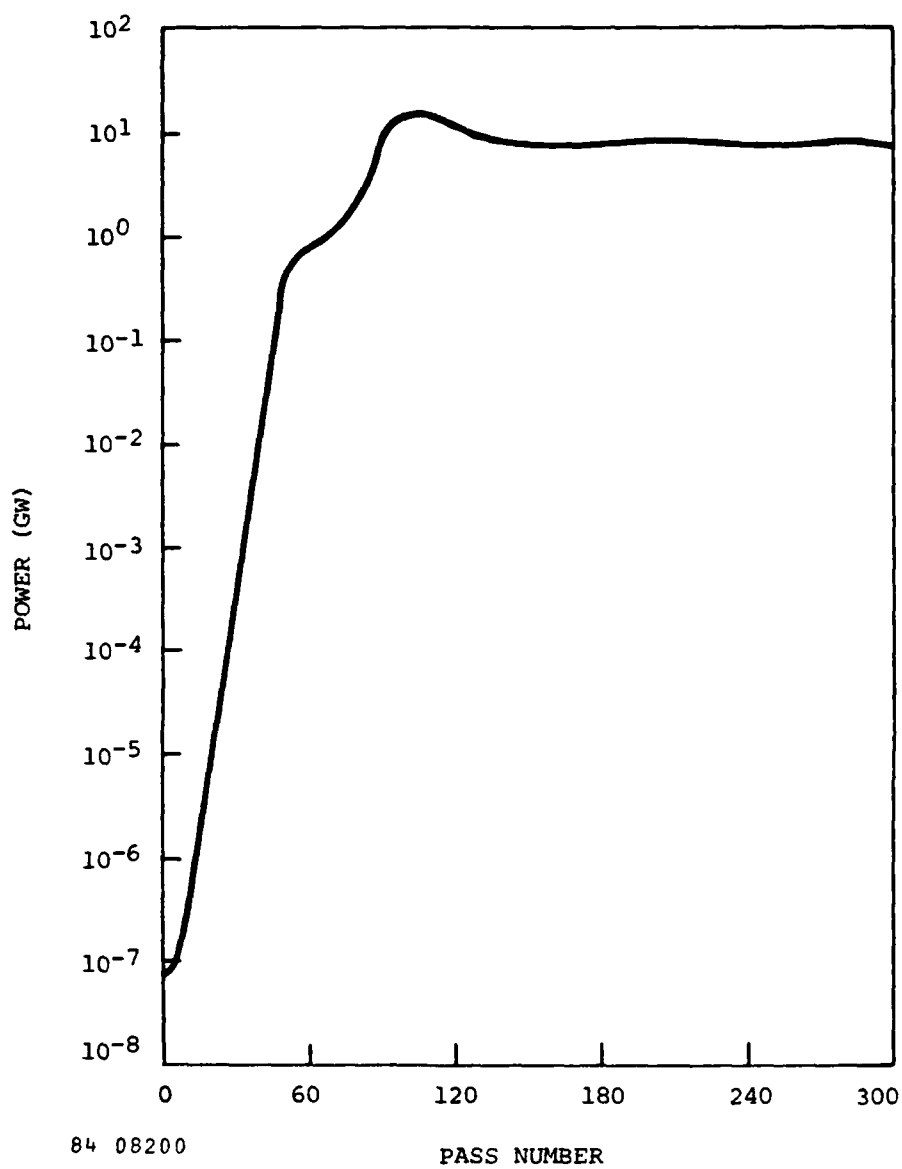
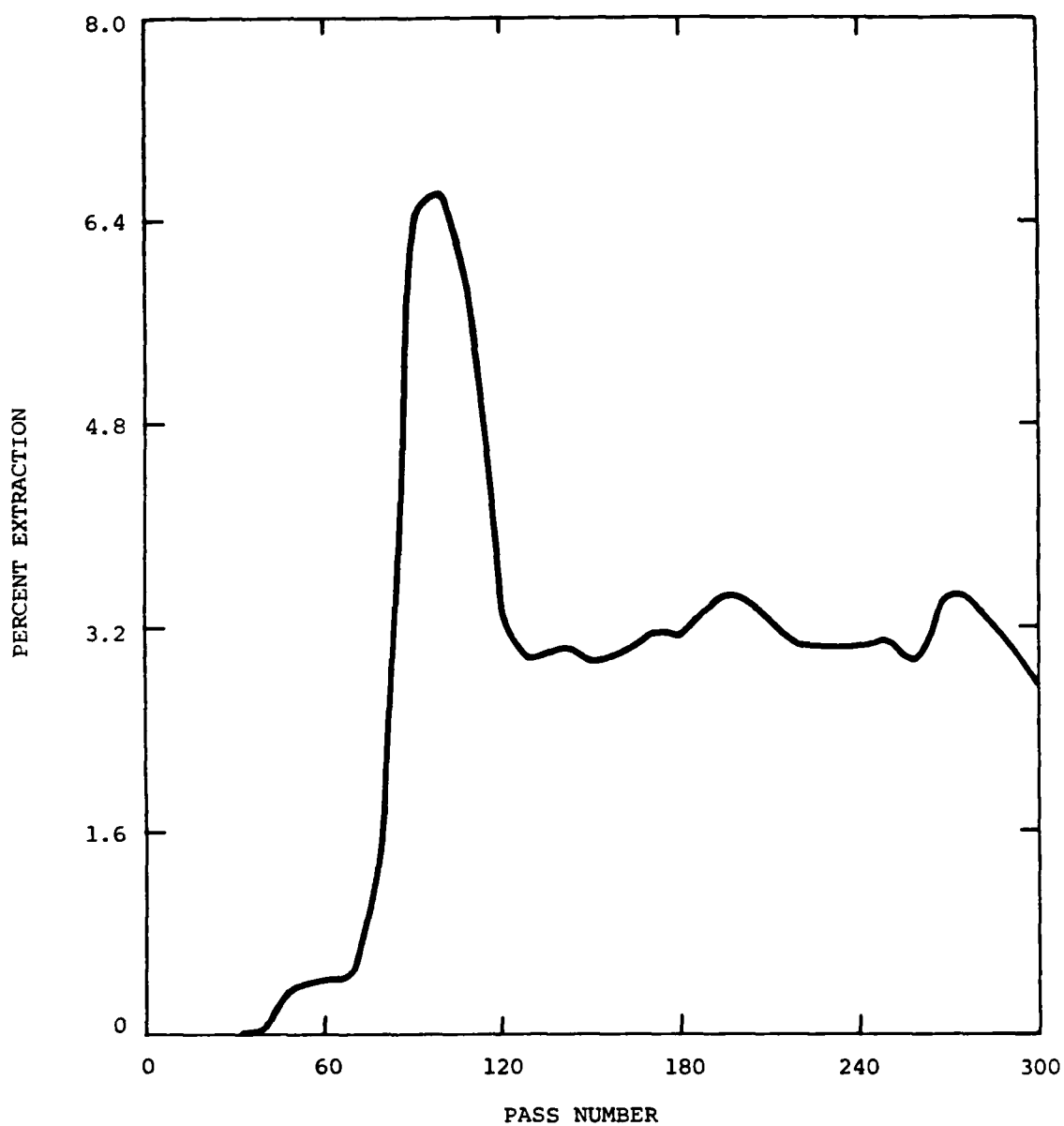


Figure 2-4. Power Level as a Function of Time for the Simulation Shown in Figure 2-2.



84 08199

Figure 2-5. Extraction as a Function of Time Showing Loss of Extraction as Sidebands Grow After Main Line Achieves Trapping.

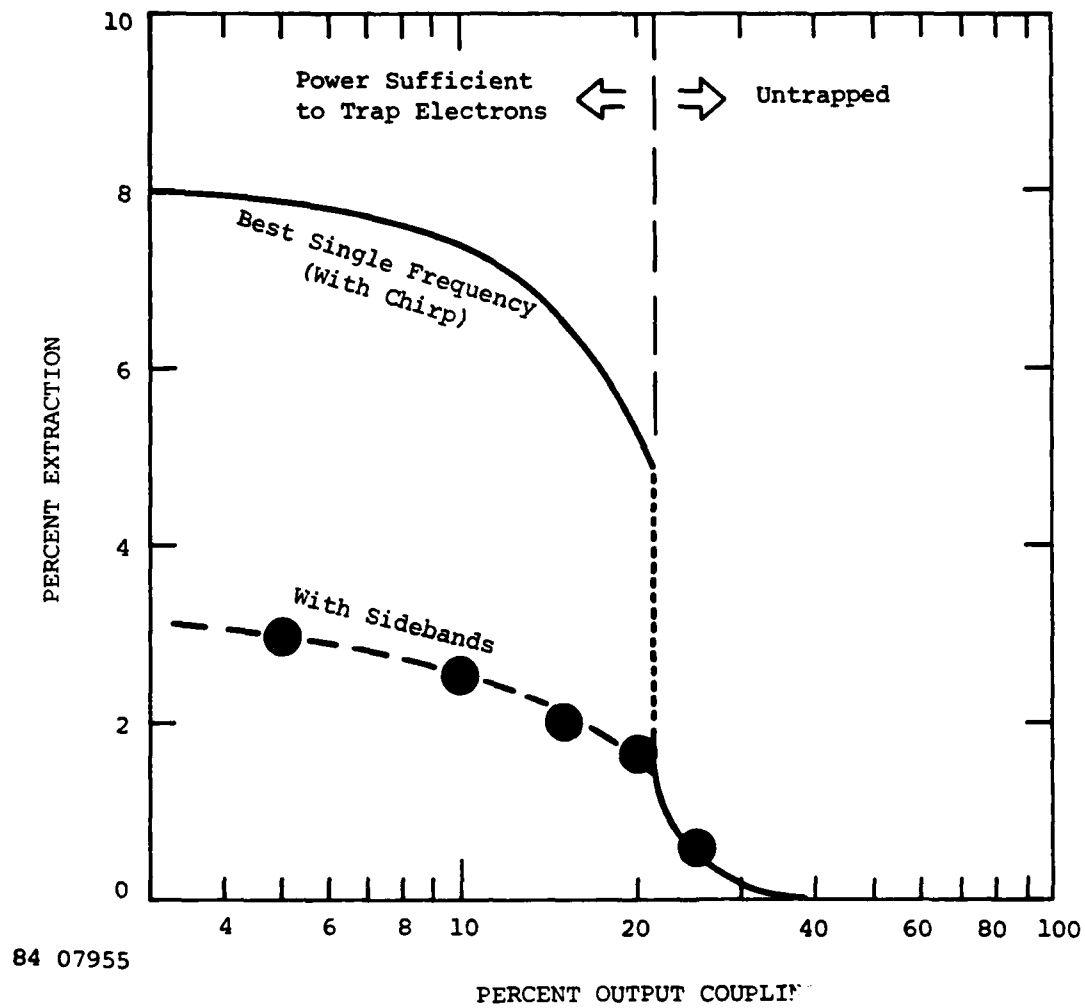


Figure 2-6. Extraction Degradation Due to Sidebands.

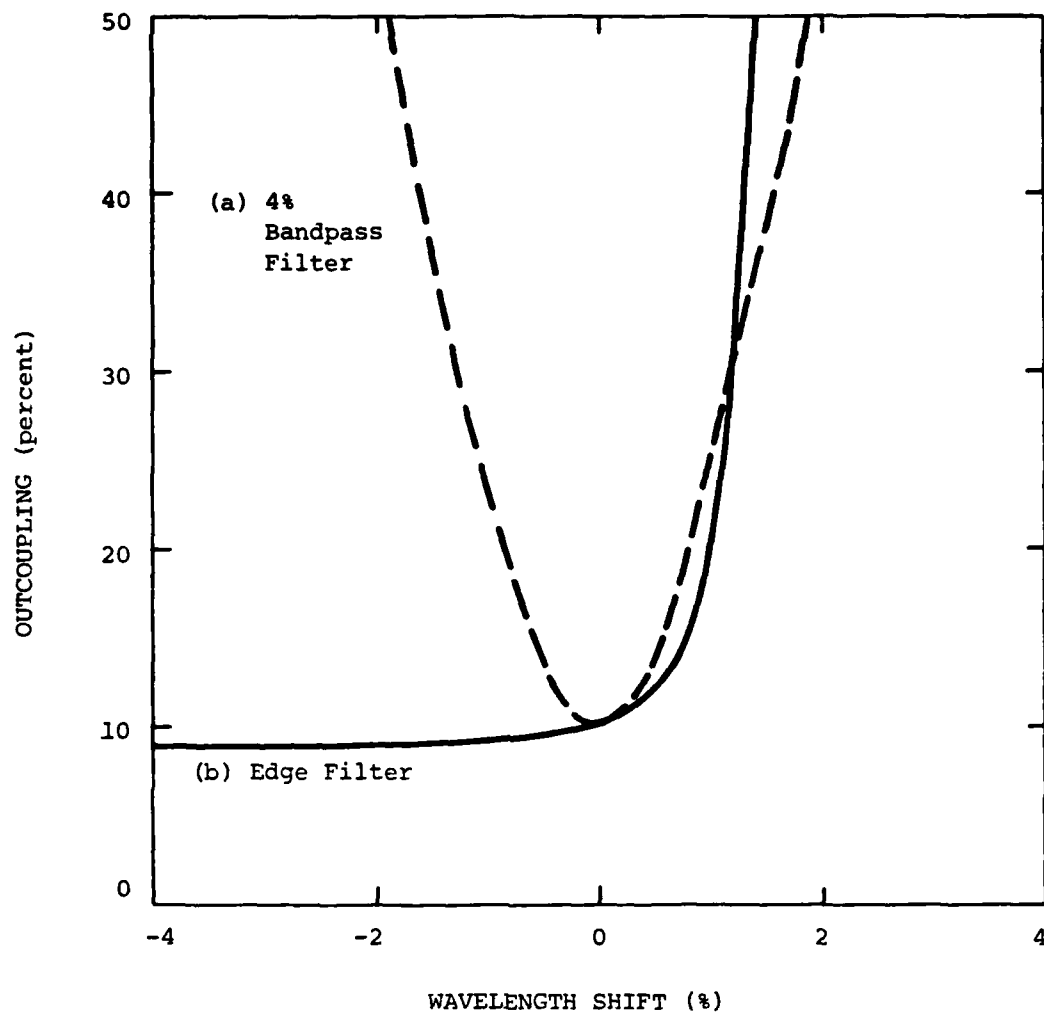
expected value. Of course, sidebands do not form for output couplings which are too high to allow the laser to achieve trapping.

2.3 SIMULATION OF SIDEBAND SUPPRESSION TECHNIQUES

The model of sideband evolution allows study of sideband suppression techniques. Kroll originally suggested⁽²⁻¹⁾ that the addition of electron energy spread would reduce the sideband growth rate since the growth rate depends on the details of the phase space distribution of electrons trapped in the potential well. Simulations have indeed shown⁽²⁻²⁾ that large initial energy spread reduces the growth rate but does not eliminate the instability. Here we investigate the possibility of totally eliminating sideband activity by use of a dispersive element in the optical cavity to provide wavelength selectivity.

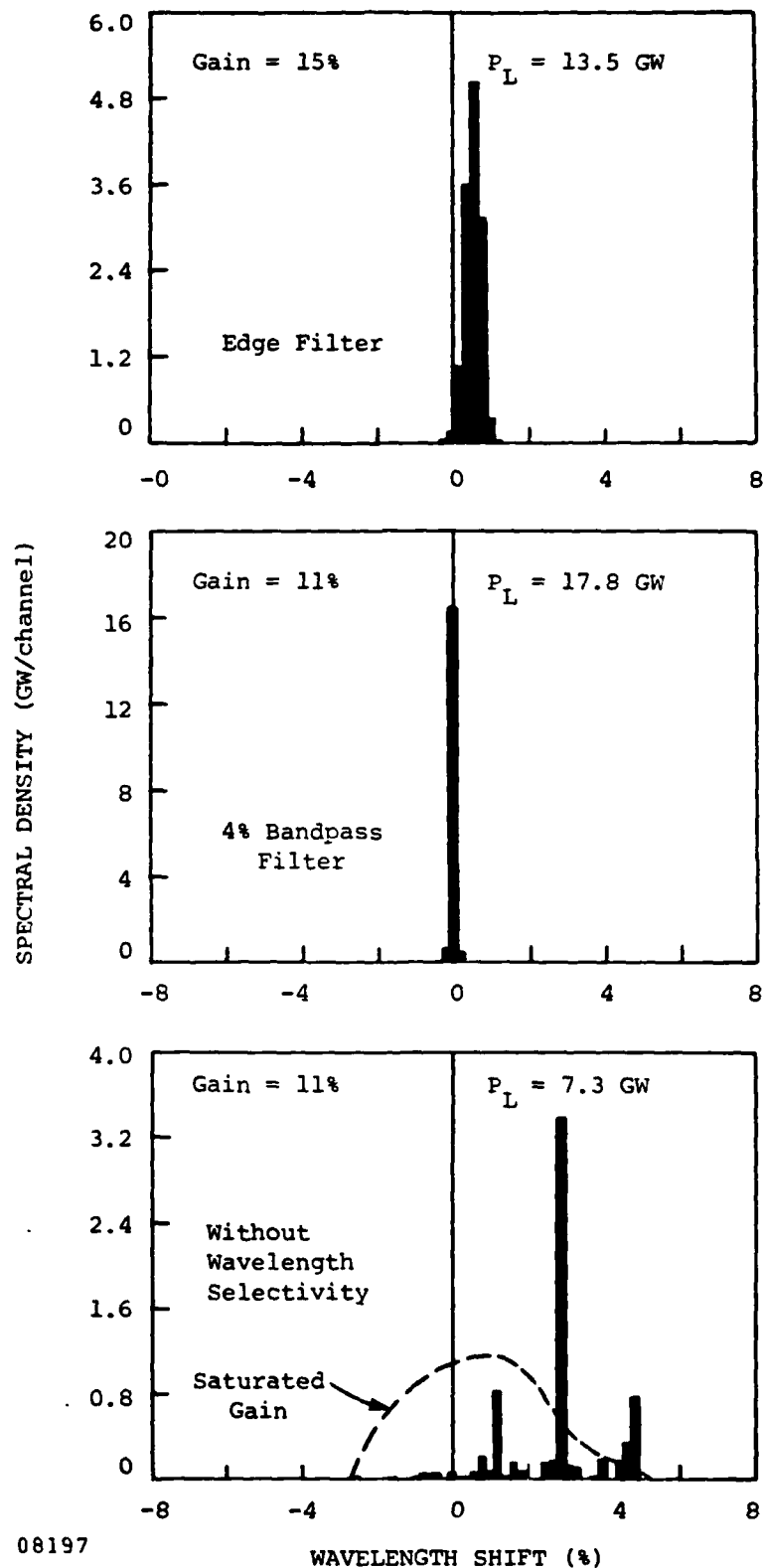
A number of possible schemes for provision of wavelength selectivity are considered in Section 3. As an example of the performance of these techniques, the simulation shown in Figures 2-2 through 2-5 has been repeated including optical filters in the cavity. Figure 2-7 shows the filter functions assumed in the two example calculations. The round-trip cavity loss on the main line is retained at 10 percent. In Case (a) of Figure 2-7, a 4 percent bandpass filter is placed in the cavity. We define the bandwidth to be the width at the 50 percent loss points. The $\sin^2(\lambda_g)$ dependence of the cavity loss is characteristic of that produced by a birefringent filter. In Case (b), an edge filter is used with a cutoff at longer wavelengths. The edge filter function corresponds to the wavelength selectivity possible by operation of the laser near the edge of a 10 percent bandpass filter produced by a multilayer dielectric mirror coating. In both cases the selectivity functions are configured in such a way that the losses are large at the sideband wavelength offset of 1.5 percent (4 to 5 times the loss on the main line).

Results of these simulations are compared in Figure 2-8. Both filters successfully eliminate the sideband instability. The optical



84 08198

Figure 2-7. Wavelength Selectivity Function Used to Model Performance of (a) Birefringent Filter and (b) Multilayer Dielectric Coating for Sideband Suppression.



84 08197
 Figure 2-8. Comparison of Quasisteady State Optical Spectra (at Pass Number 300) for Cases With and Without Wavelength Selectivity.

spectra at pass number 300 are very narrow compared to the case with no frequency selectivity. Furthermore, the operating wavelength is approximately the wavelength of peak saturated gain, rather than overshooting to longer wavelengths. Consequently, the laser saturates at a much higher power level and the extraction efficiency, as shown in Figure 2-9, evolves to over 7 percent, representing very efficient electron trapping. In the case of the edge filter, the temporary drops in extraction shown in the figure correspond to chirp of the laser spectrum from one discrete frequency to another. This temporary extraction loss is believed to be a nonphysical result due to the limited frequency resolution of the model.

An additional simulation was also conducted using a birefringent filter function with a full width of 6 percent. In this case the initial sideband in the simulation of Section 2.2 lies well within the bandwidth of the cavity. The loss at the sideband frequency is 2.5 times that of the main line. It is found that these losses are not sufficient to suppress all sideband activity and restore full extraction efficiency. Evidently a cavity with strong dispersion is required for the FEL parameters studied here.

In the case of the 4 percent bandpass filter, the operating wavelength stays fixed at the startup wavelength. The line does not chirp due to the rather steep rise in loss to either side of the main line. In the case of the edge filter, the losses at first rise more slowly with increasing wavelength, allowing the line to chirp about 0.6 percent in wavelength. This operating point is more nearly the point of peak saturated gain. In fact, in this case the laser picks an operating point with about 13 percent output coupling rather than the nominal 10 percent.

The best choice of a filter shape depends on several factors. Modeling predicts that many tapered-wiggler FEL designs will require substantial wavelength chirp during the transition from small-signal to saturated operation, so in that case the filter function must be configured

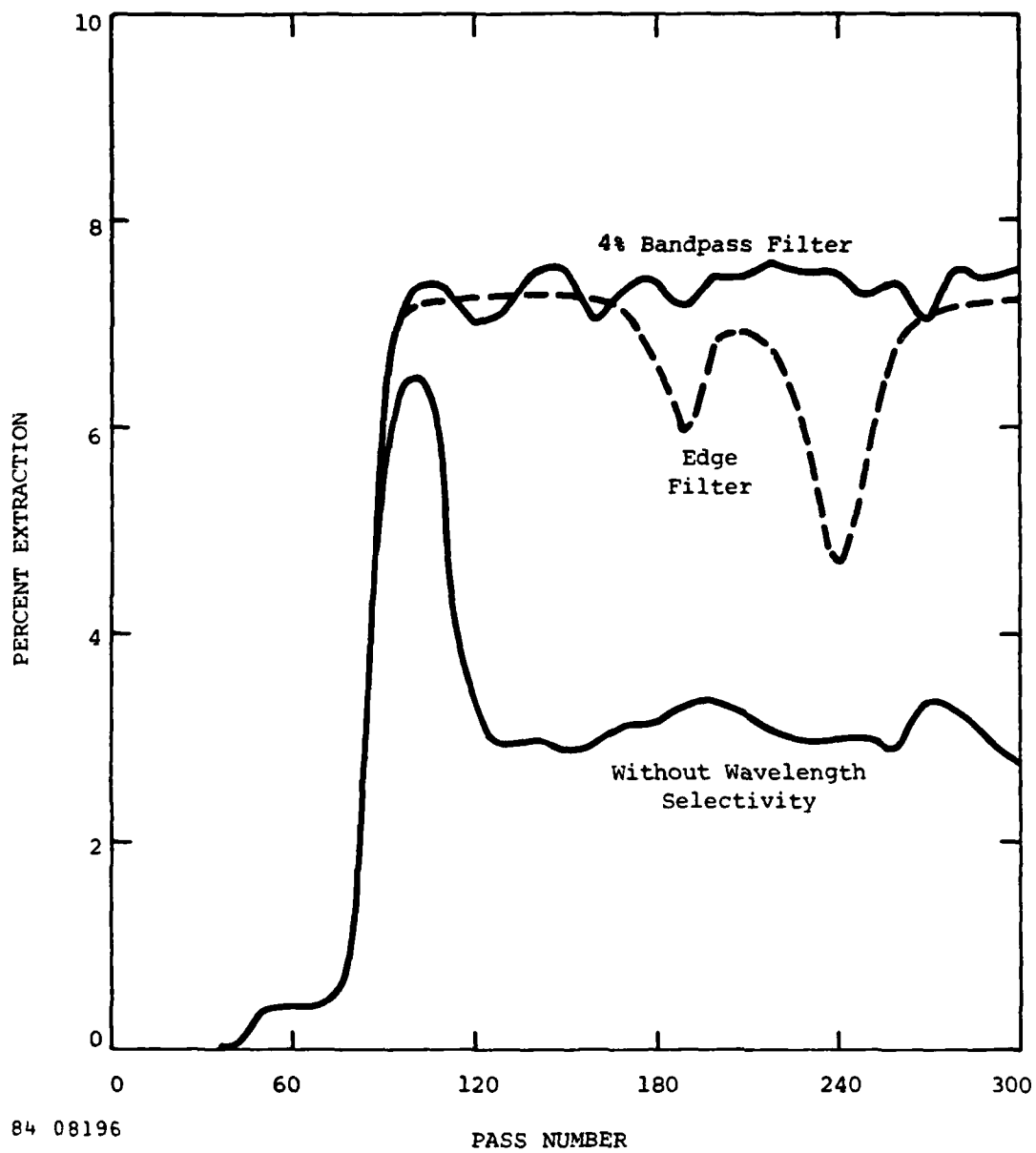


Figure 2-9. Introduction of Wavelength Selectivity Eliminates Loss of Extraction Efficiency Due to Sidebands.

to allow for the chirp. The wiggler taper used in this example is especially designed to minimize chirp requirements; it will start up without chirp at an output coupling of 10 percent, although a small amount of chirp to longer wavelengths is required for startup with larger outcoupling. Another consideration is loss induced by the chirp. In the edge filter example shown in Figure 2-8, the laser has considerably higher loss after the chirp. This is desirable only if the additional losses are recoverable as outcoupled power.

REFERENCES

- 2-1. N.M. Kroll and M.N. Rosenbluth, "Sideband Instabilities in Trapped Particle Free-Electron Lasers," in Free-Electron Generators of Coherent Radiation, Physics of Quantum Electronics, Vol. 7, S.F. Jacobs, H.S. Pilloff, M. Sargent, M.O. Scully, and R. Spitzer, eds. (Addison-Wesley, 1980), p. 147. See also, N.M. Kroll, P.L. Morton, and M.N. Rosenbluth, "Free-Electron Lasers with Variable Parameter Wigglers," IEEE J. Quantum Electron., QE-17, 1436 (1981).
- 2-2. J.C. Goldstein and W.B. Colson, "Control of Optical Pulse Modulation Due to the Sideband Instability in Free-Electron Lasers," in the Proceedings of the International Conference on Lasers 1982, New Orleans, LA, December 15-17, 1982.
- 2-3. W.B. Colson and R.A. Freedman, "Synchrotron Instability for Long Pulses in Free-Electron Laser Oscillators," Optics Comm. 46, 37 (1983).
- 2-4. See, for example, the review by W.B. Colson and A. Renieri, "Pulse Propagation in Free-Electron Lasers," in the Proceedings of the Bendor Free Electron Laser Conference, J. de Physique, 44, p. C1-11 (1983).
- 2-5. C.C. Shih and M.Z. Caponi, "Theory of Multicomponent Wiggler Free-Electron Lasers in the Small-Signal Regime," Phys. Rev. A, 26, 438 (1982).
- 2-6. W.B. Colson and R.A. Freedman, "Oscillator Evolution in Free-Electron Lasers," Phys. Rev. A, 27, 1399 (1983).

- 2-7. J.C. Goldstein, "Evolution of Long Pulses in a Tapered Wiggler Free-Electron Laser," in Free-Electron Generators of Coherent Radiation, C.A. Brau, S.F. Jacobs, and M.O. Scully, eds., Proc. Soc. Photo-Optical Instrum. Engrs., 453, p. 2 (1984).
- 2-8. W.B. Colson, "Chaotic Optical Modes in Free-Electron Lasers," in Free-Electron Generators of Coherent Radiation, C.A. Brau, S.F. Jacobs, and M.O. Scully, eds., Proc. Soc. Photo-Optical Instrum. Engrs., 453, p. 290 (1984).
- 2-9. C.A. Brau and R.K. Cooper, "Variable Wiggler Optimization," in Free-Electron Generators of Coherent Radiation, Physics of Quantum Electronics, Vol. 7, S.F. Jacobs, H.S. Pilloff, M. Sargent, M.O. Scully, and R. Spitzer, eds., (Addison-Wesley, 1980) p. 647.
- 2-10. M.N. Rosenbluth, H.V. Wong, and B.N. Moore, "Free Electron Laser (Oscillator) - Linear Gain and Stable Pulse Propagation," in Free-Electron Generators of Coherent Radiation, C.A. Brau, S.F. Jacobs, and M.O. Scully, eds., Proc. Soc. Photo-Optical Instrum. Engrs., 453, p. 25 (1984).
- 2-11. A.E. Siegman, An Introduction to Lasers and Masers, McGraw Hill, New York, 1971.
- 2-12. D. Quimby and J. Slater, "Emittance Acceptance in Tapered-Wiggler Free-Electron Lasers," in Free Electron Generators of Coherent Radiation, C.A. Brau, S.F. Jacobs, and M.O. Scully, eds., Proc. Soc. Photo-Optical Instrum. Engrs., 453, p. 92 (1984).
- 2-13. W.B. Colson and S.K. Ride, "The Free Electron Laser: Maxwell's Equations Driven by Single-Particle Currents," in Free-Electron Generators of Coherent Radiation, Physics of Quantum Electronics, Vol. 7, S.F. Jacobs, H.S. Pilloff, M. Sargent, M.O. Scully, and R. Spitzer, eds., (Addison-Wesley, 1980) p. 377.

Section 3

WAVELENGTH-SELECTIVITY OPTIONS

Wavelength-dispersive optical elements may be required in the laser cavity for suppression of the sideband instability. This section discusses several schemes which provide adjustable selectivity in the desired wavelength range of about ± 1 percent, i.e., in a range of around 5 to 10 nm. The wavelength-selective element must provide sufficient losses to suppress the sideband evolution without adding losses to the cavity which prevent startup at the design wavelength. The selective optics must add very little wave front distortion, around $\lambda/100$ per surface. This implies highly homogeneous materials, especially for transmissive elements, and very high quality optical surfaces.

The approaches considered include thin-film dielectric coatings on the end mirrors, birefringent filters, and gratings, as well as a novel approach based on optical mode size variation with wavelength using a dispersive lens in the cavity. We have considered designs which would be suitable for near-term visible-wavelength FEL oscillator experiments, but note that the most promising candidates for high-power systems, which preclude use of transmissive optics within the cavity due to cooling requirements, are dielectric mirror coatings and gratings. While not suitable for high-power designs, the birefringent filter has the property to also serve as the cavity outcoupler. Thus any additional cavity losses induced by the filter following frequency chirp of the FEL can be included in the outcoupled power, an important efficiency consideration.

3.1 THIN-FILM MIRROR COATINGS

Thin-film dielectric coatings are often used on cavity end mirrors to achieve high reflectivity at the design frequency. Such mirrors generally are highly reflective only within a fairly narrow band of wavelengths and can therefore be used for wavelength selectivity. The reflectivity

profiles of various realizable dielectric stack designs are calculated and evaluated for suitability as wavelength-selective elements in an FEL.

A computer algorithm was written to calculate the ideal reflectance properties of thin-film periodic multilayer stacks.⁽³⁻¹⁾ Each period of the stack consisted of either two or four materials with alternating high and low refractive indexes. The refractive index was assumed homogeneous and the coating thickness was assumed uniform across the aperture of the mirror.

It should be noted that the model does not account for the following real aspects of multilayer stacks.^(3-2 to 3-4) The polycrystalline structure of the high index material will lead to light scattering and absorption of light. This effect may be modeled by giving its refractive index an imaginary component corresponding to the absorption at a given wavelength. Due to the paucity of experimental data for the coatings of interest, this effect was ignored. For realistic cases, the shape of the functions used in the sideband calculations of Section 2.3 will not change significantly, and the conclusions of that Section will still hold. The coating designs considered were purposely limited to physical thicknesses of $\sim 5 \mu\text{m}$ or less since errors due to cumulative film nonuniformity across the effective mirror aperture degrade the Strehl ratio significantly in thick stacks. For example, a cumulative nonuniformity of only 2 percent in a $4 \mu\text{m}$ thick stack causes an effective figure error of $\lambda/8$.⁽³⁻⁵⁾ We note that assuming perfect substrates and a coating figure error of $\lambda/28$ causes the on-axis intensity of a mirror to decrease 20 percent. Such considerations dictate control of thickness uniformity to below the 0.5 percent level.

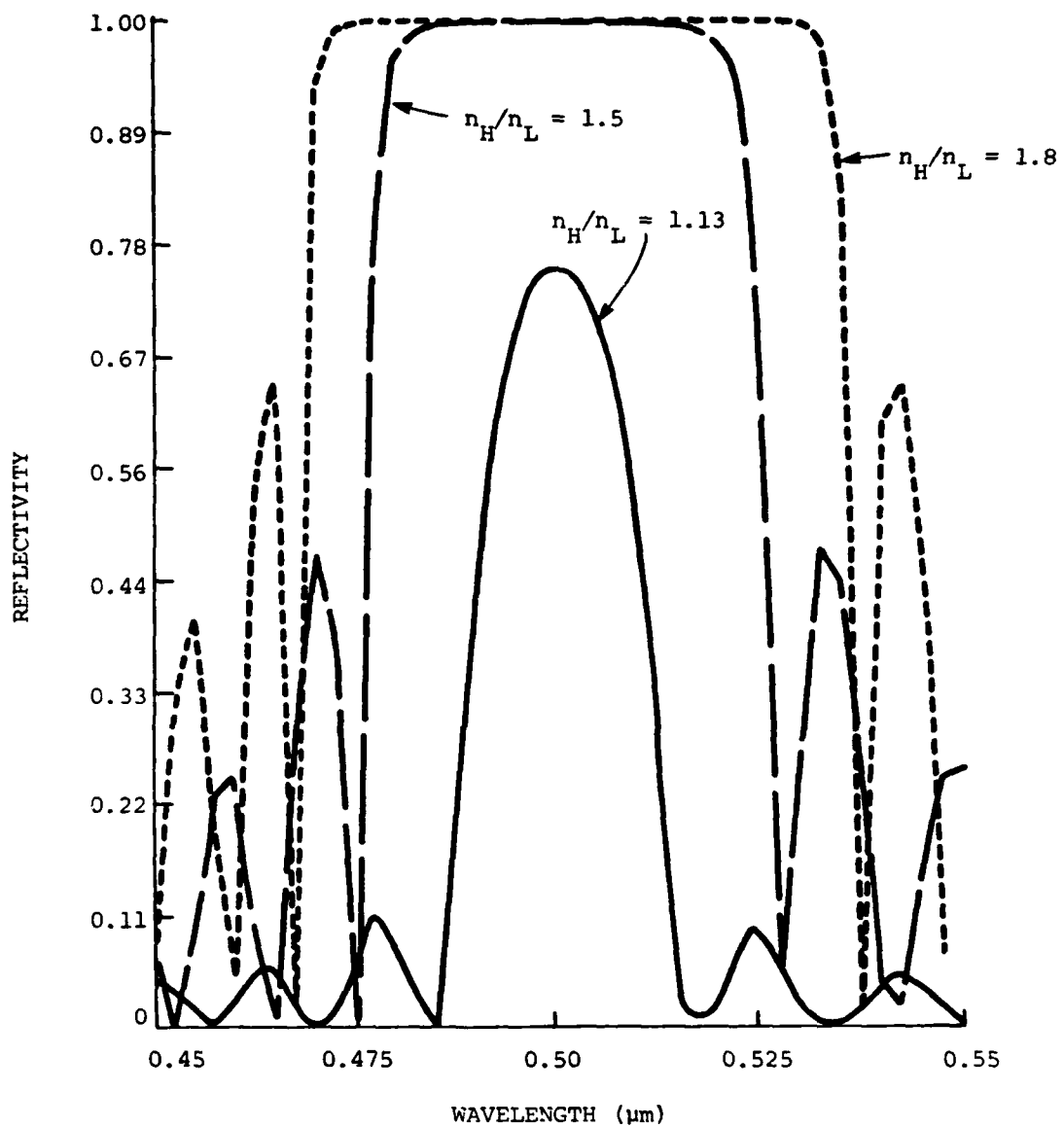
The purpose of the calculation was to determine which features of thin-film stacks were most significant for wavelength selectivity in the FEL. Various designs and combinations of materials were used in the calculations. The stack had either one or two high/low index of refraction combinations per period. The high/low combinations were either $\text{Al}_2\text{O}_3/\text{SiO}_2$,

$\text{ZrO}_2/\text{SiO}_2$, or $\text{TiO}_2/\text{SiO}_2$, with refractive index ratios of 1.126, 1.499, and 1.8, respectively. The bulk refractive indexes were used in all of the coating designs, due to lack of precise knowledge of the actual thin-film refractive index for all but one of the materials. The thin-film refractive index values will always be less than the bulk values, and thus the reflectivities of an actual coating may be expected to be slightly less than these theoretical curves.

Results of varying the refractive index ratio for three-quarter wave layers are presented in Figure 3-1. For a fixed number of periods, N , the maximum reflectivity R_{max} increases with the refractive index ratio, n_H/n_L , as does the wavelength range over which the reflectivity decreases by less than 1 percent (the high reflectivity bandwidth). The designs shown in the figure have R_{max} occurring at $0.5 \mu\text{m}$. It should be noted that for the physical thickness used, the Al_2O_3 design does not provide high reflectivity and may be useful only if it also serves as the outcoupler.

Figure 3-2 demonstrates that increasing N for quarter-wave designs increases both R_{max} and the bandwidth. It may be observed from the results of Section 2.3 that simple quarter-wave designs with a high reflectivity fail to provide narrow enough bandwidths for wavelength discrimination. The designs using $3\lambda/4$ thick layers in each period shown in Figure 3-1 are superior in this respect. Figure 3-3 illustrates this design feature for a fixed number of periods of the $\text{ZrO}_2/\text{SiO}_2$ combination, which is the most likely candidate for FEL applications (because of its damage resistance properties). Either of the $3\lambda/4$ or $5\lambda/4$ designs appear to provide the desired sideband suppression characteristics. Since both damage sensitivity and figure error increase with the physical thickness of the stack, the $3\lambda/4$ coating would probably be chosen.

Figure 3-4 demonstrates the kind of edge filter type coating designs that may be achieved by choosing more complicated structures for each coating period. In this case an alternating high/low/high/low combination was employed with the second high/low combination corresponding to a



84 08187

Figure 3-1. Dependence of Coating Reflectivity on Ratio of High Index to Low Index Ratio (n_H/n_L) for a Ten Period 3/4-Wave Stack.

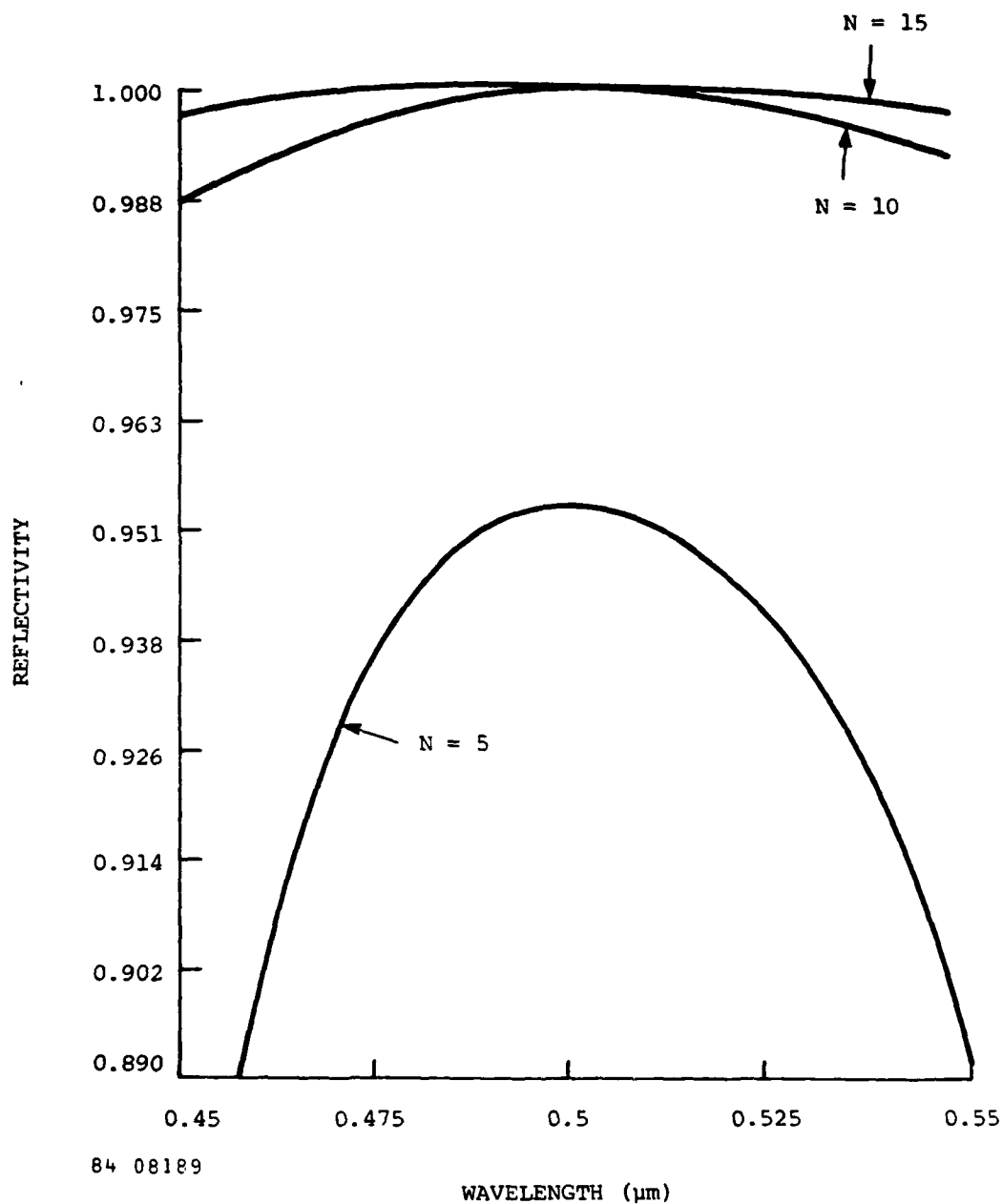


Figure 3-2. Dependence of Reflectivity and Bandwidth on Number of Periods N for $\text{ZrO}_2 + \text{SiO}_2$ Quarter-Wave Stack.

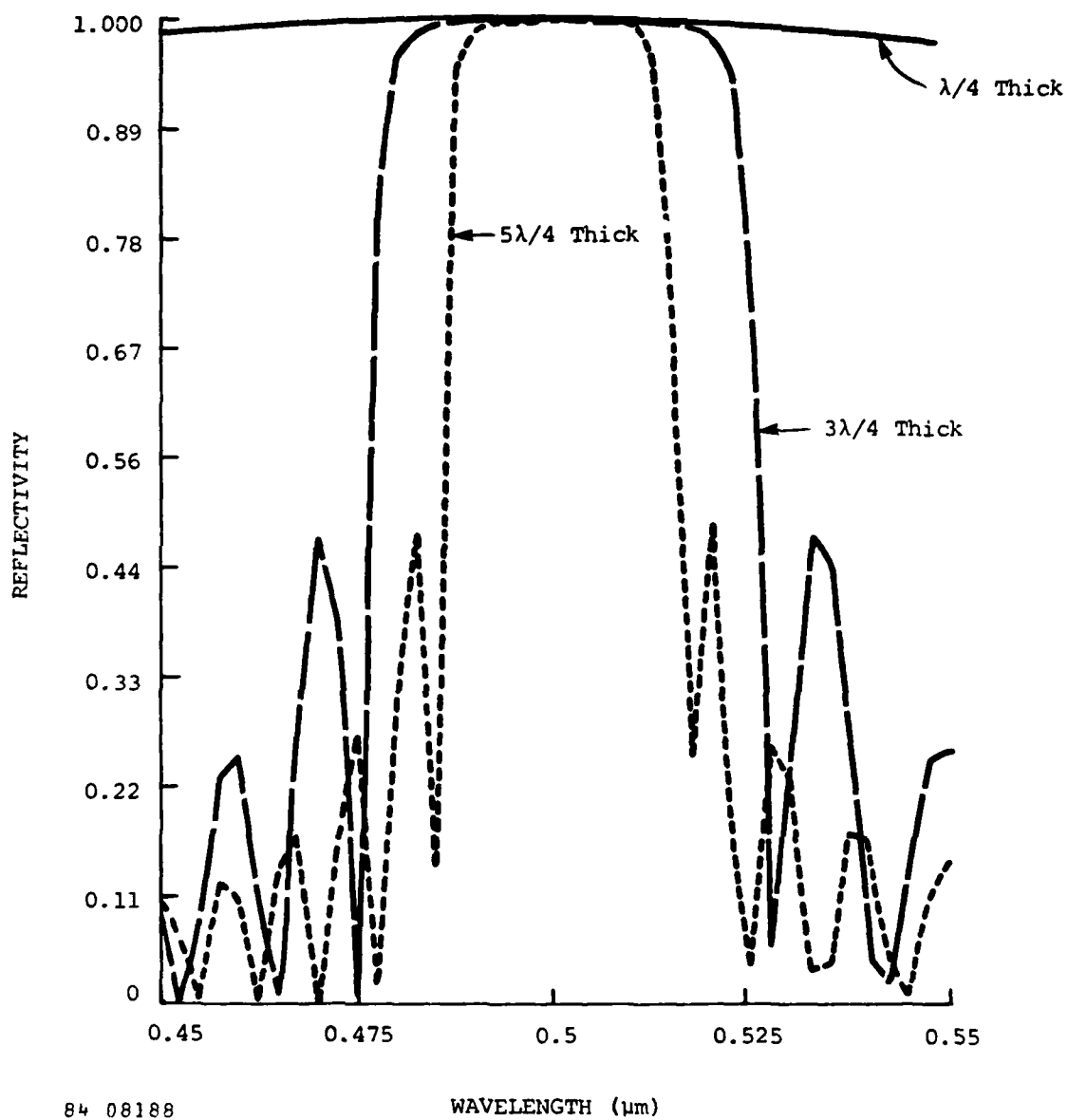


Figure 3-3. Dependence on Reflectivity on Film Thickness for $\text{ZrO}_2 + \text{SiO}_2$ Ten Period Stack.

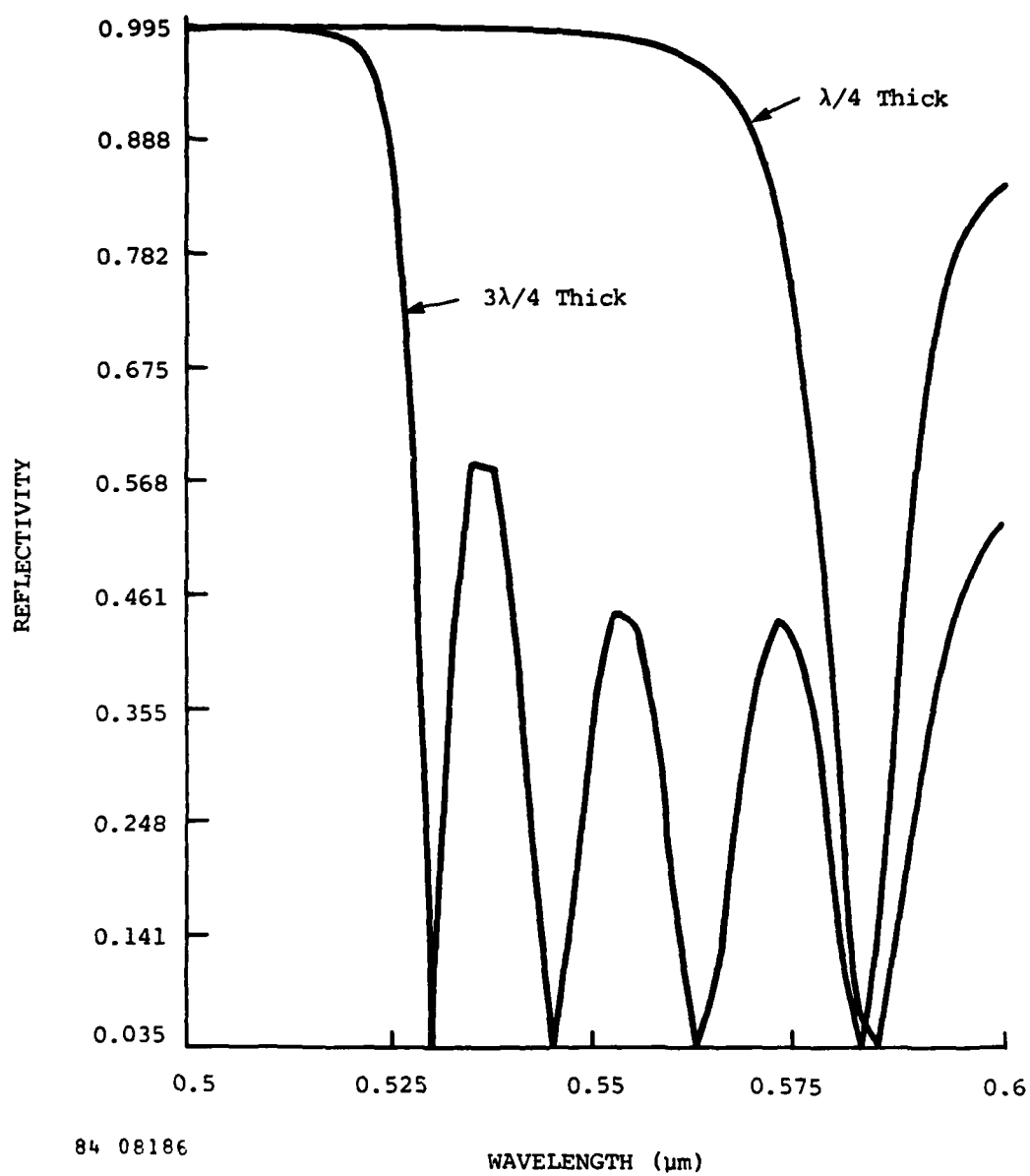


Figure 3-4. Five Period Edge Filter Design for Two Layer Thicknesses of $ZrO_2 + SiO_2$.

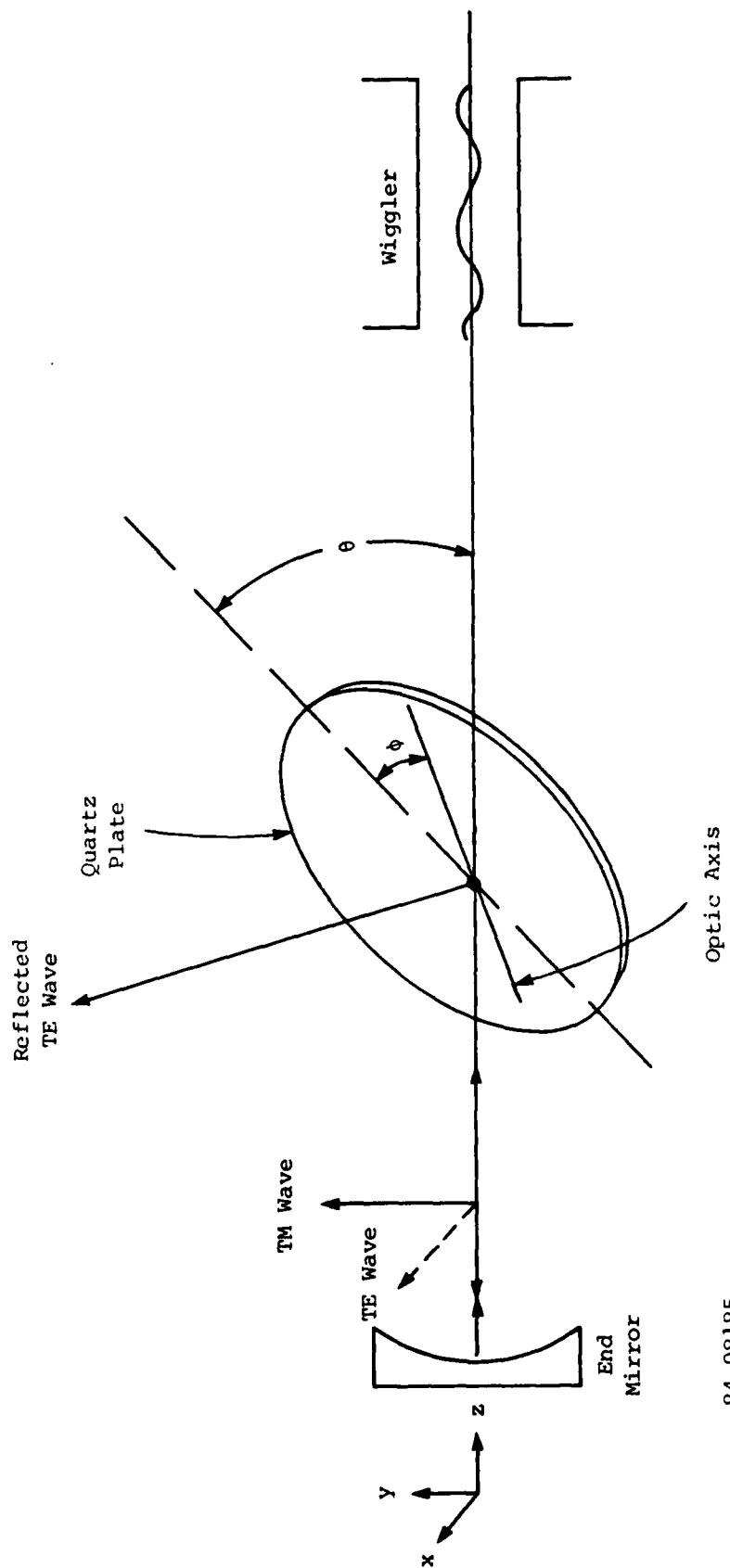
different wavelength of maximum reflectivity. As can be observed in the figure, the edge filter slopes can be made very sharp so such coating designs should completely suppress sideband development.

The damage threshold claims for edge filters are just as high as for the best "hard" mirror coatings (i.e., a claim⁽³⁻⁶⁾ of 5 MW/cm² CW at 1.06 μ m). Most coating designs include a $\lambda/2$ overcoat of SiO₂, since this has been shown experimentally⁽³⁻⁷⁾ to increase the damage threshold by at least a factor of 2. The effect of this additional coat on the maximum reflectivity, bandwidth and slope is insignificant as far as FEL performance and sideband suppression is concerned.

3.2 BIREFRINGENT FILTERS

Birefringent filters, also called Lyot filters, are based on the natural birefringence of certain materials such as crystalline quartz, which is the only material considered here. Frequency tuning is provided based upon the differing phase retardation of ordinary and extraordinary waves which pass through the crystal. A plane polarized input wave will become elliptically polarized in a manner dependent on the input wavelength, because of the dispersion of both ordinary and extraordinary refractive indexes. Filtering occurs because the FEL provides gain in only one plane (assuming a plane-polarized wiggler), and light which suffers a 90 degree rotation in a birefringent plate tilted at near Brewster's angle will undergo considerable loss by reflection (~17 percent per surface). Figure 3-5 defines the plate geometry relative to the FEL. Light which has a wavelength such that it is not rotated out of the wiggler plane (i.e., it remains a TM wave) suffers virtually no loss. Thus these devices are nearly ideal filters in that their transmission function has a theoretical maximum of unity. Their demonstrated high damage resistance is an additional advantage.⁽³⁻⁸⁾

The effective rotation of the plane of polarization as a function of λ is described in terms of a 2 x 2 Jones matrix which is a function of θ ,



84 08185

Figure 3-5. Orientation of Tilted Birefringent Plate in FEL Cavity.

the plate tilt angle with respect to the system optic axis, and ϕ , a rotation of the optic axis within this plane (see Figure 3-5). For low loss θ is chosen equal to Brewster's angle. The center wavelength is chosen by variation of ϕ . The general form of the transmission function for the TM component of the incident wave is⁽³⁻⁹⁾

$$T(\theta, \phi) = 1 - A(\theta, \phi) \sin^2 \left[\frac{\delta_e(\lambda) - \delta_o(\lambda)}{2} \right], \quad [3-1]$$

where A is the depth of modulation of the transmission function and δ_e and δ_o are the wavelength-dependent phase shifts inputted by the birefringent plate. When the argument of the sin function is a multiple of π , the transmission function is unity. The thickness of the birefringent plate and its angle ϕ determine the period of $T(\theta, \phi)$ and its wavelength of maximum transmission.

Figure 3-6 illustrates the tunability of three filters with thicknesses of 400, 800 and 1200 μm . These filters are inserted intracavity at Brewster's angle. With $\phi = 45$ degrees, the maximum in the transmission function occurs at 0.55 μm . Other wavelength values are easily obtained by simple rotation. The depth of modulation is seen to depend on this angle as well. Figure 3-6 demonstrates the increase in slope obtained by going to thicker plates.

High quality plates are readily available in crystalline quartz at all the design thicknesses considered here. Typical scattering losses below 0.1 percent per surface are desired and can be manufactured. A surface flatness approaching $\lambda/100$ can be achieved, so introduction of additional figure error is not a problem. Power levels exceeding 500 MW/cm^2 in a Q switched pulse train at a pulse repetition rate of 10 pps have been achieved in intracavity Nd:Glass laser systems and no spectral shift due to thermal effects was observed.⁽³⁻⁸⁾ It should be noted that the latter effect is second order for a birefringent filter as compared to a solid Fabry-Perot.

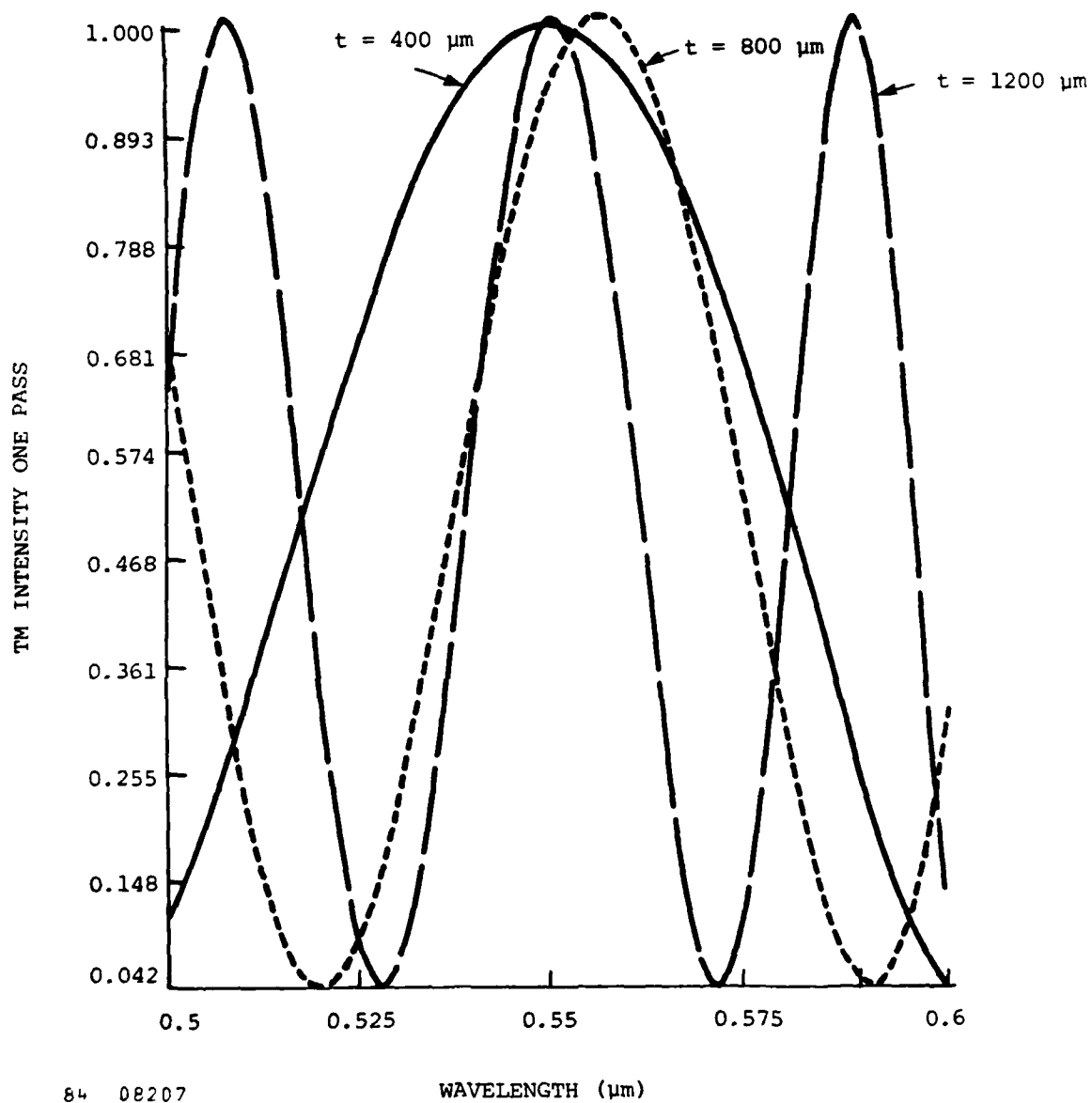


Figure 3-6. Birefringent Plate Transmission Functions for Various Plate Thicknesses, t . (Dotted curve is offset for Clarity.)

A feature of this filter is the possibility of providing wavelength-dependent outcoupling. If one side of the birefringent plate is antireflection coated and the FEL cavity is a ring, the filtered light is in a single reflected beam. Furthermore, if the plate is tilted slightly off Brewster's angle, it can provide the primary means of outcoupling for the cavity, with the outcoupled light directed in the same beam as that reflected by the filter. If the FEL chirps during the transition from the small-signal to saturated regimes, as is generally the case for tapered-wigglers, the saturated outcoupling could exceed the outcoupling during startup. This is useful for minimizing the startup time.

3.3 ANGULARLY-DISPERSIVE ELEMENTS

Angularly-dispersive elements include both gratings and prisms. Such elements can provide wavelength selectivity in an FEL cavity by dispersing optical sidebands so that they lose overlap with the gain medium and are not amplified. In the case of the prism, the wavelength discrimination is essentially fixed by the dispersion of the refractive index of the prism material and the beam size. Since a prism would be expected to handle rather high power levels in transmission, fused quartz would likely be required. Operation at a tilt angle near Brewster's angle would be necessary to minimize insertion losses. With these design constraints, a frequency resolution of $\Delta\lambda/\lambda \approx 0.05$ percent would be expected for conditions of a visible-wavelength FEL such as the design considered in Section 2.2. This may actually be too severe for FEL requirements. Diffraction gratings used in reflection offer more design freedom since the resolution is set by the grating period. For these reasons, the following design analysis focuses on gratings.

For a grating to operate as a sideband suppressor, the dispersion of the grating must be large enough to misalign the sideband component and small enough that all frequency components of the desired micropulses are still aligned in the cavity. This is possible, since the transform-limited spectral width of the micropulse is much less than the sideband shift.

Another requirement is efficiency. If the grating is not the output coupler, the grating efficiency should be 99 percent or greater. Another consideration which may limit the selectivity is potential cavity misalignment due to chirp during the startup phase.

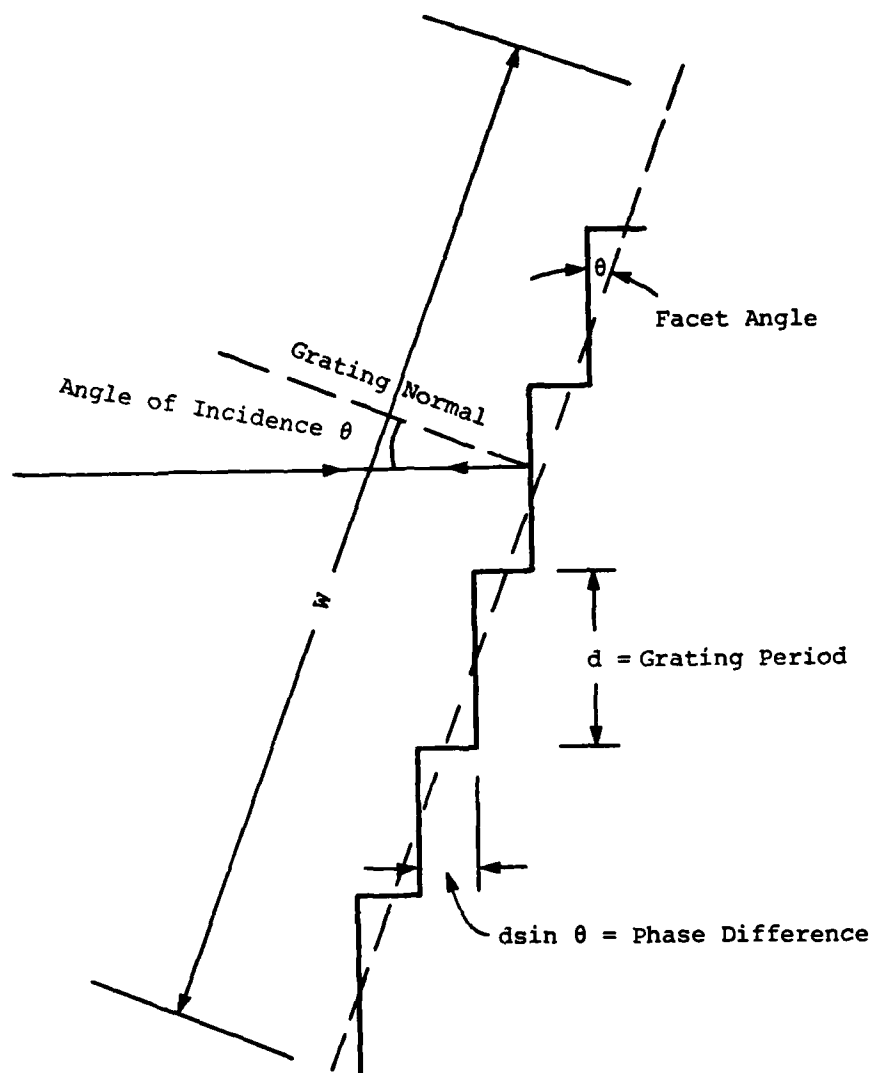
3.3.1 Grating Design for FEL Applications

The calculations of Section 2 indicate that about 1 percent wavelength discrimination eliminates sideband development. As a design example, consider a grating used in Littrow or "autocollimation" mounting as shown in Figure 3-7, which we will configure to suppress a sideband of wavelength offset $\Delta\lambda/\lambda$ of 1.5 percent. For this geometry the angle of incidence equals the blaze angle and the angle of diffraction. The Rayleigh criterion for resolution of the grating is determined by the optical path difference (in waves of light) between the extremities of the grating⁽³⁻¹⁰⁾

$$\frac{\Delta\lambda}{\lambda} = \frac{\lambda}{2W \sin\theta} , \quad [3-2]$$

where W is the grating width and θ is the angle of incidence. We assume that the beam size in the cavity requires a grating with a width of ~2 cm. The ideal blazed grating will have triangular grooves, and the angle that the primary facet makes with respect to the grating plane (the blaze angle) will be chosen to be the same as the angle of incidence (see Figure 3-7). Each groove is formed so that independently (by geometric optics) it acts like a small mirror tilted to redirect the light in the direction of a chosen diffracted order. For the FEL described in Section 2.2, the grating will have a blaze angle of ~0.05 degrees. The line spacing will be ~0.3 mm, an extremely modest requirement.

The groove profile determines the amount of energy diffracted into any individual order. We define the absolute efficiency to be the fraction of the incident power which is distributed in a single diffracted order. This is the efficiency quoted herein unless otherwise noted. The relative



84 08206

Figure 3-7. Illustration of Diffraction Grating Used in Littrow Mounting.

efficiency is defined as the fraction of the incident power which would be distributed in a single diffracted order if the grating surface had perfect reflectivity. Thus the relative efficiency is a measure of the groove efficiency. The periodicity and aperture function of the grating influence only the resolution of the grating, and because of the modest resolution requirements of the FEL, manufacturing imperfections in these characteristics are less important than control of the groove geometry. Since absolute efficiencies for intracavity application of gratings for the FEL should exceed 99 percent, we may immediately rule out symmetric groove profiles which can be at best only 50 percent efficient at near normal incidence angles.

3.3.2 Production of Concave Blazed Gratings

Figure error budget considerations for the FEL dictate a minimum number of intracavity optical elements. Although planar gratings would be of interest in ring cavity designs, concave gratings are useful in linear cavities since they combine both focusing and dispersion in a single element.⁽³⁻¹¹⁾ Thus the design and manufacture of concave gratings will be addressed.

Historically, most gratings were manufactured by diamond ruling of an aluminum or gold coated planar glass substrate. This technique will not yield gratings with the desired efficiencies for FEL applications, since it is very difficult to control groove profiles for blaze angles less than 0.5 degrees due to tool geometry and other factors.⁽³⁻¹⁰⁾ In addition, to achieve the required reflectivities at near normal incidence will require multilayer dielectric coated gratings, which are difficult to fabricate by ruling techniques. If gratings are ruled on a spherical substrate using the same engine as employed for planar gratings, the groove spacing and facet angle will not be uniform with respect to the spherical grating surface. If conventional ruling techniques must be employed, efficient, aberration-free gratings with a constant groove angle may be made by cylindrically bending a diffraction grating ruled on a plane

surface.⁽³⁻¹⁰⁾ However, due to the inconvenience of manufacture of ruled concave gratings and the lesser efficiency of such gratings, interference gratings can be an attractive alternative.

The simplest technique of creating interference gratings consists of coating a blank substrate with photoresist, exposing it to a fringe pattern and developing it. The intensity variation translates into a solubility variation across the photoresist. After development with a suitable solvent, the remaining photoresist has the proper spatial frequency variation. A reflective coating can then be applied. The control of the thickness and uniformity of the photoresist coating is of paramount importance for the overall quality of the resulting grating. Direct application of interference grating techniques at normal incidence produces gratings with symmetric groove profiles.

A blazed grating can be produced by a simple interference scheme which involves tilting the grating blank. A convex mirror is placed behind the grating blank and centered on the desired focal point of the grating. A standing wave pattern is formed at the tilted grating blank surface which produces fairly flat facets whose normals all point to the same focal point (the condition which provides uniform efficiency and constant blaze wavelength over the grating aperture). The wavelength of the laser used to set up the standing wave interference pattern will determine the blaze wavelength of the grating. This technique has yielded groove profiles of sufficient quality to produce 99 percent relative efficiency at a blaze angle of 10 degrees.⁽³⁻¹²⁾

For FEL applications, somewhat shallower blaze angles will likely be required. The blaze angle of an interference grating can be reduced by ion beam etching. This technique has produced high quality gratings with angles near 0.5 degrees and has demonstrated blaze angle reduction by factors of 3 to 10.⁽³⁻¹³⁾ Gratings blazed for wavelengths between 0.5 μm and 5 μm , with efficiencies of up to 90 percent, have been prepared with this technique.⁽³⁻¹⁴⁾

Another technique of interest for FEL applications uses the preferential chemical etching properties of crystalline silicon to produce a blazed grating following exposure of a photoresist surface layer to a symmetrical interference pattern. A suitable photoresist is deposited on a Si crystal oriented with its $\langle 110 \rangle$ plane at an appropriate angle to the surface. The $\langle 110 \rangle$ plane etches at a greater rate than the $\langle 111 \rangle$ plane resulting in a triangular groove profile. Thus the blaze angle is determined by the angle of the crystalline axis relative to the surface, rather than by the photoresist exposure process. The resulting surface may be coated with a dielectric stack for good efficiency. Features to 10^{-4} cm can be created in this manner. Typical rms surface roughness is 2 to 5 Angstroms. The smoothness of the surface provides low scattering loss and high damage resistance, two attributes required of FEL optics.

3.3.3 Practical Performance of Interference Gratings

The best interference and ruled gratings produce diffracted wave fronts of high optical quality, but interference gratings suffer less stray light and scattering problems. Scattering losses for interference gratings are predicted to be less than 0.2 percent.

The theoretical efficiency of a grating with two dielectric overcoats is ~95 percent. An experimental grating with 0.015 μm groove depth (approximately the value required for the FEL) has been made with 87 percent efficiency; the loss in efficiency was believed to be due to the inability to control the blaze angle over the entire grating aperture.⁽³⁻¹⁵⁾ More recently, a grating with nearly 99 percent relative efficiency was fabricated using preferential etching in Si and ion etching.⁽³⁻¹²⁾ Presumably, with suitable dielectric coatings this type of grating would be suitable for FEL application. Since most of the interference gratings with low blaze angles are first generation prototypes, one may expect improved efficiencies as experience in their manufacture is gained.

Highly damage resistant gratings⁽³⁻¹⁶⁾ are usually ruled in substrates of pyrex or copper (for infrared applications). Typical CW damage levels at $1.06 \mu\text{m}$ wavelength are 10 KW/cm^2 for 10 sec (glass substrate), while pulsed levels are 140 MW/cm^2 at 25 nsec, 70 MW/cm^2 at 100 nsec, and 7 Joules/cm^2 at 100 nsec (on an electroless nickel copper substrate). Thus circulating powers could be as high as 35 MW for 100 nsec pulses at low repetition rates. Thus CW damage would limit the design of Section 2.2 (but at $1 \mu\text{m}$) to several kW average circulating power. The coating material for the above figures is aluminum. Overcoating with gold or silver improves the reflectivity but lowers the damage threshold by 2. Damage measurements of dielectric coated gratings are not available, but would be expected to be higher, as is the case for mirrors.

3.4 FREQUENCY SELECTIVITY THROUGH A DISPERSIVE OPTICAL MODE SIZE

The FEL optical gain is sensitive to spatial characteristics of the optical mode due to variation of the electron-photon overlap with mode size. This property can be exploited to provide a frequency-dependent round trip loss for the purpose of suppressing the sideband instability. The basic concept is to use a dispersive lens in the cavity to provide a wavelength-dependent mode size, and to configure the cavity so that the available dispersion provides the degree of selectivity desired.

A convenient property of the FEL so far as this goal is concerned is the need for near-concentric cavities. This geometry provides the small spot size at the wiggler and the large spots at the end mirrors necessary to avoid mirror damage. The mode size of the near-concentric cavity is extremely dependent on the mirror focal length (assuming fixed cavity length), so that only small focal length changes are needed from the dispersive element. The Rayleigh range, Z_R , for the focal region near the center of a symmetric near-concentric cavity is a simple function of the distance between the centers of curvature of the end mirrors, d , and is given by

$$Z_R = \frac{1}{2} (d L)^{1/2}, \quad [3-3]$$

where L is the total cavity length. The Rayleigh range determines the mode size, and the mode size determines the electron photon overlap and, hence, the FEL gain. An example calculation of gain as a function of distance between the centers of curvature of the end mirrors is given in Figure 3-8. Key parameters of this calculation are listed in Table 3-1. It is worth noting that the overall shape of this curve is dependent primarily on the emittance value chosen. Aperturing of the beam by the wiggler magnets is unimportant over the range shown.

The geometry, which can provide variable selectivity at the 1 percent wavelength resolution of interest, is shown in Figure 3-9. The combined focal length of the lens and mirror M_2 becomes more dispersive as their focal lengths decrease, while the power of the combination can remain fixed if the spacing between them is adjusted properly. The mirror-lens combination was analyzed with standard ABCD matrix ray-trace formalism to determine the sensitivity of the combination to dispersion. As an example, consider a combination which has a positive fused silica lens with a 1 m focal length separated from mirror M_2 by 10 cm. The corresponding convex mirror to produce an effective focal length of 15 m has a focal length of -0.467 m. The sensitivity of this example to wavelength is illustrated by a 28 cm change in focal length for a 5 nm wavelength change. The focal length variation can be combined with Figure 3-8 for a rough estimate of the net gain as a function of wavelength, and is given in Figure 3-10. The changes in effective focal length for 5 nm excursions of the laser wavelength are the correct size to suppress the sideband instability, and still provide acceptable gain over the range of wavelengths desired for FEL startup. The selectivity of the lens mirror combination can be adjusted by choosing different combinations of strengths of the elements.

The main detriment to the use of the lens-mirror combination in the FEL cavity is the effect on the figure error budget. The introduction of the lens into the cavity adds a figure error which is sensed twice each

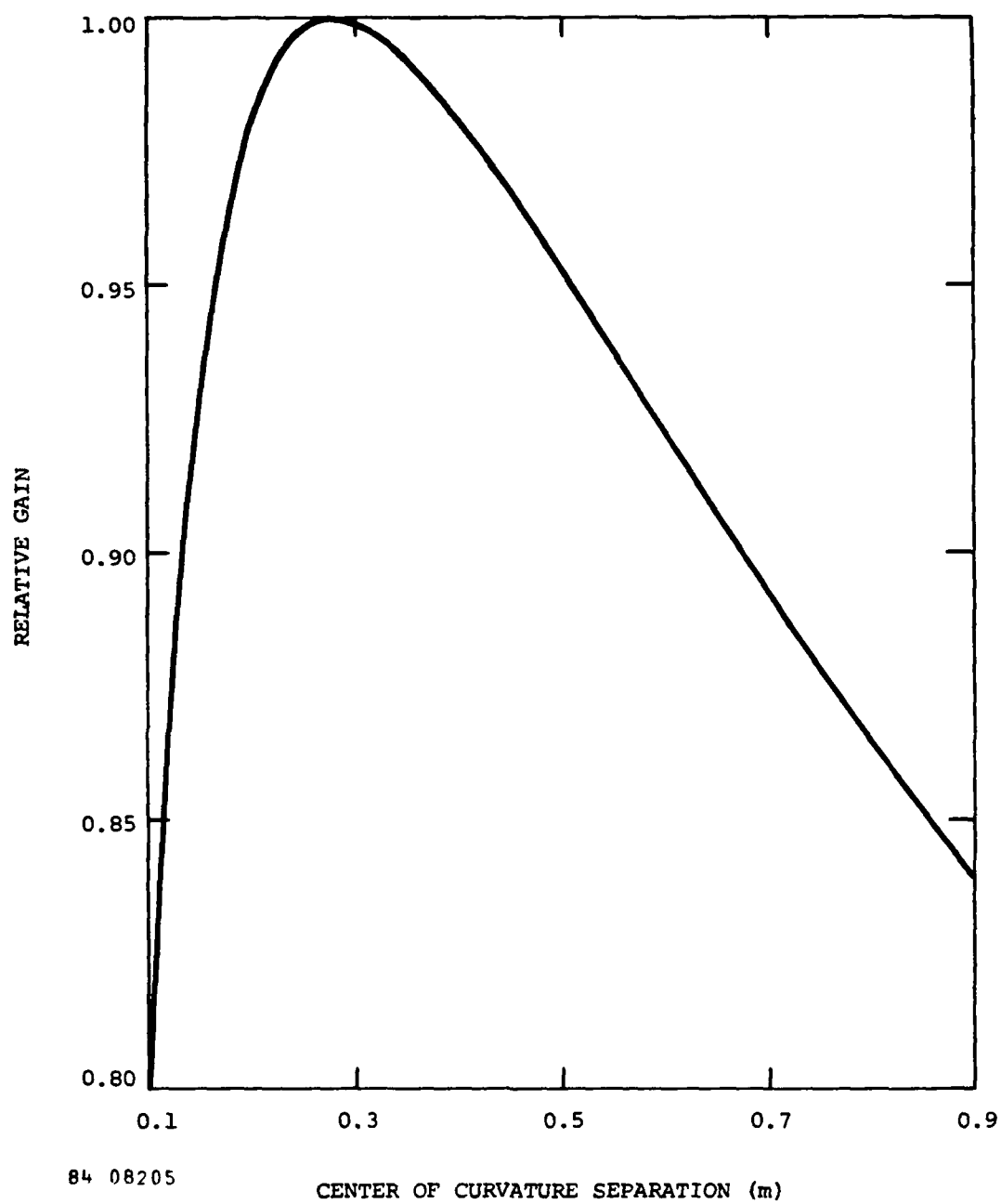
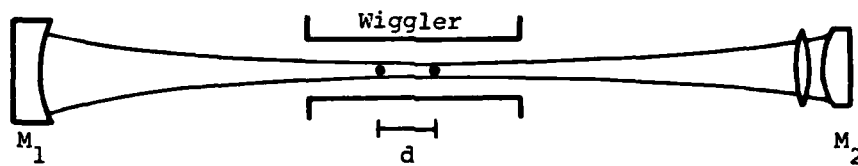


Figure 3-8. Calculation of FEL Gain in a Near-Concentric Cavity with Variable Mode Size. Key Parameters Assumed are Given in Table 3-1.

Table 3-1

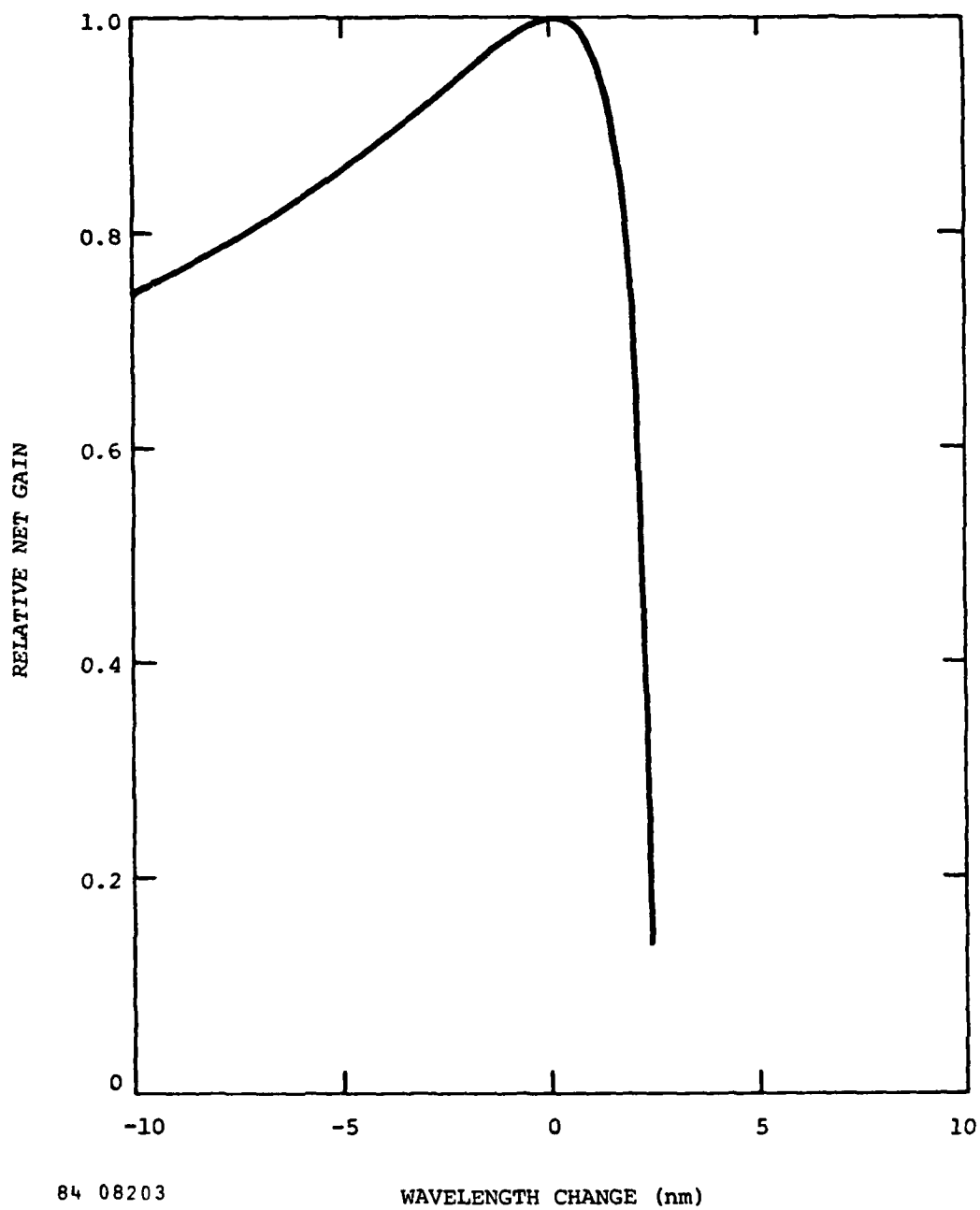
PARAMETERS OF GAIN CALCULATION WITH VARIABLE MODE SIZE

Normalized Emittance	0.01 cm rad
Wiggler Full Gap	0.45 cm
Wiggler Length	5 m
Wiggler Wavelength	2.02 cm
Optical Wavelength	0.5 μ m
Beam Energy	120 MeV
$a_w = \frac{e B_{\max} \lambda_w}{2^{2/3} \pi m c^2}$	1.33
Cavity Length	60 meters



84 08204

Figure 3-9. Near-Concentric Cavity Geometry for Use of Dispersive Lens for Mode Size Variation.



84 08203

Figure 3-10. Calculation of Net FEL Gain Variation Due to Change in Mode Size.

round trip. The lens figure error introduced by the two passes each round trip is correlated since a ray passes through the same spot on the lens on each pass. For example, a lens made to a figure error of $\lambda/50$ introduces an effective round trip figure error of $\lambda/25$, which in some cases may be an unacceptable addition to the figure error budget.

REFERENCES

- 3-1. M. Born and E. Wolf, Principles of Optics, 4th ed., Oxford, England: Pergamon, 1970.
- 3-2. E.N. Farabaugh, D.M. Sanders, M.E. Wilke, S.A. Hurwitz, and W.K. Haller, "Preparation of Thin Amorphous Films by E-beam Evaporation from Multiple Sources," in the Proceedings of NBS Conference on Laser Induced Damage in Optical Materials (1981).
- 3-3. P.J. Martin, H.A. Macleod, R.P. Netterfield, C.G. Pacey and W.G. Sainty, "Ion Beam Assisted Deposition of Thin Films," Applied Optics, 22, 178 (1983).
- 3-4. D.R. Gibson and P.H. Lissberger, "Optical Properties of Narrowband Spectral Filter Coatings Related to Layer Structure and Preparation," Applied Optics, 22, 269 (1983).
- 3-5. H.E. Bennett and D.K. Burge, "Sensitive Technique for Measuring Apparent Optical Figure Error Caused by Coating Nonuniformity," in NBS Special Publication 638, Proceedings of the Conference on Laser Induced Damage in Optical Materials, p. 421-426.
- 3-6. CVI Laser Optics Catalog.
- 3-7. T.T. Hart, T.L. Lichtenstein, C.K. Carniglia and F. Rainer, "Effects of Undercoats and Overcoats on Damage Thresholds of 248 nm Coatings," in NBS Special Publication 638, Proceedings of the Conference on Laser Induced Damage in Optical Materials, p. 344-350.
- 3-8. Yung S. Liu, "Line Narrowing and Tuning of a High-Power Nd:Glass Laser Using an Intracavity Brewster-Angle Birefringent Filter," J. of Applied Physics, 48, 647 (1977).

- 3-9. D.R. Preuss and J.L. Gole, "Three-Stage Birefringent Filter Tuning Smoothly Over the Visible Region: Theoretical Treatment and Experimental Design," *Applied Optics*, 19, 702 (1980).
- 3-10. M.C. Hutley, Diffraction Gratings, Academic Press, London (1982).
- 3-11. Y. Fujii and J. Minowa, "Optical Demultiplexer Using a Silicon Concave Diffraction Grating," *Applied Optics*, 22, 974 (1983).
- 3-12. R. Petit, Electromagnetic Theory of Gratings, Springer-Verlag, (1980).
- 3-13. P.R. Stuart, M.C. Hutley and M. Stedman, "Photofabricated Blazed X-ray Diffraction Gratings," *Applied Optics*, 15, 2618 (1976).
- 3-14. J. Muller, R. Nietz and U. Unrau, "Blazed Holographic Gratings by Selective Etching in Silicon," *Proc. Soc. Photo-Opt. Instrum. Eng.*, 192, 244 (1979).
- 3-15. D. Maystre, *Opt. Commun.*, 26, 127 (1978).
- 3-16. PTR Optics Grating Catalog. Grating specifications.

APPENDIX A

Demonstration of large electron-beam energy extraction by a tapered-wiggler free-electron laser

W.M. Grossman, T.L. Churchill, D.C. Quimby and J.M. Slater

Mathematical Sciences Northwest, Inc.
2755 Northup Way, Bellevue, Washington 98004

and

J. Adamski, R.C. Kennedy and D.R. Shoffstall

Boeing Aerospace Company
P.O. Box 3999, Seattle, Washington 98124

Abstract

Electron-beam energy spectral measurements were made on a tapered-wiggler free-electron laser amplifier. A 10 MeV electron beam from a traveling-wave linear accelerator interacted in a tapered-wiggler with an intense 10.6 μm CO₂ laser beam. The electron spectra show a 4 percent net energy loss and a 9 percent peak loss. Measurements of electron energy spectra, extraction efficiency as a function of electron-beam energy, and extraction efficiency as a function of optical power are presented and are consistent with theoretically predicted performance.

Introduction

The experimental results reported here help validate the concept of the taper-wiggler free-electron laser (FEL). The device is a candidate for a high-efficiency tunable source of coherent radiation. The first FEL, demonstrated at Stanford,¹ had an untapered wiggler. The tapered wiggler² differs from the Stanford wiggler in that the resonant electron energy of the wiggler magnet varies along its length to maintain a resonant electron-photon interaction as the electrons decelerate. The resonant energy of the wiggler can be tapered by varying the wavelength or amplitude of the periodic magnetic field as a function of axial position. Electrons trapped in the ponderomotive potential well formed by the electric field of the light and the magnetic field of the wiggler decelerate in accord with the resonant energy change, or taper, of the wiggler. Adding taper to the FEL wiggler can provide increased electron-beam energy extraction and increased overall efficiency at the expense of reduced gain.

Not all of the electrons entering the wiggler are trapped in the ponderomotive potential and the nominal trapping fraction for this experiment is about 50 percent. Under these conditions the net deceleration is about half the peak deceleration. The corresponding energy spectrum has two peaks of roughly equal current, one near the entrance energy and the other at the energy resonant with the wiggler exit. The wiggler used in this experiment has a 9 percent energy taper and a nominal net electron energy extraction of about 4 percent.

The highest net energy extraction previously reported by our group is about 2.5 percent indicating strong interaction, but less than optimal trapping over the length of the 9 percent taper wiggler in our experiment.³ This result is limited by a combination of non-optimum overlap of the electron and laser beams, the electron beam emittance, and the laser power. Detrapping of electrons along the wiggler length is evident in the energy spectra. Here we report results of electron-beam extraction measurements in which the electron beam emittance is reduced from our previous experiments. We again use the 9 percent tapered wiggler. The electron beam size is not limiting, and 4 percent net extraction is observed. The results are consistent with theoretical predictions and give added verification to the tapered wiggler concept. They are also consistent with the results of the Los Alamos tapered wiggler experiment in which an energy taper of 7 percent led to about 4 percent net extraction.⁴

Experiment

Electron beam energy extraction is measured in the FEL amplifier using the configuration shown in Figure 1. The wiggler is 2.3m long, has 97 periods, and is constructed of SmCo₅ permanent magnets. It has 9 percent resonant energy taper at constant synchronous phase, achieved by decreasing the period 13 percent and the peak field strength 8 percent along the length of the wiggler with fixed gap. In the experiments reported here, the CO₂ laser generates a 40 ns optical pulse, and the linear accelerator typically generates a 0.5 μsec

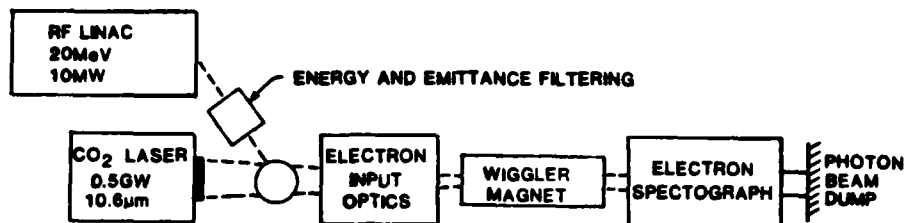


Figure 1. Block diagram of amplifier experiment.

electron beam macropulse consisting of 20 psec micropulses generated at 2.8 GHz. The two beams are timed so that the shorter optical pulse falls upon the longer electron-beam pulse in the wiggler. During the period of overlap, all of the electron micropulses are subject to the FEL interaction. The spectrograph can follow the envelope of the temporal evolution of the electron-beam energy spectra on a nanosecond timescale, but cannot resolve individual micropulses. Most of the optical beam cannot interact with the electrons because the linac duty cycle is 0.05; therefore, the average gain is low and is not measured. The RF linac, electron-beam spectrograph, wiggler magnet, and CO₂ laser used in the extraction experiments have previously been reported upon in detail.³

The Boeing linac is a traveling-wave radio-frequency linear accelerator capable of acceleration to 30 MeV. The primary power is supplied by a single 20 MW peak, 2 kW average, S-band klystron. A gridded electron gun provides macropulse widths over the range of 0.005 to 10 μ sec. Since our last reported results,³ the gun was modified by the addition of a cowling intended to intercept electrons from the perimeter of the cathode and reduce the linac's emittance. Two stages of bunching at the fundamental frequency compress the charge into 15 to 20 degrees of phase of the accelerating wave to achieve an energy spread of less than 2 percent. The output pulse train consists of pulses which are approximately 20 psec long and are separated by the 350 psec RF cycle time. Peak micropulse currents are from 2 to 5 amps leaving the accelerator structure, and as described later, are lower at the wiggler due to losses in filtering and other losses in transport. The full width energy spread is 2 percent, and the normalized emittance for 100 percent of the charge at the wiggler, defined at $\gamma\alpha x'$, is about 0.01 cm-rad in each plane. The beam is spatially filtered to achieve this emittance and energy spread, and the peak micropulse currents are typically 50 to 200 mA at the wiggler.

The electron-beam transport and optics system is shown in Figure 2. The system provides achromatic transport to the FEL with adjustable energy and emittance filtering. The beam

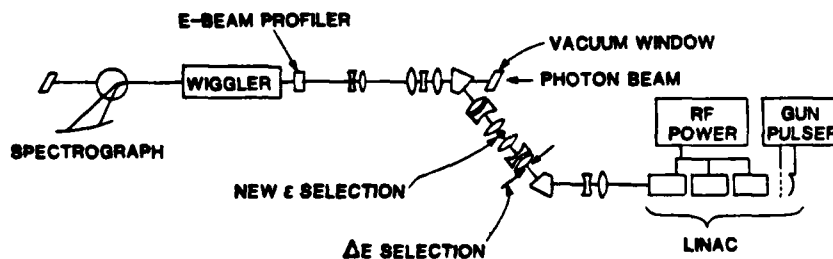


Figure 2. Electron beam transport system.

is switched into the FEL experiment line by a dog-leg translation system similar to a design suggested by Swenson.³ Mechanical slits in the dog-leg provide energy and emittance selection. Five quadrupole magnets just upstream of the wiggler are used to adjust the focal position and convergence angle in two planes of the input beam. Five fluorescent screens are deployed within the wiggler and six screens are deployed in the transport legs to assist in pointing and focusing the electron-beam.

Two beamline modifications have been made since earlier experiments. They are the upgrade of the emittance slits in the dog-leg and the addition of an emittance-measuring wire-scanner just upstream of the wiggler. The new emittance filter consists of four independently movable jaws and replaced a fixed aperture filter. The new jaws are typically

used with gaps 3 times smaller than previously available. The emittance filter also has been moved about 20 cm down the beamline, placing it exactly at the predicted symmetry point of the dog-leg where no encoding of energy on position should exist. In order to move the emittance filter, the quadrupole magnet previously located at the symmetry point has been replaced by a pair of quadrupoles placed symmetrically about the emittance filter.

A new emittance-measuring wire-scanning profilometer is located directly upstream of the wiggler and consists of a wire-shadow scanner, a turnout magnet, and a stopping block. Transport from the scanner to the stopping block is nearly 100 percent, and transport from the scanner location to the spectrograph via the wiggler, when the turnout magnet is off, also is near 100 percent. This insures that the emittance and spectrograph measurements both include the entire beam. Emittance is deduced by measuring beam size as a function of the strength of an upstream quadrupole magnet.^{6,7} These measurements give the minimum spot size and divergence angle of the beam, allowing the emittance to be computed.

The electron spectrograph is a 12-inch round pole Browne-Beuchner⁸ design. The focal plane of the spectrograph has segmented stopping blocks cabled to oscilloscope channels. These allow temporal bandwidth of approximately 200 MHz and, as used, have a minimum of 1 percent energy spread per oscilloscope channel. The use of discrete stopping blocks limits the spectrograph in energy resolution, but has the advantage of allowing temporal resolution and relatively simple calibration.

The CO₂ laser consists of an oscillator-preamplifier-amplifier chain. A low pressure gain cell forces the oscillator to operate on a single longitudinal mode. An electro-optical switch is used to slice out a fast rising 40 ns pulse from the 150 ns oscillator output, as shown in Figure 3. The peak optical power delivered into the wiggler was typically about 0.5 GW based on independent measurements of the pulse shape and the integrated energy.

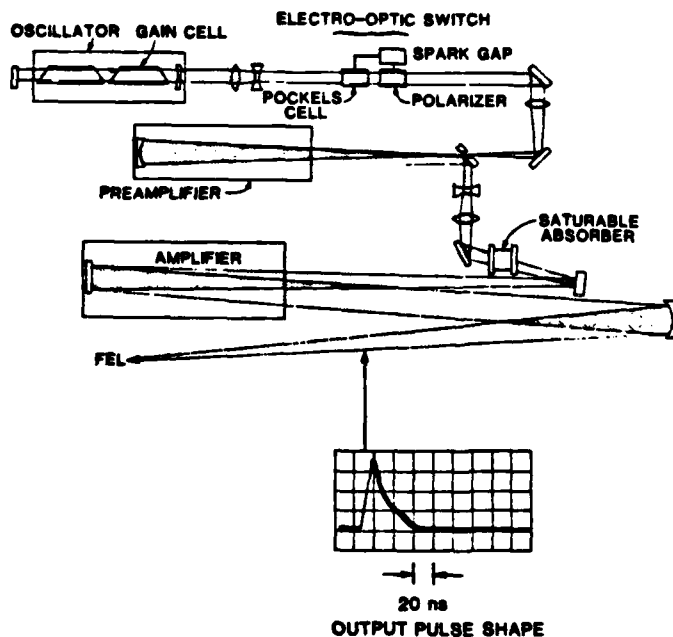


Figure 3. CO₂ laser chain and output pulseform.

Electron energy spectrum measurements and modeling

Electron energy gain or loss resulting from the FEL interaction is measured with the electron spectrograph. In these experiments, the interaction is easily identified in the time-resolved spectra because the optical pulse has different temporal behavior than the electron macropulse. Representative histories of the current into the spectrograph channels during the CO₂ laser pulse are shown in Figure 4. Immediately prior to the time of laser overlap, most of the current was entering the spectrograph channel labeled -0.5 percent.

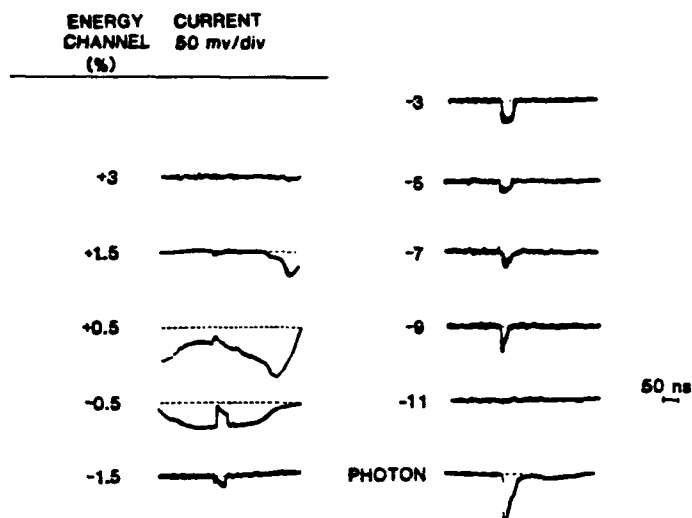


Figure 4. Spectrograph histories during FEL interaction.

It can be seen from the traces that the mean energy is varying on a timescale much longer than the laser pulse, and this variation can be ignored. During peak laser power, nearly 90 percent of the electrons in the nominal input channel are displaced to higher or lower energies. A small amount of current is accelerated to higher energy in the +1.5 percent channel, and the greater fraction is decelerated into the lower energy channels, down to -9 percent. The temporal histories of the channels differ greatly reflecting the nonlinear nature of the electron trapping as a function of optical power.

An electron beam spectrum measured at the time of peak CO₂ intensity is shown in Figure 5. There is a 4 percent shift in the average electron energy assuming the current is evenly distributed within each spectrograph channel. The maximum extraction for any electron is 9 percent. Superimposed upon that data is the electron beam spectrum prior to injection of the CO₂ beam. The curves can be considered as output and input spectrum, respectively, because the macropulse current and spectral content do not change significantly on several nanosecond timescales. The photon pulse, not shown, has a peak power of about 0.5 GW and the effective power could be less because imperfect optical beam quality (Strehl ratio <1) can only degrade the interaction.

The electron spectra are taken with the spectrograph channels connected in pairs with combined 1 percent energy acceptance over the range of 18.2 to 19.0 MeV, and 2 percent acceptance elsewhere. For any channel, the uncertainty in current at the time of maximum photon flux is less than 25 percent. An indication of the reliability of the measurements is that the sum of the measured channel currents, which should not vary, typically differ by less than 10 percent between interaction and non-interaction traces. For the data shown in Figure 5, the peak micropulse current at the time of the interaction is about 160 mA.

Using the input spectrum of Figure 5, an output electron energy spectrum, including the interaction, has been calculated by direct integration of the equations for electron energy loss and electron phase in the ponderomotive potential of the FEL interaction.² In the calculation, it is assumed that the electron-beam and 500 MW optical beams are optimally

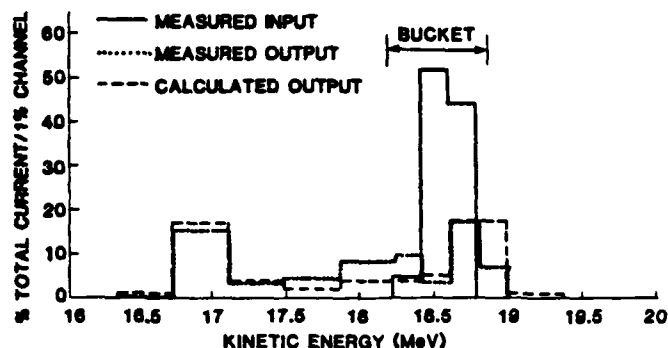


Figure 5. Measured input and output electron beam spectra for FEL interaction.

focused and coaligned, and the optical beam is diffraction-limited. A normalized emittance of 0.023 cm-rad at $\gamma = 37$ is assumed for both planes. The effect of emittance is included in the calculation in a two-step process. First the optical electric (E) fields and wiggler magnetic (B) fields experienced by each electron are computed as a function of axial position, including the off-axis motion but ignoring the small effect of the FEL on the trajectory. Then the energy loss is determined in a one-dimensional integration of the energy and phase equation for electrons in the ponderomotive potential well of the FEL. This is done using the previously computed E and B fields experienced by each electron. The resulting theoretical electron spectrum, shown as the dashed line in Figure 5, corresponds to a net extraction of 4.0 percent and is in excellent agreement with the data. A net extraction of 4.7 percent is predicted for the same parameters, except with zero emittance. This shows that for these parameters the extraction is only weakly dependent on the emittance. The emittance used to give a theoretical curve matching the data was about twice the measured value. This choice of emittance may roughly compensate for simplifying assumptions used in the theoretical model which would otherwise lead to an overestimate of net extraction. These assumptions are that the CO₂ laser is diffraction-limited and that the electron and optical beams are optimally pointed and focused.

Extraction as a function of input energy has been measured over a range of input energies from 18.0 to 19.2 MeV. This data is shown in Figure 6. The experimental data is

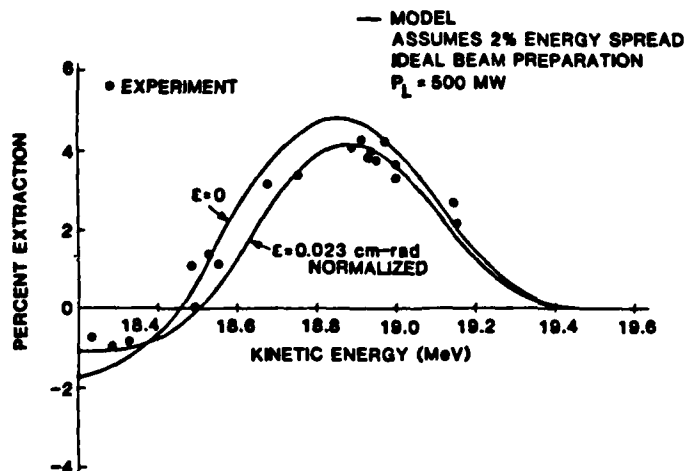


Figure 6. Extraction as a function of input energy.

upshifted 1.5 percent in energy to allow for a small uncertainty in spectrograph calibration. Peak extraction is observed near 19 MeV for our wiggler. When the electron energy is detuned below 18.4 MeV, net acceleration of the electrons is seen. Electron deceleration and energy extraction is observed over a range of 3 percent in energy. This implies that net gain is present over an optical bandwidth of twice the energy bandwidth or about 6 percent. The data is in agreement with the theoretically predicted curves generated assuming normalized emittances of 0 and 0.023 cm-rad, perfect focusing, perfect alignment, and a diffraction-limited optical beam. The points shown do not include all the data taken. With misalignment, poor focusing, or other problems, it is always possible to achieve results in which the magnitude of the extraction is too low, but it is not possible to achieve extraction results that are artificially high except by actual measurement errors.

Electron energy extraction has been measured as a function of laser power and is shown in Figure 7. Extraction is seen to increase with laser power. The data is taken from

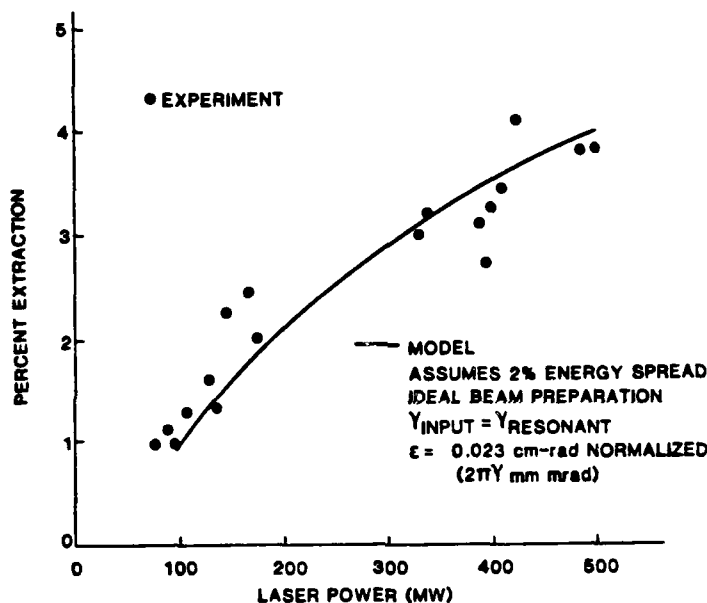


Figure 7. Extraction as a function of laser power in the wiggler.

three time-resolved electron spectral records. Extraction is found as a function of time and using laser pulse histories, the extraction as a function of laser power is deduced. The data is in general agreement with theoretical predictions. Again, perfect focusing and alignment are assumed for the theoretical prediction, and a finite 0.023 cm-rad normalized emittance is used as a rough estimate of all the effects of nonideal preparation of both beams. When the extraction is predicted as a function of laser power for zero emittance, the theoretical results parallel those shown in Figure 7, but the extraction is about 1 percent larger.

Summary

An experiment verifying the performance of a tapered-wiggler FEL was described in which electron-beam extraction matching theoretical predictions was observed. Deceleration of individual electrons by an amount approximately equal to the energy taper of the wiggler is observed as in our earlier experiments, a net deceleration of 4 percent is observed, and agreement is found between predicted and observed energy spectra. Electron-beam extraction efficiency is measured as a function of electron beam energy and CO₂ laser beam power and the results are consistent with predictions of performance at the theoretical limitations.

Acknowledgments

The authors wish to acknowledge the assistance of R.W. Nelson and J.M. Ross of Mathematical Sciences Northwest, Inc., and L. Tyson and A.D. Yeremian of Boeing Aerospace Company.

This work was supported in part by The Office of Naval Research under contract N00014-82-C-0704 and by the Air Force Office of Scientific Research under contract F49620-81-C-0079.

References

1. D.A.G. Deacon, L.R. Elias, J.M.J. Madey, G.J. Ramian, H.A. Schwettman, and T.I. Smith, "First Operation of a Free-Electron Laser," *Phys. Rev. Lett.* **38**, 892 (1977).
2. N.M. Kroll, P.L. Morton, and M.N. Rosenbluth, "Variable Parameter Free-Electron Laser," in *Free-Electron Generators of Coherent Radiation*, edited by S.F. Jacobs (Addison-Wesley Publishing Company, Reading, Mass., 1980) pp. 113-145.
3. J.M. Slater, J. Adamski, D.C. Quimby, T.L. Churchill, L.Y. Nelson, and R.E. Center, "Electron Spectrum Measurements for a Tapered-Wiggler Free-Electron Laser," *IEEE J. Quantum Electron.*, **QE-19**, 374 (1983).
4. R. Warren, B. Newnam, J. Winston, W. Stein, L. Young, and C. Brau, "Results of the Los Alamos Free-Electron Laser Experiment," *IEEE J. Quantum Electron.*, **QE-19**, 391 (1983).
5. D.A. Swenson, "Acromatic Translation System for Charged-Particle Beams," *Rev. Sci. Instr.* **35**, 608 (1964).
6. G. Mavrogenes, M.B. James, R.F. Koontz, and R.H. Miller, "Beam Measurements on Argonne Linac for Collider Injector Design," *Proc. of 11th International Conference on High-Energy Accelerators*, CERN, Geneva, Switzerland, July 7-11, 1980, pp. 481-485.
7. J.E. Clendenin, G.A. Loew, R.H. Miller, J.L. Pellegrini and J.B. Truher, "Single Bunch Beam Measurements for the Proposed SLAC Linear Collider," *IEEE Trans. on Nucl. Sci.* **NS-28**, 2452 (1981).
8. C.P. Browne and W.W. Beuchner, "Broad Range Magnetic Spectrograph," *Rev. Sci. Instr.* **27**, 899 (1956).

APPENDIX B

Electron-Beam Quality Requirements for Tapered-Wiggler Free-Electron Lasers

D.C. Quimby and J.M. Slater

Mathematical Sciences Northwest, Inc.
2755 Northup Way, Bellevue, Washington 98004

Abstract

A general approach to optimization of the free-electron laser interaction is used to develop the scaling of emittance and energy spread requirements for tapered wigglers optimized for highest optical gain at fixed e-beam energy extraction. The required e-beam properties for a high extraction oscillator are found to be quite stringent at visible wavelengths, but state-of-the-art accelerators should be sufficient. The applicability of various methods of emittance acceptance enhancement is examined. One very promising option is a magnet canting scheme for providing two-plane focusing in planar wigglers. Two-plane focusing relaxes the severe emittance requirement resulting from the need to maintain spatial overlap between the optical beam and the free-expanding e-beam. In addition, options for adjusting various system parameters for enhanced emittance acceptance, at reduced gain per unit current, are explored.

I. Introduction

The tapered-wiggler free-electron laser (FEL) concept may lead to development of a high efficiency, tunable laser. The large e-beam energy extraction possible with wiggler tapering may lead to high efficiency systems through reduction of e-beam energy recovery or recirculation requirements. A key technology issue in applying this technology at short photon wavelengths concerns the capability of linear accelerators to produce electron beams with the small emittance and energy spread required by the FEL. The limited e-beam power available with small emittance and energy spread, together with the high optical power required for energy extraction, limit the tapered-wiggler single-pass gain. The motivation of this paper is to gain a proper understanding of the optimization and scaling of the tapered-wiggler FEL gain including limitations due to emittance and energy spread, to aid in development of a high efficiency, high-power FEL at visible wavelengths. Emittance requirements for untapered wigglers driven by linear accelerators have previously been developed by Smith and Madey⁽¹⁾ and Dattoli, et al.⁽²⁾ In addition, Madey has discussed the emittance requirements for storage-ring driven FELs.⁽³⁾

The general approach to optimization of the FEL interaction strength described in Section II is used to develop the scaling of emittance and energy spread requirements for optimized planar wigglers. Emittance and energy spread acceptance limits are defined based in part on numerical simulation of the degradation of FEL interaction strength due to these effects. Results of the gain optimization analysis are presented in Section III. The required e-beam properties are found to be quite stringent at visible wavelengths, but angular canting of the magnets to provide equal two-plane focusing is shown to enhance emittance acceptance. In addition, possible tradeoffs are examined which relax the e-beam emittance and energy spread requirements, but produce lower gain per unit e-beam current. Implications are addressed in Section IV.

II. Gain Optimization

A general approach to the problem of optimization of the FEL interaction is developed in this section, leading to specific requirements for the wiggler and e-beam properties. The gain-extraction product is a useful figure of merit for the tapered-wiggler FEL interaction strength since gain can be evenly traded for extraction (and vice versa) by changing the wiggler taper.

A. Gain-Extraction Product

The gain-extraction product, ξ , has been shown⁽⁴⁾ to be given by (cgs units)

$$\xi = \frac{128\pi^2 e}{mc^3} (\delta \sin\psi)^2 \gamma I \chi^2, \quad [1]$$

where

$$\chi = \frac{1}{\alpha} \frac{h}{\lambda_w} \frac{a_w}{[1 + a_w^2]} \frac{\ln[q + [1 + q^2]^{1/2}]}{(1 + q^2)^{1/2}}, \quad [2]$$

δ is the fraction of electrons trapped in the ponderomotive well, $\sin\psi$ is the average sine of the phase angle for trapped electrons, γ is the electron energy in units of the rest mass mc^2 , I is the electron current, α is the ratio of magnet half-gap h to the 1/e photon beam amplitude radius w_e at the wiggler entrance and exit, $a_w = eB_0\lambda_w/2^{3/2} \pi mc^2$, B_0 is the peak B-field, λ_w is the wiggler wavelength, $q = L_w/2Z_R$, L_w is the wiggler length, and Z_R is the Rayleigh range of the photon beam. Equation [1] does not include degradation of the gain-extraction product due to energy spread and emittance; these effects will be introduced later. Equation [1] is derived under the assumptions of small fractional change in the resonant energy,

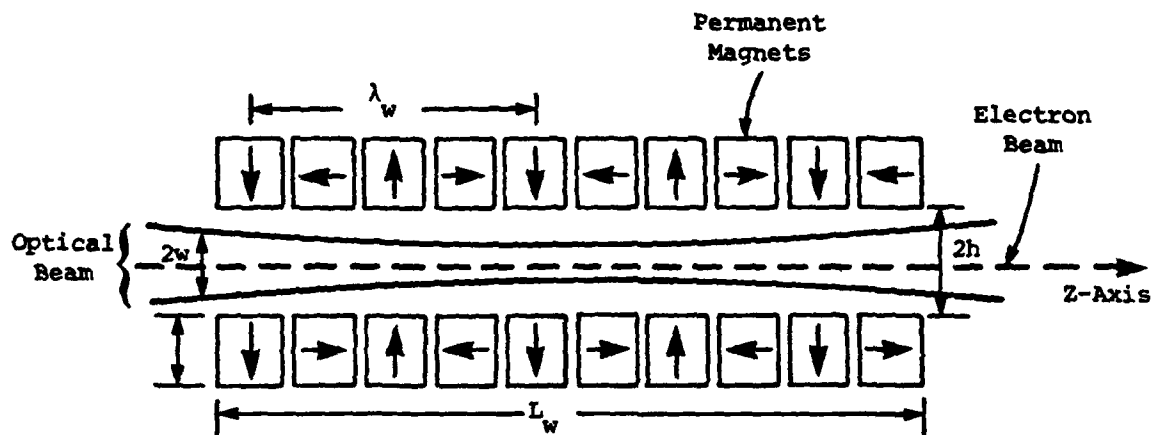
$$\gamma_r^2 = \frac{\lambda_w}{2\lambda_s} [1 + a_w^2], \quad [3]$$

and low gain. The electron dynamics are idealized by assuming that trapped electrons behave as the synchronous-phase particle⁽⁵⁾ does, so that, in essence the optimization is for a single electron traveling along the wiggler axis.

The assumed geometry is shown in Figure 1. A diffraction-limited photon beam is focused in the center of a planar wiggler. A Halbach⁽⁶⁾ magnet configuration is used. The permanent magnets have polarization vectors oriented as indicated by the arrows in Figure 1. In order to properly reflect the physical limitations of developing large magnetic fields in this geometry, we write a_w in terms of the basic magnet parameters h , λ_w , and the remanent magnetization, B_r . For the magnet bar height $g = 3\lambda_w/8$ and no gaps between neighboring magnets, the calculated field may be expressed as⁽⁶⁾

$$a_w = 1.07 \times 10^{-4} B_r \lambda_w e^{-2\pi h/\lambda_w} \quad [4]$$

Using a typical peak value of $\delta \sin \psi$ of 0.26 (based on numerical simulation results), a conservative clearance factor α of 2, and $B_r = 9000$ G typical of SmCo_5 magnets, the gain-extraction product is now a function of L_w , λ_w , h , λ_g , Z_R , and I . Optimization of expression Equation [1] depends on which parameters are fixed and which are varied to produce the maximum. The case of λ_g , L_w , and I fixed is considered here. These choices allow the wiggler length to be held to a practical value and assume that the peak current available is limited. It is to be noted that when optical component damage is an issue, Z_R may be a more useful independent parameter than L_w , since Z_R partly determines the beam size on the resonator mirrors. Fixing λ_g , L_w , and I apparently leaves a three-dimensional surface to be examined, but h and Z_R are not independent of one another (due to the fixed clearance factor α) and the resulting two-dimensional space is easily analyzed to find the system parameters yielding the maximum gain-extraction product.



82 06271

Figure 1. FEL Geometry for Optimization Analysis.

The e-beam energy spread and emittance requirements can also be determined as a function of the system parameters. The allowable energy spread is determined by the requirement that it cannot exceed the ponderomotive bucket full height. Similarly, the allowable emittance is set by the combined requirements that the effective energy spread due to emittance be less than the bucket height and that the electron and photon beams overlap spatially.

B. Energy Spread Requirements

For a tapered-wiggler, the energy spread must be less than the ponderomotive bucket height full width, given by⁽⁵⁾

$$H = \left[\frac{\Delta\gamma}{\gamma} \right]_{\text{Bucket}} = 2 \left[\frac{2\lambda_s e_s a_w F[\psi_r]}{\pi [1 + a_w^2]} \right]^{1/2}, \quad [5]$$

where $e_s = eE_0/2^{1/2}m_0c^2$ is the normalized rms E-field, $F(\psi_r) = \cos\psi_r - (\pi/2 - \psi_r)\sin\psi_r$, and parameter ψ_r is the phase angle in the ponderomotive potential well for the electron whose energy loss rate exactly matches that of the wiggler resonant energy. A phase angle of about 40 degrees maximizes the product of trapping fraction and bucket deceleration rate for the case of a monoenergetic, zero emittance beam. At photon flux levels too low to result in trapping, the allowable energy spread corresponds to the homogeneous small-signal linewidth. Using the linewidth defined by Brau⁽⁷⁾ for the linearly tapered wiggler gives an allowable energy spread of

$$\frac{\Delta\gamma}{\gamma} = \frac{1}{2} \frac{\Delta\lambda_s}{\lambda_s} = \left[\frac{\lambda_w}{\pi L_w} \frac{\Delta\gamma_r}{\gamma_r} \right]^{1/2}, \quad [6]$$

where $\Delta\gamma_r$ is the resonant energy change of the wiggler taper. It is of interest to compare the energy spread requirements at small-signal and saturated flux levels. Since saturation (the onset of trapping) occurs for an E-field value of roughly

$$e_s = \frac{\gamma_r^2}{a_w L_w} \frac{\Delta \gamma_r}{\gamma_r}, \quad [7]$$

the bucket full width at saturation is, for $\psi_r \approx 40^\circ$,

$$\left[\frac{\Delta \gamma}{\gamma} \right]_{\text{Bucket}} \approx \left[\frac{\lambda_w}{\pi L_w} \frac{\Delta \gamma_r}{\gamma_r} \right]^{1/2}, \quad [8]$$

which is equal to the equivalent energy-width due to the small-signal linewidth. Thus, the energy spread requirements for a linearly tapered wiggler at small-signal and saturated conditions are identical. At flux levels well above the onset of saturation, the energy spread requirements relax as the bucket size grows.

C. Emittance Requirements

The allowable emittance in the focusing plane of a planar wiggler is often set by the requirement that the effective energy spread due to emittance be less than the bucket height. For such cases, in which spatial overlap is not the limiting factor, determination of the allowable emittance is based on the principle that electrons with slightly different trajectories interact in the same way as electrons with identical trajectories but slightly different energies. The trajectory difference is of course related to the emittance, with the consequence that the allowable emittance can be directly related to the allowable energy spread.

The effective energy spread due to emittance may be determined by examining the variation in transverse momentum and B-field experienced by an electron which executes the betatron orbit⁽⁸⁾ of maximum amplitude. The effective energy spread full width is found to be

$$\left(\frac{\Delta\gamma}{\gamma}\right)_{\text{Equiv}} = \begin{cases} \frac{k_w^2 a_w^2 \epsilon_N}{2\pi\gamma k_\beta (1 + a_w^2)} & k_\beta < \frac{a_w k_w}{\gamma} \\ \frac{\gamma k_\beta \epsilon_N}{2\pi (1 + a_w^2)} & k_\beta > \frac{a_w k_w}{\gamma} \end{cases} \quad [9]$$

where $k_w = 2\pi/\lambda_w$ is the wavenumber of the wiggler, k_β is the wavenumber for betatron oscillations resulting from the distributed focusing along the wiggler, and the normalized emittance ϵ_N is defined as $\gamma\pi r\theta$ where r is the radius and θ is the half-angle at any beam focus. The two terms in Equation [9] are due to detuning from the resonance condition by the B-field gradient and by the trajectory angle associated with the betatron orbit, respectively. The minimum energy spread occurs for a focusing strength $k_\beta = a_w k_w / \gamma$ which is precisely the natural value for a planar wiggler. In that case the detuning from the resonant condition for each electron is independent of axial position. Electron trapping will be relatively inefficient when the effective energy spread given by Equation [9] exceeds the bucket full width. For other focusing strengths, the energy spread given in Equation [9] is actually a peak value achieved only at certain points in the betatron orbit. In this case detrapping will occur if the energy spread exceeds the bucket height and the synchrotron wavelength is much shorter than the betatron wavelength. The latter condition is marginally satisfied for the systems of interest. The requirement that the effective energy spread be less than the well depth will hereafter be called the "bucket constraint."

In some cases, the allowable emittance may be limited by the need to maintain spatial overlap in the focusing plane. This occurs when the allowable e-beam radius based on the bucket constraint exceeds the photon beam waist size. The e-beam radius given by the distributed focusing in the wiggler is

$$r_{\text{eb}} = \left[\frac{\epsilon_N}{\gamma\pi k_\beta} \right]^{1/2} \quad [10]$$

This result is valid when the electrons are optimally focused at the wiggler entrance, in which case the e-beam radius is length independent within the wiggler. As shown later, a reasonable condition for minimal gain degradation at fixed extraction is the requirement that the e-beam radius be less than the 1/e photon intensity radius, that is, $r_{eb} < w/2^{1/2}$, where w is the 1/e photon amplitude radius. This requirement leads to an allowable emittance of

$$\epsilon_N < \frac{\gamma \lambda_s Z_R k_\beta}{2} . \quad [11]$$

The requirement to maintain spatial overlap between the electron and photon beams shall be called the "overlap constraint."

In the free-expanding plane, spatial overlap is generally the limiting constraint. Proper overlap may be provided by matching the photon and e-beam envelope shapes, leading to the requirement

$$\epsilon_N < \frac{\gamma \lambda_s}{2} . \quad [12]$$

Comparison with Equation [11] shows that the emittance requirement for overlap is more severe in the free-expanding plane for those systems which have $Z_R k_\beta$ greater than unity. This constraint may be relaxed if e-beam focusing is provided in the nominally free-expanding plane.

D. Two-Plane e-Beam Focusing

Two-plane focusing can be provided in a planar wiggler either by external quadrupoles or by angular rotation^(9,10) of the wiggler magnets. The former method allows a readily adjustable focal strength but requires precise alignment to insure that the wiggler and focusing elements are coaxial. Otherwise the beam will be steered off-axis and a betatron oscillation excited. The latter method ensures that the focusing properties are properly aligned and, in principle, could be used with hybrid (SmCo₅ plus steel) wigglers which do not allow linear superposition

of external fields. Two-plane focusing using magnet canting has recently been experimentally demonstrated in a SmCo_5 wiggler.⁽¹⁰⁾ When focusing is introduced in the wiggle plane, the focal strength in the nominally focusing plane is reduced according to

$$k_{\beta x}^2 + k_{\beta y}^2 = k_{\beta 0}^2, \quad [13]$$

where $k_{\beta x}$ and $k_{\beta y}$ are the wiggle plane and nominally focusing plane betatron wavenumbers, respectively, and $k_{\beta 0} = a_w k_w / \gamma$ is the nominal betatron wavenumber in the absence of canting. The best spatial match with a cylindrically symmetric photon beam occurs with equal two-plane focusing, in which case

$$k_{\beta x} = k_{\beta y} = \frac{a_w k_w}{2^{1/2} \gamma}. \quad [14]$$

E. Confirmation of Emittance and Energy Spread Requirements

Equations [5], [9], [11], and [12] define energy spread and emittance requirements. The actual degradation in FEL interaction strength for energy spread and emittance values which approaches these limits is computed in this section. Electrons which are detuned to near the edge of the bucket or experience lower E-fields due to off-axis trajectories experience a somewhat weaker interaction.

These effects may be quantified by numerical integration of the equations for electron energy loss and electron phase in the ponderomotive potential of the FEL interaction.

$$\begin{aligned} \frac{d\gamma}{dz} &= \frac{-e_s a_w \sin(\psi - \phi)}{\gamma} \\ \frac{d\psi}{dz} &= k_w - \frac{k_s}{2\gamma^2} \left[1 + a_w^2 + \gamma^2 \left[\theta_x^2 + \theta_y^2 \right] \right]. \end{aligned} \quad [15]$$

The effects of emittance are included in a two-step process. First the transverse angles θ_x and θ_y of the electron orbits, the optical E-fields,

and the wiggler B-fields experienced by each electron are computed as a function of axial position, including the off-axis motion but ignoring the small effect of the FEL interaction on the trajectory. Then the energy loss is determined in a one-dimensional integration of the coupled equations Equation [15] using the previously computed angles and E and B-fields for each electron. The emittance phase space is assumed to be uniformly filled. The electron and optical beams are assumed to be optimally focused and coaligned and the optical beam is assumed to be diffraction-limited, in which case, in the low-gain approximation, the E-field amplitude and phase varies spatially according to⁽¹¹⁾

$$e_s(r, z) = e_s^0 \left[\frac{w_0}{w(z)} \right] e^{-(r/w(z))^2} \quad [16]$$

$$\phi(r, z) = \tan^{-1}[z/z_R] - \left[\frac{r}{w(z)} \right]^2 [z/z_R] ,$$

where e_s^0 is the normalized on-axis E-field at the waist, $w(z) = w_0 (1 + [z/z_R]^2)^{1/2}$, w_0 is the 1/e photon amplitude radius at the waist, and z is measured from the waist location. The spatial B-field variation is included by assuming constant k_w with a_w tapered for constant resonant phase

$$a_w(y, z) = a_w^0 \{ \cosh k_w y , \quad [17]$$

where

$$\zeta(z) = 1 - \frac{\Delta a_w}{a_w^0} \frac{\ln \left[\frac{-q + (1 + q^2)^{1/2}}{z/z_R + [1 + (z/z_R)^2]^{1/2}} \right]}{\ln \left[\frac{-q + (1 + q^2)^{1/2}}{q + (1 + q^2)^{1/2}} \right]} , \quad [18]$$

a_w^0 is the a_w value at the entrance, and Δa_w is the change in a_w along the wiggler length.

Numerical calculations have been completed for the preliminary point design of a 0.5 μm oscillator experiment given in Table 1. This design incorporates a SmCo_5 wiggler of 5 m length and an e-beam energy of 120 MeV. The wiggler design assumes two-plane e-beam focusing provided by the wiggler magnets.

Results of the numerical electron tracking calculations are given in Figure 2. The effect of emittance is to require an overall higher photon power to achieve a given level of extraction. Since overlap is the more severe emittance constraint (see Table 1), the higher photon flux compensates for the relatively low E-fields experienced by most electrons due to their off-axis trajectories. While the additional E-field required to achieve extraction at higher emittance is modest, the associated increase in photon power may be significant. About 50 percent gain degradation is found at the overlap constraint of $r_{\text{eb}} = w_0/2^{1/2}$ defined previously. A similar gain degradation factor is obtained for an energy spread which just matches the full bucket height. These results show that the previously defined energy spread and emittance requirements correspond to defining the acceptance as the value which degrades the FEL interaction strength by one-half.

III. Results and Discussion

The optimization analysis developed in the previous section is used to define the parameters for systems optimized for peak gain at fixed extraction. Energy spread and emittance acceptance values are identified for these systems. Later, tradeoffs which lower the gain but enhance acceptance are examined.

A. Gain-Optimized Systems

The calculated optimum gain and corresponding e-beam energy are given in Figure 3. The gain values are in units of percent optical power increase per ampere of e-beam current. They apply to 5 percent extraction,

Table 1

PRELIMINARY POINT DESIGN FOR 0.5 μ m
OSCILLATOR EXPERIMENT

E-Beam Energy	120 MeV
Peak Current	100 A
Wiggler Length	5 m
Taper ($\Delta\gamma_T/\gamma_T$)	12%
Wiggler Wavelength	2.18 cm
Peak Magnetic Field	8.7 kG
a_w	1.25
Full Gap	0.36 cm
Rayleigh Range	2.2 m
Instantaneous Photon Power at 5% Extraction	3.3 GW
Normalized Emittance Acceptance Based on Overlap ^a	0.014 cm-rad
Normalized Emittance Acceptance Based on Effective Energy Spread ^a	0.048 cm-rad
Energy Spread Acceptance ^a	1.5%
Single-Pass Gain at 5% Extraction ^b	18%

^a Assumes equal two-plane focusing provided by wiggler,
and 50 percent gain loss at fixed extraction.

^b Assumes $\epsilon_N = 0.01$ cm-rad, Energy Spread = 1 percent.

AD-A144 053

TAPERED-WIGGLER FREE-ELECTRON LASER OSCILLATOR PROGRAM

2/2

(U) MATHEMATICAL SCIENCES NORTHWEST INC BELLEVUE WA

J SLATER ET AL. MAY 84 NSNM-C. 11. 198. 01

UNCLASSIFIED

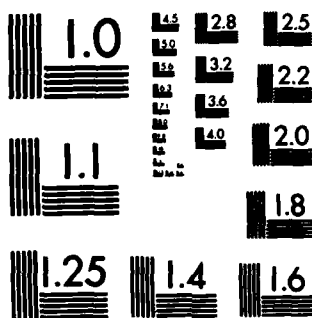
AFOSR-TR-84-0623 F49620-81-C-0079

F/G 20/5

NL

END

PAID



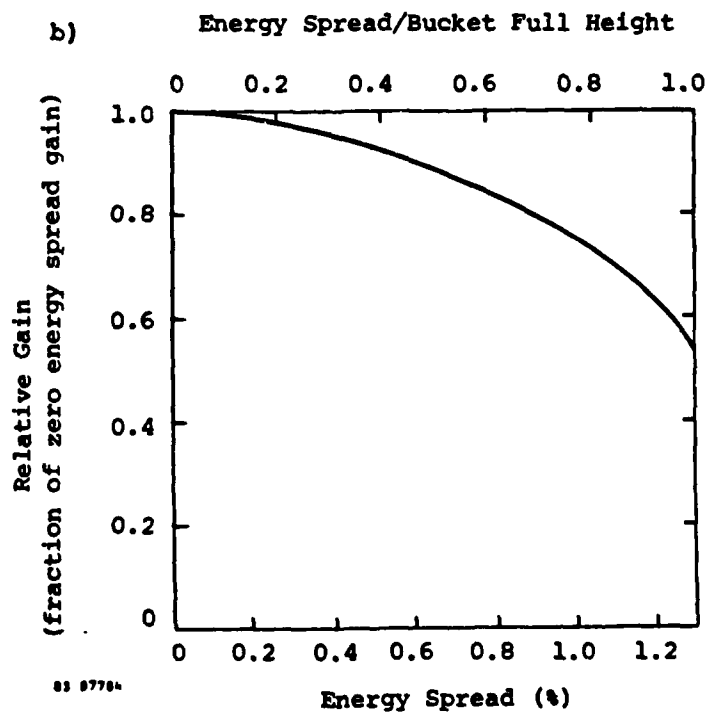
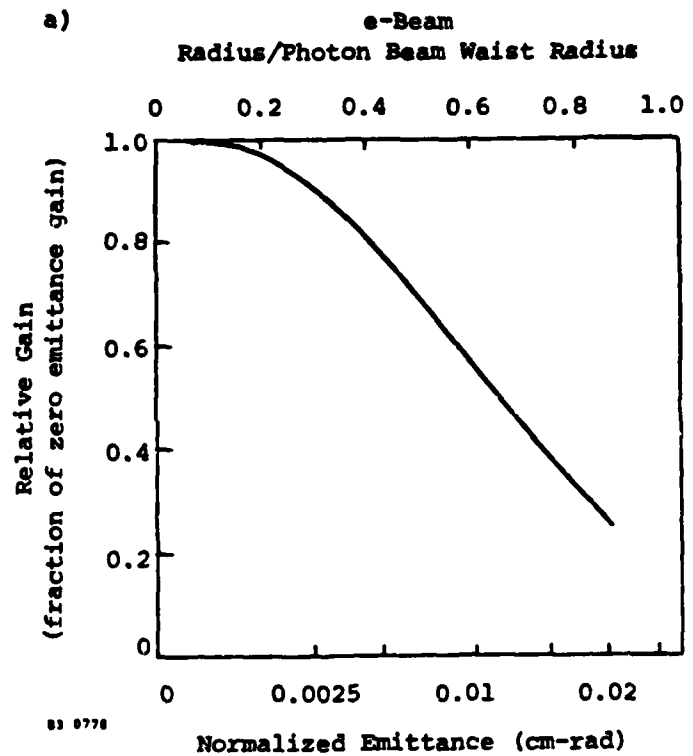


Figure 2. Gain Degradation at Fixed Extraction Due to (a), Finite Emittance, and (b), Energy Spread. Assumed Conditions Given in Table 1.

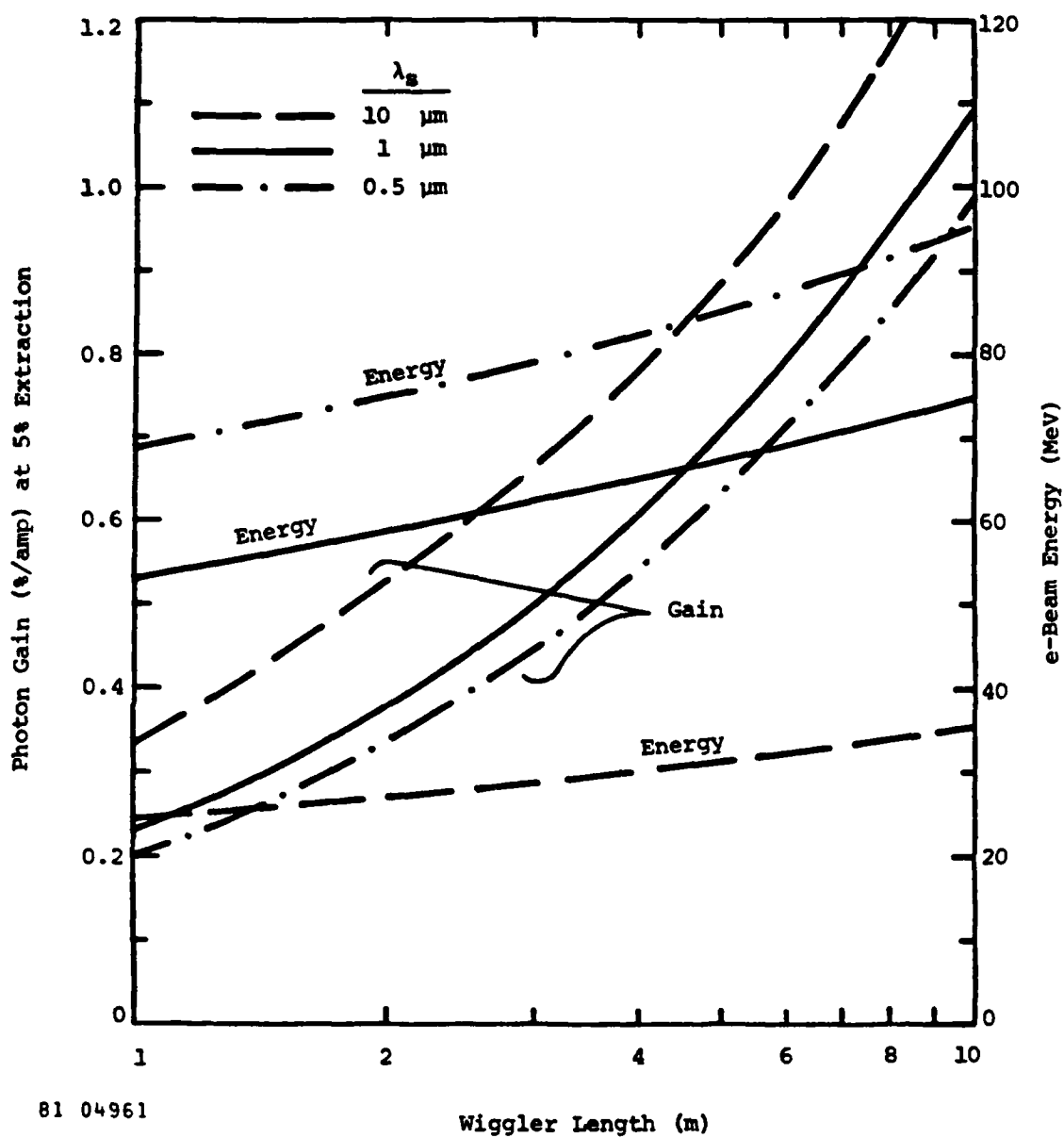


Figure 3. Maximum Single-Pass Gain and Optimum E-beam Energy.

but can be trivially scaled to other extraction values since the gain-extraction product is constant. Comparison with the numerical tracking code described previously shows that these gains are generally accurate to within 30 percent. The curves clearly indicate that higher gains may be obtained with longer wigglers. This results primarily from the term $h a_w / \lambda_w (1 + a_w^2)$ in Equation [2], which increases in value as the bore size h increases. The gain is not a strong function of the photon wavelength. This is due to our assumption of constant current, which means that the weaker interaction at shorter wavelengths is partially offset by the larger e-beam power at higher γ values. The associated optical powers, P_g , for 5 percent extraction are given in Figure 4. These powers can be scaled to extraction values, η , other than 5 percent by noting that η^2/P_g is constant.

Optimum values of the dependent parameters for the 1 micron photon wavelength case are shown in Figure 5. Parameters L_w/Z_R and a_w remain roughly constant while the ratio h/λ_w varies significantly with wiggler length. It is interesting to note that the optimum a_w value is less than unity for the conditions examined and for this particular choice of the independent parameters. An optimum a_w value of 1.0 is frequently reported in the FEL literature, and the latter value does result from this optimization when λ_w is taken to be independent (i.e., fixed). Certainly one can pick λ_w to be a system constraint if so desired, but equivalent wiggler performance will then require slightly longer wigglers than for the case where L_w is constrained and λ_w is optimized.

Calculated values of the energy spread requirements for gain-optimized systems are shown in Figure 6. These curves apply to the 5 percent extraction case, but may be scaled to other values by noting that the bucket height varies proportional to $\eta^{1/2}$. The bucket depth dependence on photon wavelength is weak because the $\lambda_g e_g$ product in Equation [5] does not vary substantially. These bucket widths have been calculated for the field at the entrance or exit of the wiggler. From the

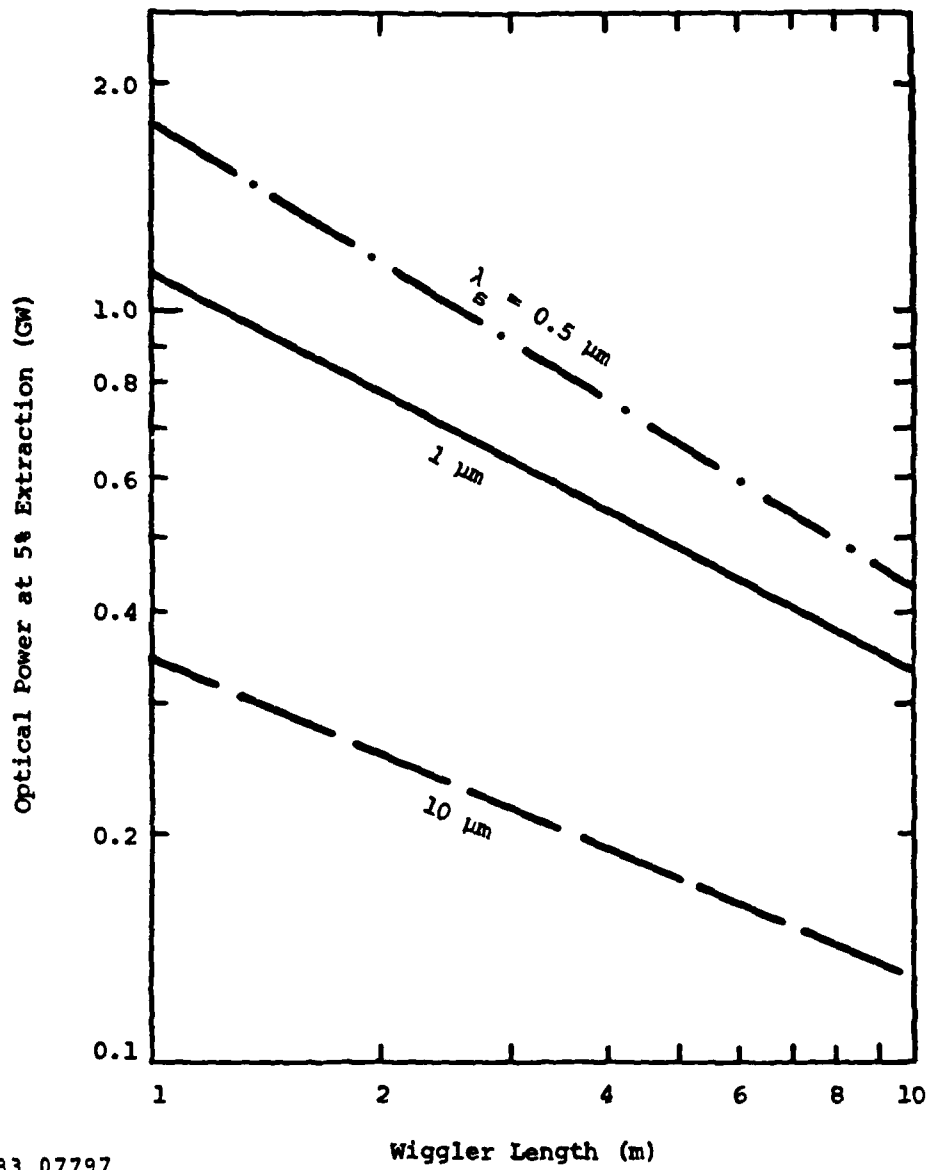


Figure 4. Optical Power Under Peak Gain Conditions.

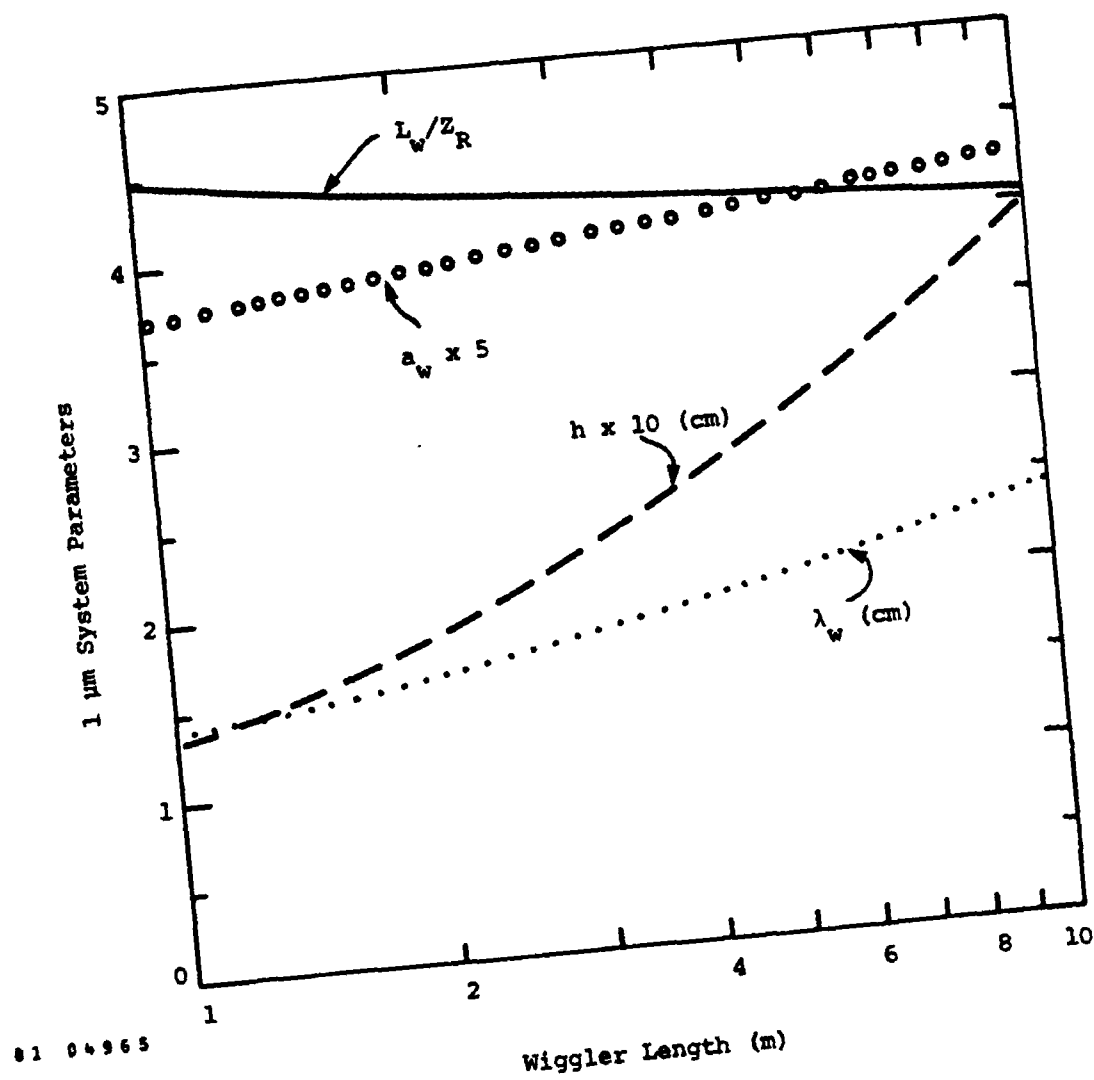
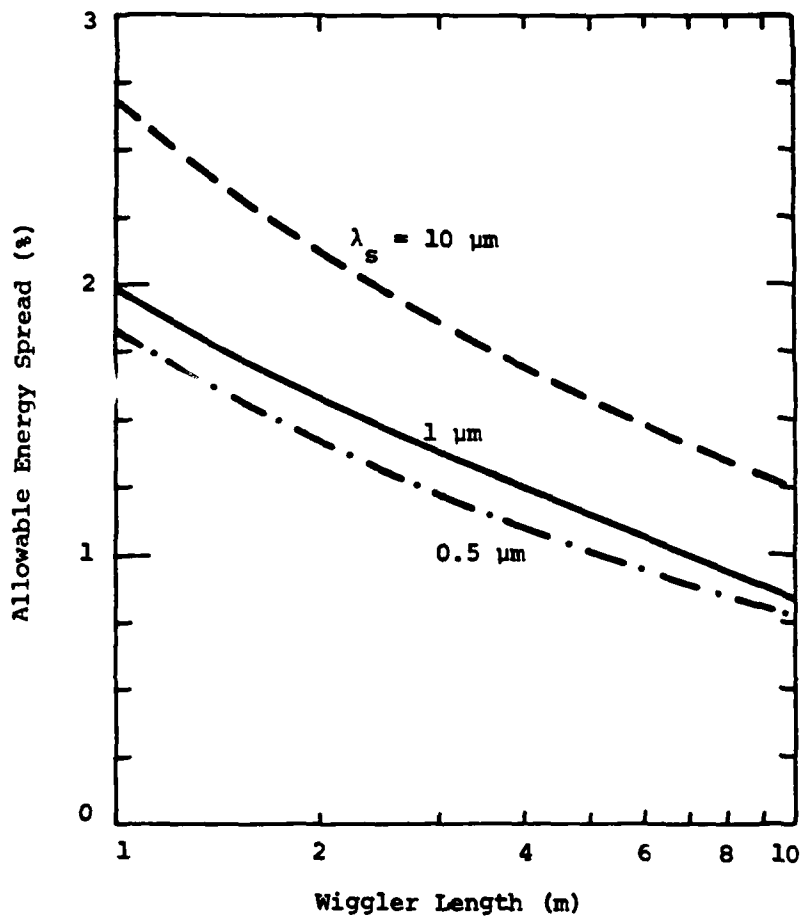


Figure 5. Optimum Wiggler Parameters for Maximum Gain at $\lambda_s = 1 \mu\text{m}$.



83 07675

Figure 6. Energy Spread Requirement at Optimum Gain Conditions and 5 Percent Extraction Based on Equating Maximum Energy Spread to Bucket Height.

$L_w/2R$ values of Figure 5, the bucket at the wiggler center is typically 50 percent larger.

The emittance values which just fill the bucket and which just meet the overlap requirement are shown in Figure 7. Clearly the emittance requirement for overlap is the more severe constraint and becomes particularly serious at shorter photon wavelengths. This constraint may be relaxed somewhat if e-beam focusing is provided in the nominally free-expanding plane.

B. Two-Plane e-Beam Focusing

The allowable emittance for gain optimized systems with equal two-plane focusing is shown in Figure 8. As with single-plane focusing, the allowed emittance is generally limited by spatial overlap constraints. For short wiggler lengths, the overlap obtained with two-plane focusing and an axially independent beam size is worse than the overlap which can be achieved with no wiggler focus and a slightly converging input beam. In this case the emittance requirement shown is identical to that in Figure 7 for single-plane focusing. For $\lambda_g = 10 \mu\text{m}$, the allowed emittance is limited by the bucket constraint for wiggler lengths greater than 8 meters. For the longer wiggler lengths, the emittance acceptance is considerably enhanced relative to the single-plane focusing case. Since the actual improvement in useful current scales as ϵ^2 , two-plane focusing represents a significant advantage.

The overlap problem may be further affected by additional external focusing along the wiggler length. Such additional focusing may be useful whenever the natural focus of the wiggler produces an effective energy spread that does not exceed the bucket depth. In Figure 9, the emittance requirements based on the bucket (Equation [9]) and overlap (Equation [11]) constraints are shown as a function of focusing strength by the dashed and solid lines, respectively. This example case has $\lambda_g = 0.5 \mu\text{m}$, 5 percent extraction, and $L_w = 5 \text{ m}$. Since the emittance acceptance of the wiggler is

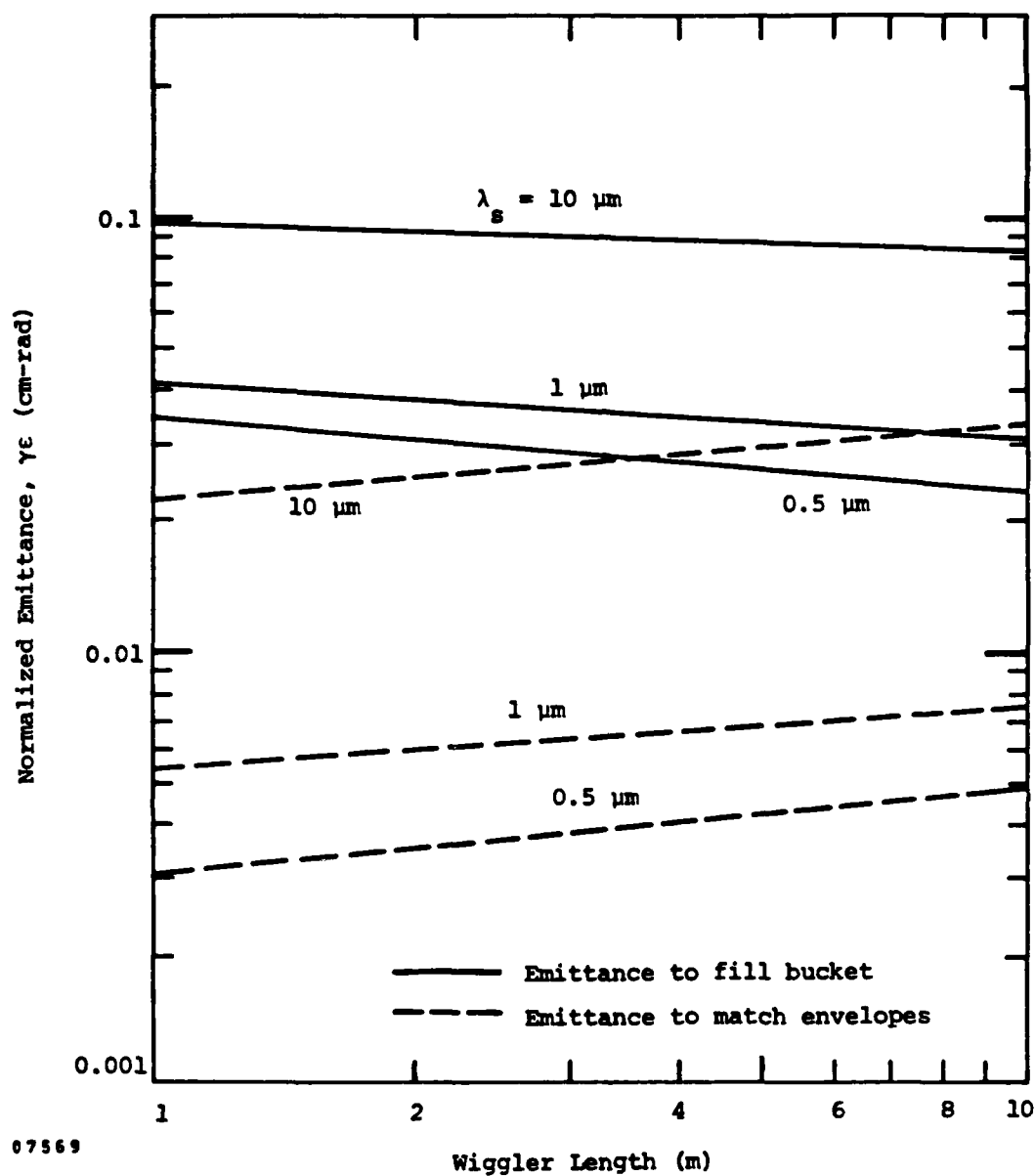
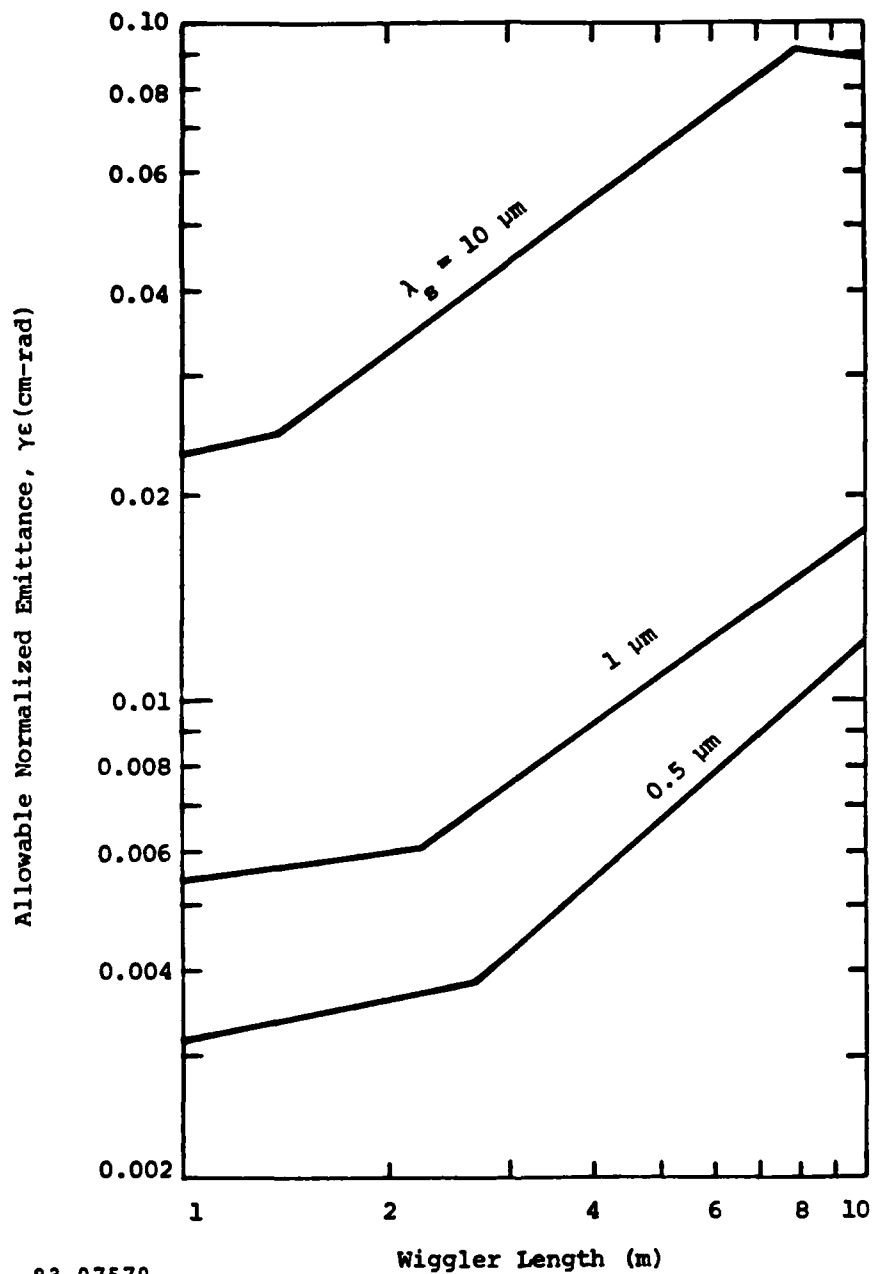


Figure 7. Normalized Emittance to Fill Bucket in Focusing Plane and for Spatial Overlap in Free-Expanding Plane.



83 07570

Figure 8. Emittance Acceptance of Gain-Optimized Systems with Equal Two-Plane Focusing Provided by Wiggler. Bucket constraint based on 5 percent extraction.

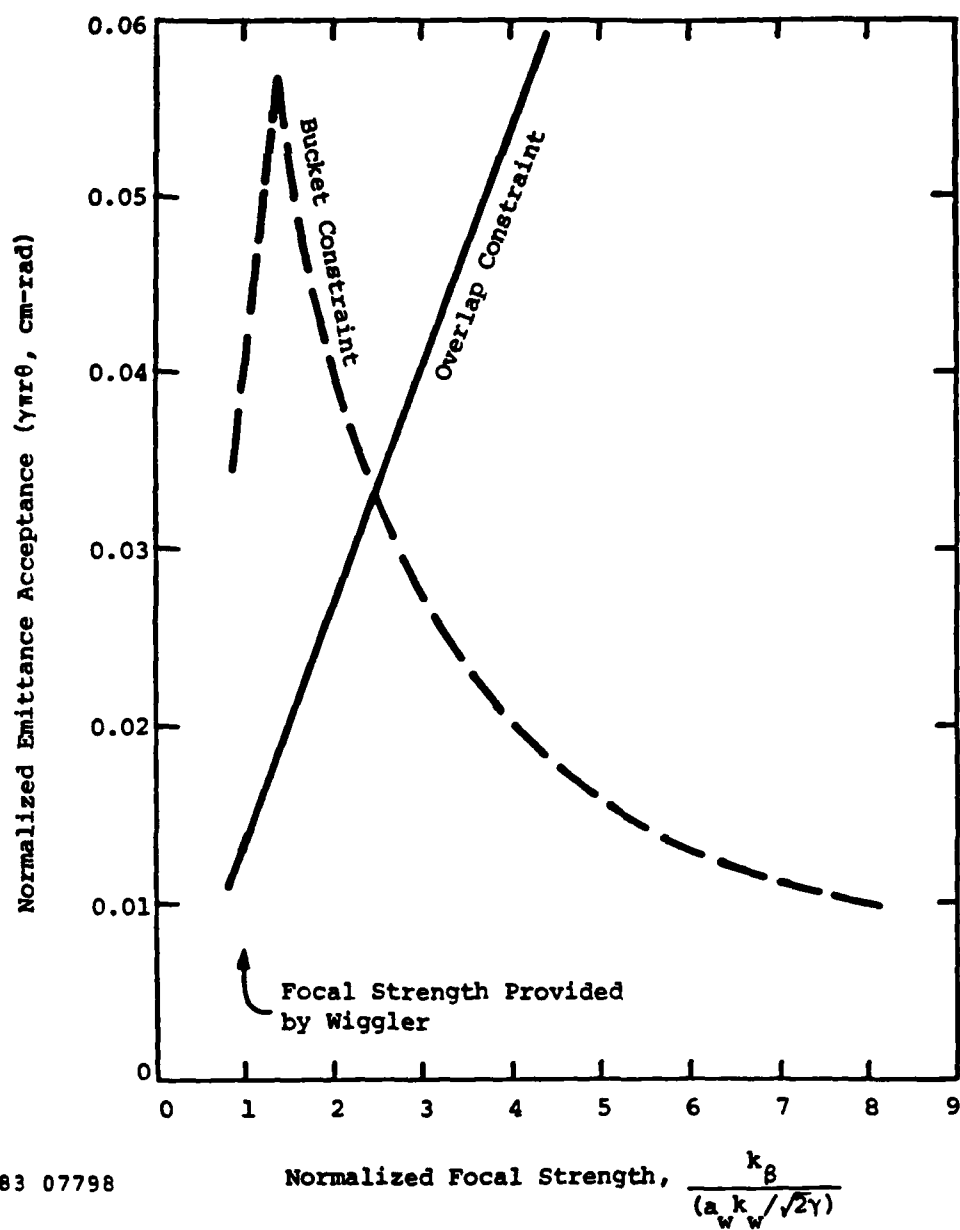


Figure 9. Emittance Acceptance for Various Levels of Equal Two-Plane Focusing. Bucket and overlap constraints as defined in Section III. Assumed wiggler parameters given in Table 1.

the minimum of the two constraints, the optimum operating point is expected to be at their intersection. Strong external focusing appears to provide a promising means of emittance acceptance enhancement.

C. Optimization for High Emittance

In the previous section systems were optimized for highest gain under the assumption of zero emittance, and the emittance acceptance was then computed. For nonzero emittance values, the wiggler parameters specified do not provide the highest possible gain. An optimization for larger emittance values is now considered for systems with equal two-plane focusing provided by the wiggler. For simplicity the analysis is tailored to cases where the equivalent energy spread due to emittance is unimportant, as is the case for the following 0.5 μm calculations.

The function to be optimized is equivalent to that considered previously (Equation [1]), except that new factors are added to reflect the degradation of gain at fixed extraction with increasing emittance and energy spread. For a given fractional energy spread $\Delta E = \Delta\gamma/\gamma$ and emittance ϵ_N , these factors depend on the other system parameters and are given by

$$f_{\Delta E} = \begin{cases} 1 - \frac{1}{2} \left[\frac{\Delta E}{H} \right]^2 & \frac{\Delta E}{H} < \left[\frac{2}{3} \right]^{1/2} \\ \left[\frac{2}{3} \right]^{3/2} \left[\frac{\Delta E}{H} \right]^{-1} & \frac{\Delta E}{H} > \left[\frac{2}{3} \right]^{1/2} \end{cases} \quad [19]$$

$$f_{\epsilon} = \begin{cases} 1 - \frac{1}{2} \left[\frac{\epsilon_N}{\epsilon_0} \right] & \frac{\epsilon_N}{\epsilon_0} < \frac{4}{3} \\ \frac{16}{27} \left[\frac{\epsilon_N}{\epsilon_0} \right]^{-2} & \frac{\epsilon_N}{\epsilon_0} > \frac{4}{3} \end{cases} \quad [20]$$

where H is the bucket height defined by Equation [5] and ϵ_0 is the

normalized emittance acceptance based on the overlap constraint given in Equation [11]. The functional dependences for lower energy spread and emittance values ($\Delta E/H < (2/3)^{1/2}$, $\epsilon_N/\epsilon_0 < 4/3$) are fits to the numerical results shown in Figure 2. For large energy spread ($\Delta E/H > (2/3)^{1/2}$), the fraction of electrons in the bucket is proportional to $1/\Delta E$, and the proportionality constant is chosen to connect smoothly to the curve in Figure 2(b). This scaling properly refers to cases where energy spread in excess of $(2/3)^{1/2} H$ is filtered out upstream of the wiggler. For large emittance ($\epsilon_N/\epsilon_0 > 4/3$) the fraction of electrons within the optical beam is proportional to ϵ_N^{-2} , and the proportionality constant is chosen to connect smoothly to the curve in Figure 2(a).

The new function to be optimized is then

$$\xi = \frac{128\pi^2 e}{mc^2} (\partial \sin \psi)^2 \gamma I x^2 f_{\Delta E} f_{\epsilon} . \quad [21]$$

As before, this is an expression for the gain at fixed extraction. The two additional parameters ΔE and ϵ_N are taken to be fixed, while, as before, λ_w , h , and Z_R are varied to find the optimum. The results of this analysis for $\lambda_s = 0.5 \mu\text{m}$ are shown in Figure 10. For wiggler lengths over 4 meters, the system parameters adjust to accept normalized emittance values of up to 0.01 cm-rad with no more than 50 percent gain loss. Energy spreads of up to 1 percent result in no more than 50 percent gain loss for wiggler lengths of under 7 meters. Intermediate wiggler lengths of 4 to 7 meters are least sensitive to the combined effects of emittance and energy spread.

Figure 11 shows how system parameters change to accept larger emittance. To provide proper overlap as the emittance is increased, the photon beam size must be increased beyond the optimal zero-emittance size. In addition, the e-beam energy is increased because the equivalent energy spread decreases with γ . The photon beam size increase causes gain loss in two ways. First the total photon power increases proportionally to the beam area so that less energy is extracted per unit photon energy

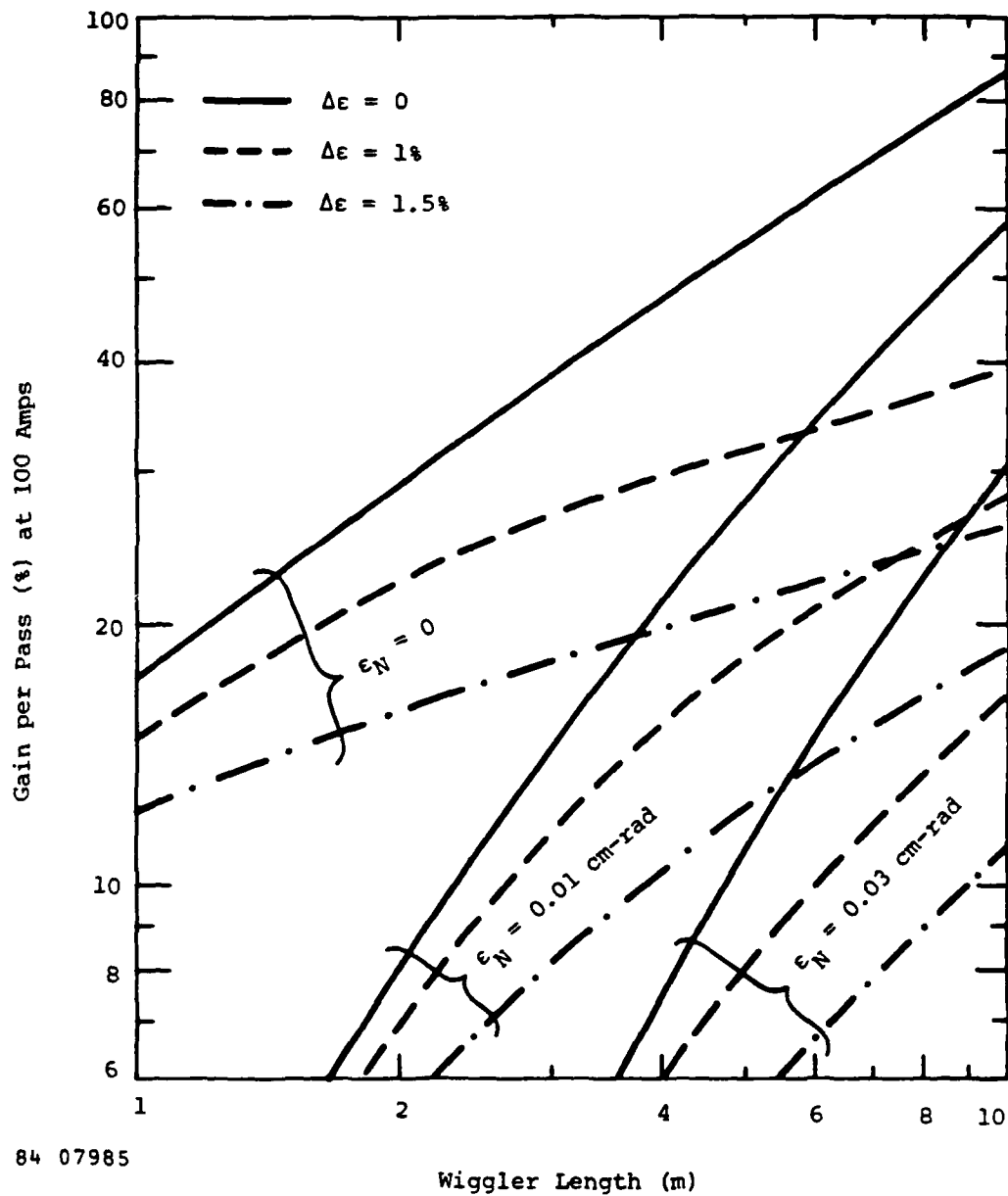


Figure 10. Maximum gain at $\lambda_s = 0.5 \mu\text{m}$ and 5 Percent Extraction for Various Assumed Levels of Emittance and Energy Spread.

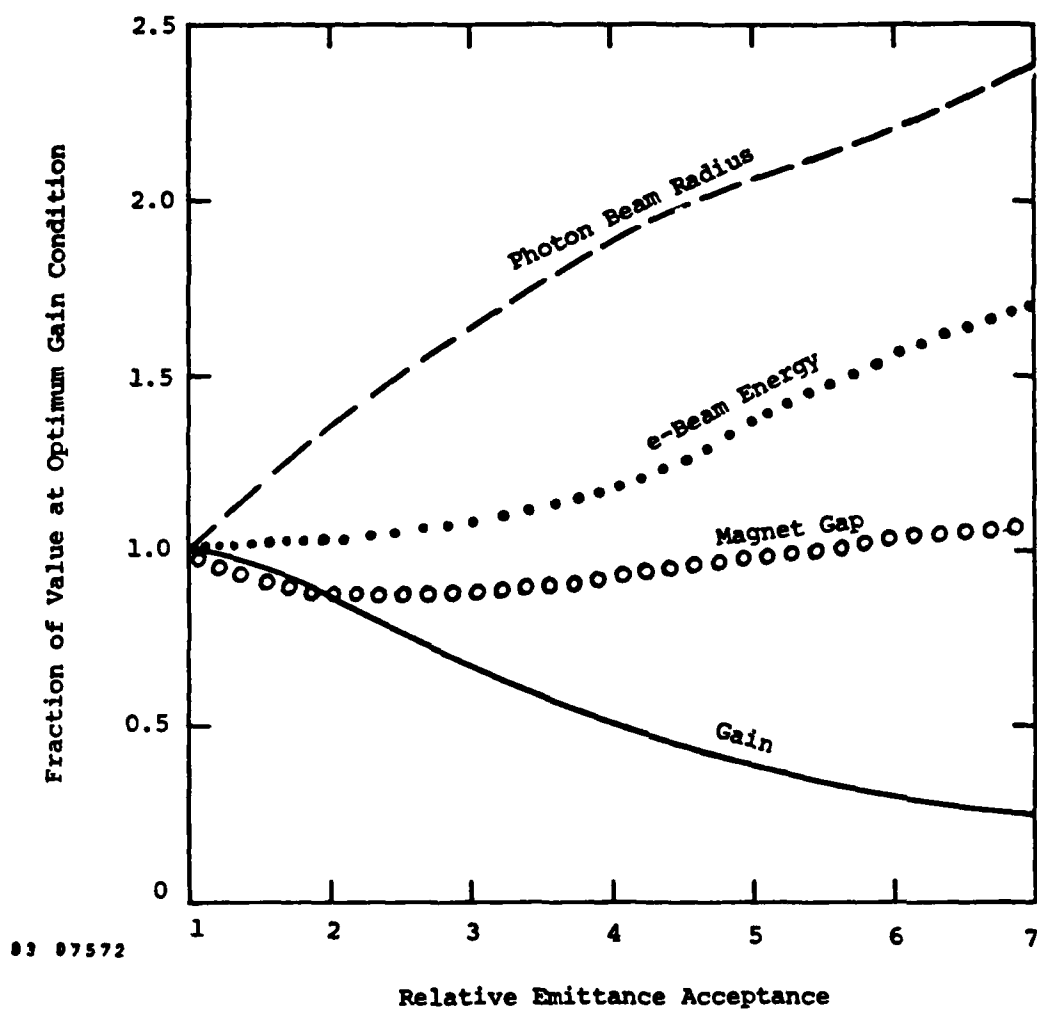


Figure 11. Variation of System Parameters to Accept Larger Emittance While Maintaining as High a Gain as Possible. $L_w = 5$ m, $\lambda_s = 0.5$ μ m, 5 percent extraction, $\Delta E = 0$.

invested. Second, the wiggler bore size must also increase, thereby reducing the B-field amplitude and the interaction strength. We note that the magnet gap actually decreases at first as the photon radius increases. This is because the gap is a fixed multiple of the photon beam size at the wiggler ends, and as L_w/Z_R moves from the optimum value of about 4 to smaller values, the end size decreases to a minimum value when the wiggler is confocal ($L_w = 2Z_R$). Not surprisingly, the curves show roughly that the emittance acceptance can be improved fourfold by doubling the photon beam radius at the expense of a factor of 2 gain loss. This benefit to cost ratio becomes less favorable for further increases in the photon beam radius and magnet gap.

It is of interest to compare the falloff in gain with emittance for various designs. The approximate falloff with increasing emittance is given directly by Equation [20]. Figure 12 compares a set of these rolloff curves for various 5 meter wiggler designs operating at 0.5 μm and 5 percent extraction. These wigglers differ in gap and magnetic field wavelength so as to provide different emittance acceptance values. It is evident in the figure that over the range shown the gain at zero emittance is falling in rough proportion to the square root of the increase in emittance acceptance, assuming the acceptance is defined as the point at which the gain falls by one-half.

IV. Implications

New subharmonic bunching linac injectors recently developed at the Boeing Aerospace Company (BAC)⁽¹²⁾ and at the Stanford Linear Collider (SLC)⁽¹³⁾ have each demonstrated simultaneous achievement of high peak current ($>100\text{A}$) and low normalized emittance ($<0.02\text{ cm-rad}$). These achievements can be compared to the well-known Lawson-Penner relation^(1-3,9)

$$\langle I \rangle [\text{kA}] = \epsilon_N^2 [\text{cm-rad}] , \quad [22]$$

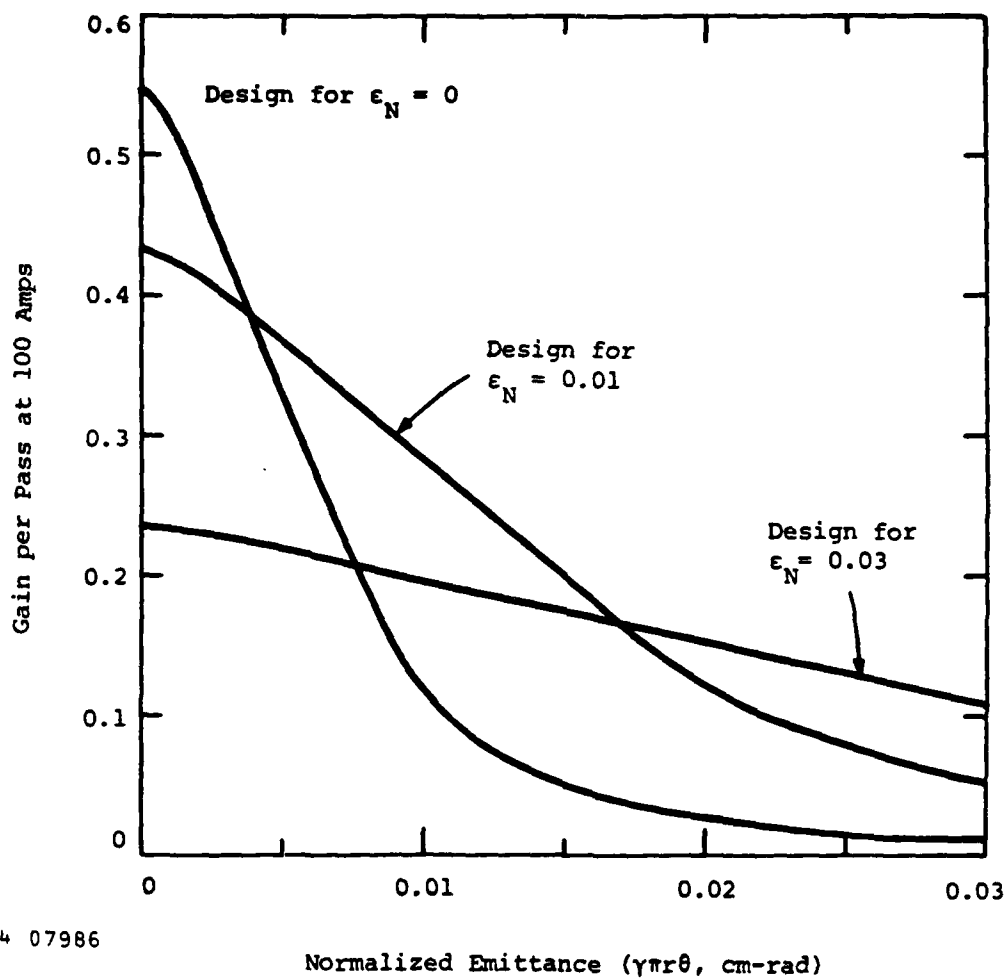
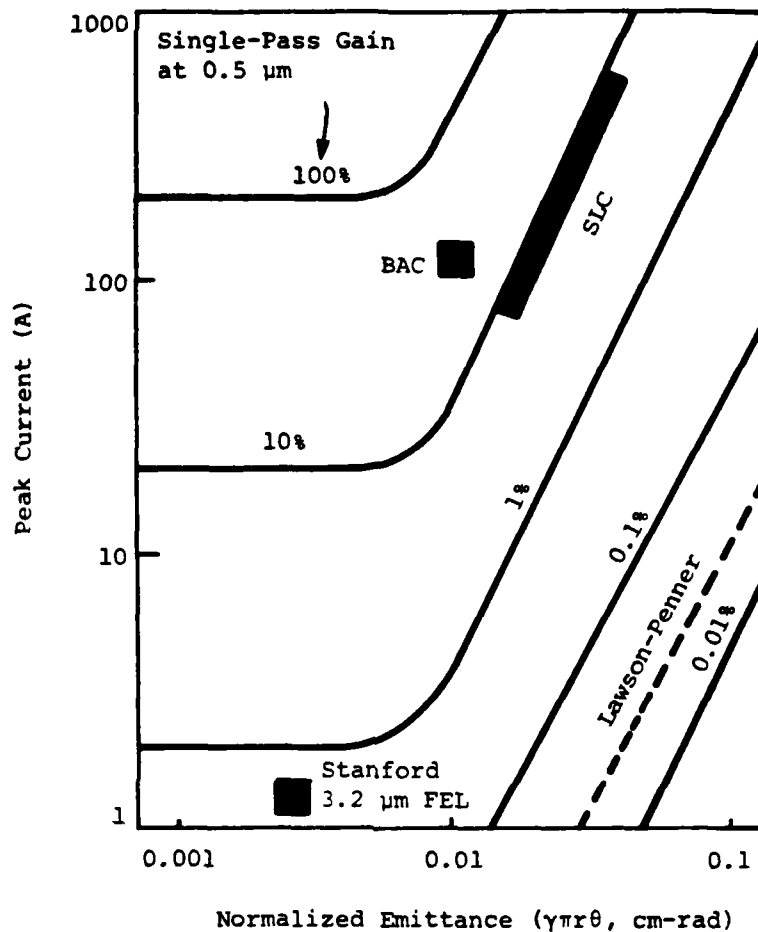


Figure 12. Gain Versus Emittance for Systems Optimized for Various Levels of Emittance. $L_w = 5$ m, $\lambda_s = 0.5$ μ m, 5 percent extraction, $\Delta E = 0$.

which is observed to approximately represent the relationship between the time-averaged current $\langle I \rangle$ and the normalized emittance of a wide range of accelerators working at average currents from milliamperes to kiloamperes. RF accelerators generally produce some degree of bunching while the electrons are of relatively low energy, so the peak and average current values differ. The microscopic duty cycle of the high peak current injectors mentioned previously is made especially small (<0.01) through the use of subharmonic bunching, yielding high peak currents with comparatively low emittance.

The implications of this accelerator technology development on FEL performance is summarized in Figure 13. Here the single-pass gain at 5 percent extraction is plotted as a function of peak current and normalized emittance for the preliminary point design of a visible oscillator given in Table 1. That design was optimized for the BAC accelerator, and as shown in the figure, about 20 percent single-pass gain is possible at 5 percent extraction. Included for comparison are the SLC accelerator and the Stanford superconducting linac,⁽¹⁴⁾ which was used for the first FEL experiment.⁽¹⁵⁾ All three accelerators are characterized by roughly the same current densities in emittance phase space, (I_p/ϵ_n^2) , although the peak currents differ by two orders of magnitude. State-of-the-art high peak current RF linacs appear to satisfy the e-beam requirements for a high extraction oscillator at visible wavelengths.



83 07673

Figure 13. Recent Improvements in Emittance and Peak Current Achieved by Linear Accelerators Improve the Prospects for Visible Oscillation with High Efficiency. Gain values at 0.5 μm assume $L_w = 5$ m and 5 percent extraction.

Acknowledgements

The authors gratefully acknowledge the stimulating interaction with J.L. Adamski and D.R. Shoffstall of the Boeing Aerospace Company with respect to this topic. The work was supported by The Office of Naval Research under contract N00014-82-C-0704 and by the Air Force Office of Scientific Research under contract F49620-81-C-0079.

REFERENCES

1. T.I. Smith and J.M.J. Madey, "Realizable Free-Electron Lasers," Appl. Phys. B, Vol. 27, pp. 195-199, 1982.
2. G. Dattoli, T. Letardi, J.M.J. Madey, and A. Renieri, "Lawson-Penner Limit and Single Passage Free Electron Lasers Performances," submitted for publication in IEEE J. Quantum Electron.
3. J.M.J. Madey, "Application of Transverse Gradient Wigglers in High Efficiency Storage Ring FELs," in the Proceedings of the Bendor Free-Electron Laser Conference, J. de Physique, Vol. 44, pp. C1-169 through C1-178, 1983.
4. J.M. Slater, "Tapered-Wiggler Free-Electron Laser Optimization," IEEE J. Quantum Electron., Vol. QE-17, pp. 1476-1479, 1981.
5. N.M. Kroll, P.L. Morton, and M.N. Rosenbluth, "Variable Parameter Free-Electron Laser," Physics of Quantum Electronics, Vol. 7, pp. 89-112, 1980.
6. K. Halbach, "Permanent Magnet Undulators," in the Proceedings of the Bendor Free-Electron Laser Conference, J. de Physique, Vol. 44, pp. C1-211 through C1-216, 1983.
7. C.A. Brau, "Small-Signal Gain of Free-Electron Lasers with Nonuniform Wigglers," IEEE J. Quantum Electron., Vol. QE-16, pp. 335-339, 1980.
8. J.P. Blewett and R. Chasman, "Orbits and Fields in the Helical Wiggler," J. Appl. Phys., Vol. 48, pp. 2692-2698, 1977.
9. V.K. Neil, "Emittance and Transport of Electrons in a Free Electron Laser," SRI Report JSR-79-10 (December 1979).

10. D. Quimby and J. Slater, "Emittance Acceptance in Tapered-Wiggler Free-Electron Lasers," in the Proceedings of the Fourth Workshop on Free-Electron Laser Devices, Eastsound, Washington, June 27 - July 1, 1983, to be published by the Society of Photo-Optical Instrumentation Engineers.
11. A.E. Siegman, An Introduction to Lasers and Masers, McGraw-Hill, New York, 1971.
12. J.L. Adamski, W.J. Gallagher, R.C. Kennedy, D.R. Shoffstall, E.L. Tyson, and A.D. Yeremian, "Accelerator Technology for a High Power Short Wavelength FEL," in the Proceedings of the Fourth Workshop on Free-Electron Laser Devices, Eastsound, Washington, June 27 - July 1, 1983, to be published by the Society of Photo-Optical Instrumentation Engineers.
13. M.B. James, J.E. Clendenin, S.D. Ecklund, R.H. Miller, J.C. Sheppard, C.K. Sinclair, and J. Sodja, "Update on the High Current Injector for the Stanford Linear Collider," SLAC-PUB-3085, presented at the Particle Accelerator Conference, March 21-23, 1983, Santa Fe, New Mexico.
14. T.I. Smith, "The Stanford Superconducting Linear Accelerator," Physics of Quantum Electronics, Vol. 8, pp. 77-87, 1982.
15. D.A.G. Deacon, L.R. Elias, J.M.J. Madey, G.J. Ramian, H.A. Schwettman, and T.I. Smith, "First Operation of a Free-Electron Laser," Phys. Rev. Lett., Vol. 38, pp. 892-894, 1977.

APPENDIX C

Mode Structure of a Tapered-Wiggler Free-Electron Laser Stable Oscillator

I. INTRODUCTION

The tapered-wiggler free-electron laser (FEL) is of current interest for its potential as an efficient, tunable laser. The basic idea is a variation of the FEL concept demonstrated in the experiment of Deacon, et al.[1], in which it was shown that a small fraction of electron-beam kinetic energy could be converted to optical energy in a single pass through a wiggler magnet. The tapered-wiggler concept[2] involves variation, or tapering, of the wiggler parameters as a function of axial position in such a manner as to maintain a resonant interaction as the electrons decelerate. This tapering allows increased kinetic energy extraction per pass, and may lead to high efficiency systems through reduction of e-beam recirculation or energy recovery requirements.

Several verification experiments of the basic concept are in progress[3]. Initial experiments are expected to achieve only low photon gain, and in a sense provide validation only of the relatively simple theory describing electron deceleration in predetermined photon and wiggler fields. The process of self-consistently determining electron and photon behavior in high gain amplifiers or oscillators is significantly more complex, and has recently been the subject of considerable analysis. With respect to the photon beam parameters, such analysis has generally fallen along one of two lines, study of either the axial profile of the beam when short pulses are of interest[4], and study of the transverse structure[5,6]. The theoretical analysis presented here pertains to the transverse optical field structure of tapered-wiggler oscillators.

Interest in the oscillator transverse field structure stems largely from the nonlinear interaction of the gain media and optical field. Geometries optimized for maximum electron-photon interaction will

generally involve a long, small diameter e-beam centered in a larger photon beam. The resulting amplitude and phase modification of the photon beam, being radially nonuniform, leads to generation of optical cavity modes which should be accounted for in system design, and also leads to an output beam of lower quality than the ideal diffraction limit. It is the quantification of these effects that is pursued here.

The method of calculation is described in Sec. II. Phase and amplitude profiles of the photon field are determined in a plane perpendicular to the cavity axis, this plane being numerically propagated back and forth along the axis using a paraxial wave equation. Section III describes the application of this formalism to the FEL interaction and relevant geometries. The complexity of the FEL interaction is reduced by means of a resonant-phase approximation, thus providing a simple relationship between the phase of the stimulating and stimulated electric fields. While the calculations presented have relatively simple modal structure, the analysis is directly applicable to more complicated structure. The resonant-phase approximation does limit the applicability of the model to fully saturated photon intensity levels. The optical cavity is taken to be injected from an external source at the full saturated intensity, and the subsequent development of mode structure is the subject of primary interest. Actual tapered-wiggler FEL oscillators may be self started from spontaneous emission or require injection at or below saturation intensity. Our analysis method precludes modeling transverse mode structure effects in the small-signal start-up regime, but it provides a useful way to determine the steady mode structure in the saturated, trapped-particle regime of tapered-wiggler FEL oscillators. While the details of the mode structure during the approach to steady state will be dependent on the start-up method, the steady-state structure should be insensitive to the start-up method. The properties of the transverse field are analyzed by means of decomposition into Gaussian-Laguerre modes, providing a convenient measure of beam properties in terms of partition of the total power into modes. The mode structure

depends strongly on the degree of aperturing in the optical cavity, this resulting from finite size optical elements. Aperturing by the wiggler magnets will be particularly important in geometries optimized for FEL interaction strength[7]. Presence of the wiggler has been accounted for by truncation of the beam at positions of the beam corresponding to the wiggler entrance and exit locations. Results of the study are presented in Sec. IV and summarized in Sec. V.

II. CALCULATIONAL METHODS

The free-electron laser oscillator is modeled using an axisymmetric physical optics code. Within the wiggler, the wave front is propagated numerically using a finite-difference solution of the paraxial wave equation [8]. For propagation between the wiggler and distant mirrors, the Huygens-Fresnel integral [9] is used. The computer model is used to find the transverse mode structure and far-field characteristics, accounting for diffraction, nonuniform gain media, refraction, and arbitrary mirror configurations and reflectivities.

A linearly polarized wave amplitude may be expressed as a scalar function of position and time

$$u(x,y,z,t) = U(x,y,z)\cos(\omega t + \Phi(x,y,z)), \quad [1]$$

where U , ω , and Φ are the amplitude, angular frequency, and phase of the wave, respectively. Using phasor notation, the explicit time dependence may be removed

$$\hat{U} = U(x,y,z)\exp(-i\Phi(x,y,z)), \quad [2]$$

where we use the superscript $\hat{}$ to denote a complex number, or phasor. The original time-dependent amplitude may be recovered by the transformation

$$u(x,y,z,t) = \text{Re}[\hat{U}(x,y,z)\exp(-i\omega t)]. \quad [3]$$

The complex wave amplitude propagates through free space according to the time-independent wave equation

$$\nabla^2 \hat{U} + k^2 \hat{U} = 0, \quad [4]$$

where $k = 2\pi/\lambda$ is the laser wave number. For light traveling nearly parallel to the z -axis, one can remove most of the rapid phase variation by defining a new function $\hat{\psi}$ by

$$\hat{U}(x, y, z) = \hat{\psi}(x, y, z) \exp(-ikz). \quad [5]$$

The function $\hat{\psi}$ represents the difference between the actual wave front and a uniform plane wave, and thus is a much slower varying function of position. This function satisfies

$$\nabla^2 \hat{\psi} - 2ik \frac{\partial \hat{\psi}}{\partial z} = 0. \quad [6]$$

the so-called "paraxial wave equation". We solve this equation numerically in axisymmetric cylindrical geometry under the assumption that $\hat{\psi}$ varies so slowly with z that its second derivative, $\partial^2 \hat{\psi} / \partial z^2$, may be neglected,

$$\frac{1}{r} \frac{\partial}{\partial r} \left[r \frac{\partial \hat{\psi}}{\partial r} \right] - 2ik \frac{\partial \hat{\psi}}{\partial z} = 0. \quad [7]$$

This free-space propagation equation is solved implicitly using a centered-difference technique involving inversion of a tridiagonal matrix[10]. This method is stable independent of step size, thus allowing the step size Δz to be chosen on the basis of desired accuracy, rather than on stability considerations. The technique is second-order accurate and is found to achieve excellent energy conservation.

A disadvantage of the finite-difference propagation technique is the inability to accurately treat sharp aperture edges. At an aperture, the complex amplitude is discontinuous, so that high order radial derivatives are undefined. Truncation errors due to these terms cannot be made arbitrarily small by decreasing Δr . This difficulty is overcome by using

smoothly tapered aperture edges[8], allowing accurate numerical calculation of the diffraction pattern. The distinction between smooth and hard apertures is unimportant to this application because differences in the fields are found only at locations very close to the aperture[11]. The apertures are smoothed by using a Gaussian profile at the edge. For example, the mirror reflectivity is

$$R(r) = \begin{cases} R_0 & r < r_0 \\ R_0 \exp\left[-(r-r_0)^2/\tau^2\right] & r > r_0 \end{cases} \quad [8]$$

where r_0 is the radius of the portion of the mirror with uniform reflectivity, R_0 , and τ is the truncation distance. We choose r_0 and τ so that the actual diameter, $2a_m$, of the mirror being modeled lies at the half power points of the Gaussian edges.

In regions of the problem where the FEL gain medium is active, the propagation equation contains an additional term describing the FEL interaction

$$\frac{1}{r} \frac{\partial}{\partial r} \left[r \frac{\partial \hat{\psi}}{\partial r} \right] - 2ik \left[\frac{\partial \hat{\psi}}{\partial z} - Af(r) \frac{\hat{\psi}}{|\hat{\psi}|} e^{-i(\pi/2 - \theta)} \right] = 0. \quad [9]$$

Here parameters A and $\theta(r, z)$ describe the E-field generated by the gain medium. The parameter A is the amplitude of the E-field generated on-axis, per unit distance along the wiggler (i.e., an interaction of length dz generates a field of amplitude $A dz$). A is proportional to the density of trapped electrons. Since the number of electrons in the bucket is fixed, A is independent of axial position. The variation in gain along the wiggler length is due to the variation of the phase θ of the stimulated field (the field of amplitude $A dz$) with respect to the stimulating field, $\hat{\psi}$. Phases of $+90$ and -90 degrees correspond to gain and absorption, respectively, with no phase shift. Phases of 0 and 180 degrees correspond to phase-front lag and advance, respectively, with no gain. The dimensionless $f(r)$ is a spatial form factor describing the radial electron density profile.

Several checks confirm the accuracy of the finite-difference propagation algorithm. Control calculations have been made using different grid sizes. These calculations verify that the results are independent of grid size, for the grid resolution used in this study. Furthermore, the beam power is conserved to within 0.05 percent when a combination of TEM_{00} and TEM_{10} modes is propagated for 35 round trips around an unapertured confocal resonator.

A plane-polarized optical beam is circulated in a symmetric stable resonator. The wiggler length is equal to two Rayleigh ranges of the optical beam. This geometry produces a shallow waist at the wiggler center, and nearly optimizes the electron-photon energy exchange. The majority of calculations presented in this paper pertain to confocal cavities, in which case the mirrors are located precisely at the ends of the wiggler. In practice, the mirrors may be separated by more than the wiggler length to provide e-beam access, but the basic aspects of the problem remain the same. The cavity mirrors have a radius of a_m . The presence of the wiggler magnets is accounted for by including additional apertures of radius a_w at each end of the wiggler. For the following analysis, the mirror on the right is taken to be a partially reflective output coupler, with radially independent reflectivity. The output coupling is chosen to be approximately equal to the FEL gain at saturation. Low to moderate gain, less than 50 percent per pass, is considered in all cases. The electron beam is assumed to have a Gaussian radial electron density profile

$$f(r) = \exp\left[-r^2/r_{eb}^2\right], \quad [10]$$

independent of axial position. In all calculations presented, the e-beam is assumed to be fairly small in diameter compared to the photon beam.

Calculation of the interaction with the gain medium is based on the synchronous-particle approximation. That is, all interacting electrons are assumed to be trapped in the ponderomotive potential well, and it is further assumed that all such electrons are located in the well at the stable-phase point[2]. This in turn determines the relative phase between the locally generated field and locally applied field, with the result that θ in Eq. [9] can now be replaced with the stable-phase angle. This approximation is useful since trapped electrons oscillate about the synchronous-phase point, but its use precludes modeling effects associated with the pendulum motion of trapped particles.

The stable-phase angle, θ , is a function of the local electric field and local wiggler taper $d\gamma_r/dz$, where γ_r is the resonant energy. The wiggler taper must be specified as an input parameter. For this analysis, the taper is chosen so that, in the presence of a TEM_{00} photon beam, the phase would be independent of axial position. In the presence of the FEL interaction, however, the wave front is typically not pure TEM_{00} . The phase angle is therefore not constant, but is specified in terms of the local field $\hat{U}(r,z)$ by

$$\sin\theta(r,z) = \sin\theta_0 \frac{|U_{0,0}(0,z)|}{|U(r,z)|} = \frac{\sin\theta_0}{|U(r,z)|} \frac{1}{\sqrt{1 + (z/Z_R)^2}}, \quad [11]$$

where $Z_R = \pi w_0^2/\lambda$, w_0 is the 1/e E-field radius of the TEM_{00} beam at the waist, $|U_{0,0}(0,z)|$ represents the on-axis amplitude of a TEM_{00} beam normalized for unity amplitude at the waist, and θ_0 is the stable-phase angle which would be produced on axis in the presence of a TEM_{00} beam of this normalization. The initial pump beam is a TEM_{00} wave with unity normalization. As the modal structure evolves due to the FEL interaction, the resonant phase evolves self-consistently according to Eq. [11]. Relatively high E-field values cause the electrons to slide toward the bottom of the bucket (toward small phase angles with high refraction and low gain) while relatively small E-fields cause large phase angles and high gain. This effect tends to produce an equilibrium value of intracavity flux.

In principle, the phase angle varies radially within the e-beam. Such variation has been included, but is unimportant for the cases examined since the photon intensity is nearly constant across the e-beam. If the phase angle reaches 90 degrees, electron detrapping, or escape from the ponderomotive potential well and subsequent loss of energy exchange, will occur. We have allowed electron detrapping to occur as a result of radial variation in the photon intensity distribution, but this is also unimportant for these cases. The code treats detrapping by assuming straight-line electron trajectories parallel to the wiggler axis. This

neglects the sinusoidal betatron orbits [12] which result from transverse gradients in the magnetic field. The code is nevertheless applicable to cases which have significant betatron motion, provided that there is little radial variation of photon intensity and phase across the e-beam.

Detrapping may also occur across the entire e-beam as a result of mode beating. For example, it is shown later that interference between the 1-0 and 0-0 modes can lead to axial intensity fluctuations of roughly a factor of two. If a design phase angle of $\theta_0 = 45$ degrees had been chosen, Eq. [11] shows that detrapping would occur on axis when the competition of the two modes is included. Since $\theta(r,z)$ is calculated based on the local field, any detrapping caused by mode beating is self-consistently taken into account. The detrapping problem can be avoided by choosing a smaller design value of the phase angle, but at the expense of electron deceleration.

The oscillator mode structure may be characterized by decomposing the wave front into the axisymmetric Gaussian-Laguerre modes of the resonator. The normalized, orthogonal modes may be written[9]

$$\hat{U}_{p,0}(r,z) = \sqrt{\frac{2}{\pi}} \frac{1}{w(z)} \exp\left[-\left[\frac{r}{w(z)}\right]^2\right] L_p\left[2\left[\frac{r}{w(z)}\right]^2\right] \cdot \exp\left[-i\left\{kz - (2p+1)\tan^{-1}\left[\frac{z}{Z_R}\right] + \frac{z}{Z_R}\left[\frac{r}{w(z)}\right]^2\right\}\right] \quad [12]$$

where $w(z) = w_0\sqrt{1 + (z/Z_R)^2}$, $p = 0,1,2,\dots$ is an integer index for each mode, the L_p are the associated Laguerre polynomials of order p , and $Z_R = \pi w_0^2/\lambda$ is set by the mirror curvature. The modes $\hat{U}_{0,0}$, $\hat{U}_{1,0}$, $\hat{U}_{2,0}, \dots$ correspond to circular TEM₀₀, TEM₁₀, TEM₂₀, ... modes, respectively. As the modes propagate through one round trip of the cavity, they incur a phase shift relative to a plane wave of $4(2p+1)\tan^{-1}(L/2Z_R)$ due to curvature.

We can describe any arbitrary wave front as an expansion of modes

$$\hat{U}(r,z) = \sum_{p=0}^{\infty} \hat{a}_p \hat{U}_{p,0}(r,z) . \quad [13]$$

The complex coefficients are conveniently found by evaluating

$$\hat{a}_p = \int_0^{\infty} \hat{U}(r,z) \hat{U}_{p,0}^*(r,z) 2\pi r dr , \quad [14]$$

where the superscript "*" denotes a complex conjugate. On each pass through the laser the wave-front mode structure is analyzed at the output mirror, immediately following the mirror truncation. This decomposition describes both the internally reflected and the outcoupled field. The far-field distribution may be found by passing the output beam through a collimating lens, then focusing with a spherical mirror. A Huygens-Fresnel integral[9] is used for propagation to the focal spot, yielding the far-field pattern.

Most of the simulations presented here pertain to confocal cavities, that is the Rayleigh range Z_R is equal to half the cavity length, L_C . Confocal systems, as well as concentric ($L_C/Z_R = \infty$) and planar ($L_C/Z_R = 0$), can support unusual mode structure because the relative phase slippage between cavity modes over one round trip is an integral multiple of 2π . For empty cavities, relative phases of individual modes at any given transverse plane will repeat on each round trip. Consequently, the mode mixing due to truncation by any apertures present has interesting properties. For example, the gain-free confocal system injected with pure 0-0 mode develops almost no 1-0 mode by way of mirror truncation, but the amount of 2-0 mode can be appreciable. The 1-0 mode is produced by truncation of the 0-0 mode at each mirror, but the 1-0 fields generated at the two mirrors drive 1-0 modes which are 180 degrees out of phase. The 2-0 mode fields produced at each mirror are in phase. If 1-0 mode is produced by the gain media, another interesting effect occurs. In

propagating from one end of the cavity to the other, the phase of the 0-0 mode changes by $\pi/2$ (relative to a plane wave), while that of the 1-0 mode slips by $3\pi/2$. The interference is therefore different at each end of the cavity, providing an asymmetry in the axial direction. Such an asymmetry can be supported in the FEL since the gain mechanism is active in one direction only.

These effects are less apparent in cavities intermediate to the special cases of confocal, concentric, or planar. The importance of any deleterious effects might therefore be considered minimal, but the reverse may actually be true. The low Fresnel number and small wiggler bores inherent to FELs tend to result in unusually high energy loading on mirror surfaces. For high average power systems, alleviation of these problems may require the use of very long, near-concentric cavities.

IV. RESULTS

4.1 Properties of a Confocal FEL Resonator

The mode structure of the confocal FEL oscillator described in Table I has been investigated in detail. We will first point out some of the basic features of the mode structure of a confocal FEL oscillator, followed by an investigation of the effect of varying some of the parameters.

The conditions listed in Table I describe a confocal stable resonator with apertures of radius $1.8 w$, where w is the $1/e$ radius of the E-field of a TEM_{00} mode at the ends of the wiggler.

TABLE I

Standard Conditions for FEL Oscillator
Mode Structure Investigation

Cavity Length, L_c/Z_R	2 (confocal)
Aperture Size, a_w/w	1.8
E-Beam Size, Z_R/Z_R^{eb}	10
Design Phase Angle, θ_0	20.7°
Gain	10%/pass
Output Coupling	9.1%
Aperture Truncation Length, T/a_w	0.055

This mirror size provides a modest degree of mode selection. Higher order modes are attenuated since they carry more energy at larger radii. The electron beam size is specified by $Z_R/Z_R^{eb} = 10$, where we define $Z_R^{eb} = \pi r_{eb}^2/\lambda$ to be the Rayleigh range based on the 1/e radius of the Gaussian e-beam. We choose the electron beam size to be significantly smaller than the pump beam ($r_{eb}/w_0 = 0.316$), so the e-beam is essentially pumped by a uniform intensity wave front. The peak (on-axis) electron density is chosen to give a gain approximately equal to the 9.1 percent output coupling (reflectivity of 0.909). Small additional cavity loss results from clipping at the apertures.

The distribution of Gaussian-Laguerre modes at the output coupler are shown as a function of round-trip number in Fig. 2. The wave front is initiated as a TEM_{00} mode, but settles down within 30 passes to a steady mode distribution containing a significant contribution of 1-0 mode. All higher modes are strongly suppressed by the finite aperture radii. The high content of 1-0 mode is due to the FEL interaction, rather than by truncation at the apertures. The fraction of 1-0 mode power in the absence of gain is only 2.6×10^{-6} . The higher order mode with the highest energy content in the bare resonator is the 2-0 mode; it constitutes only 0.27 percent of the total power.

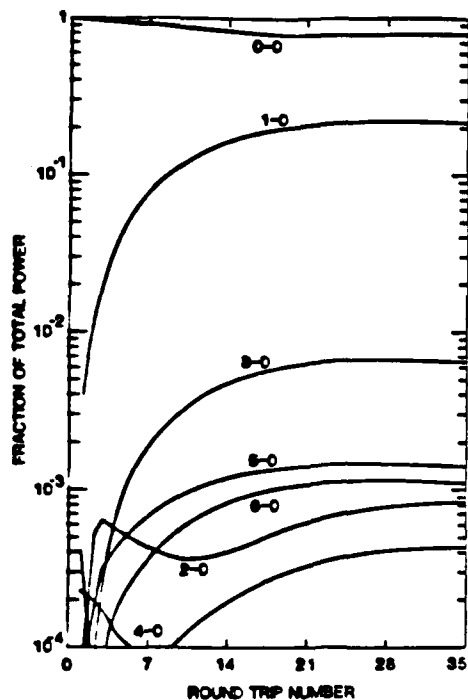


Figure 2. Mode structure evolution for conditions of Table I.

The electron trapping fraction and beam power are shown as a function of round-trip number in Fig. 3.

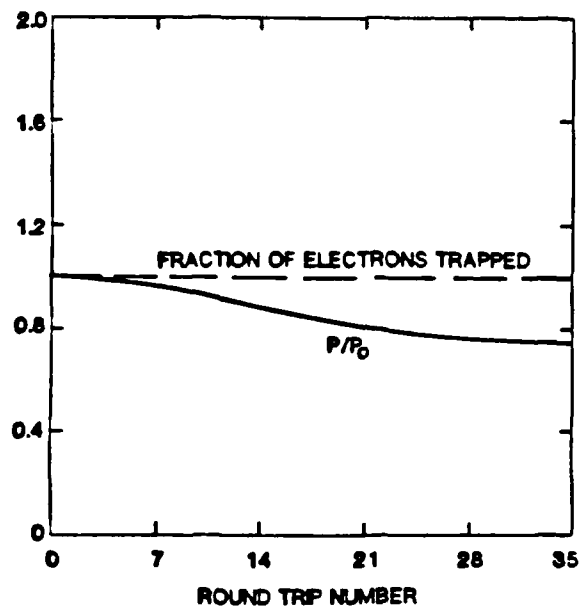


Figure 3. Beam power and fraction of electrons trapped as a function of round-trip number for conditions of Table I.

As the mode structure evolves, the round-trip losses exceed the gain slightly on each pass, allowing the power level to decay about 25 percent. Once a steady mode structure has developed, the power level comes to steady state as the phase angle adjusts to allow the gain to match the round-trip losses. The electron beam is trapped essentially over its full radius.

The steady-state phase angle of the FEL interaction is shown as a function of axial and radial position in Fig. 4.

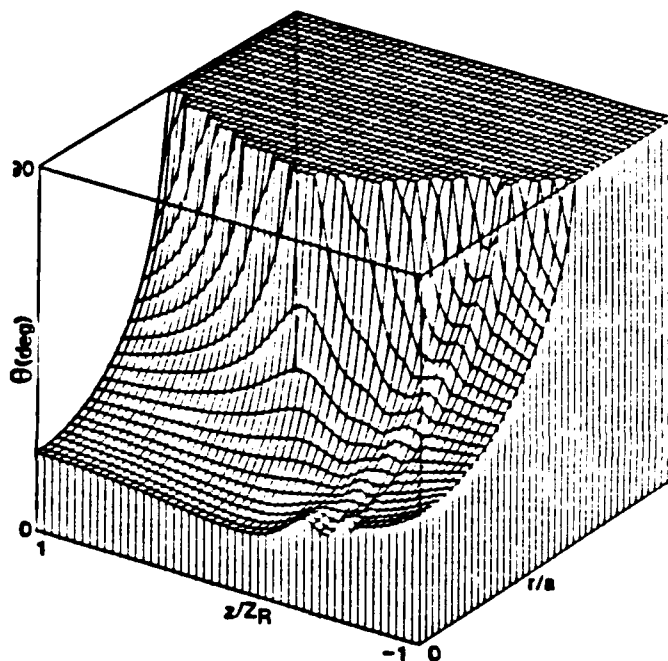


Figure 4. Steady-state phase angle for FEL interaction as a function of position. Conditions given in Table I.

While the on-axis phase angle is initially 20.7 degrees for the 0-0 mode pump beam, the steady mode distribution results in on-axis phase angles which vary between 15 and 32 degrees. The largest on-axis phase angle, or lowest intensity, occurs at the back mirror. The radial phase angle profiles have a rather broad, flat distribution, with a sharp transition to large angles and detrapping at large radius. The broad distribution is consistent with the e-beam being pumped by an essentially uniform intensity wave front. The narrowest profile occurs at the midplane between the mirrors (at the photon beam waist) where detrapping occurs at $r = 2.4 r_{eb}$. Downstream from this point, all electrons at this radius or

greater are detrapped, but this constitutes only about 0.3 percent of the total e-beam.

The steady intracavity intensity distribution is illustrated in Fig. 5.

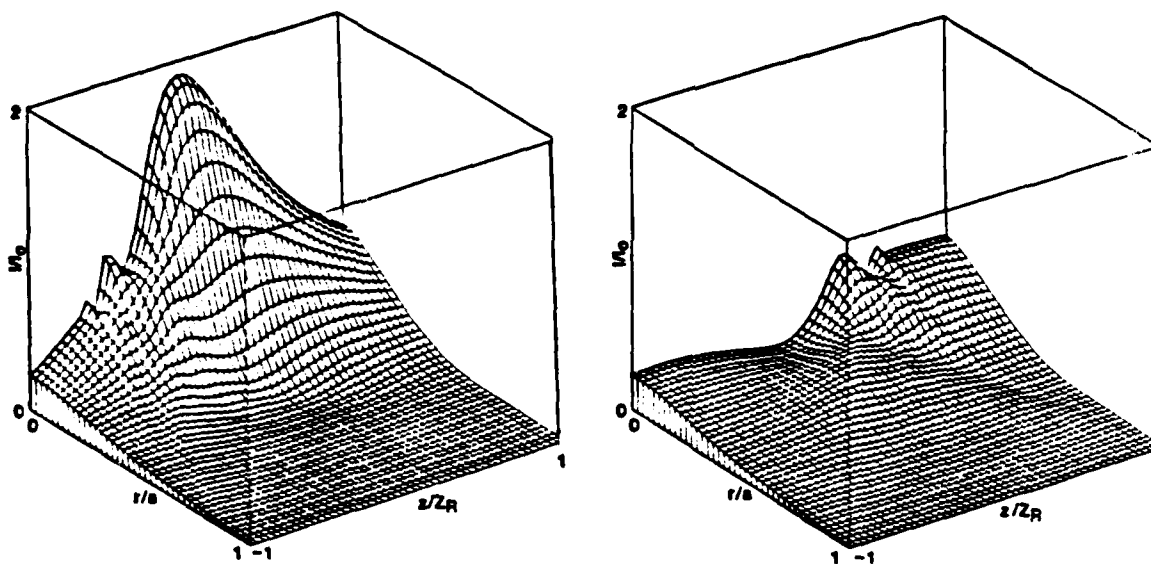


Figure 5. Intracavity intensity distributions of steady mode structure on (a) forward pass, and (b) return pass for conditions of Table I.

The intensity distribution $I(r, z)$ for the forward pass is shown in Fig. 5(a) and the backward pass in 5(b). The intensity is normalized in such a way that the on-axis intensity for the injected 0-0 mode is 1 at the midplane ($z/Z_R = 0$) and 0.5 at the mirrors ($z/Z_R = \pm 1$). The sharp variation of intensity near the axis just after a mirror reflection is due to the diffraction pattern of the aperture. The steady distribution develops in such a way that the central on-axis intensity is higher than that of the individual 0-0 mode pump beam on forward passes and lower on backward passes. The forward and backward going on-axis intensities are compared with the 0-0 mode in Fig. 6.

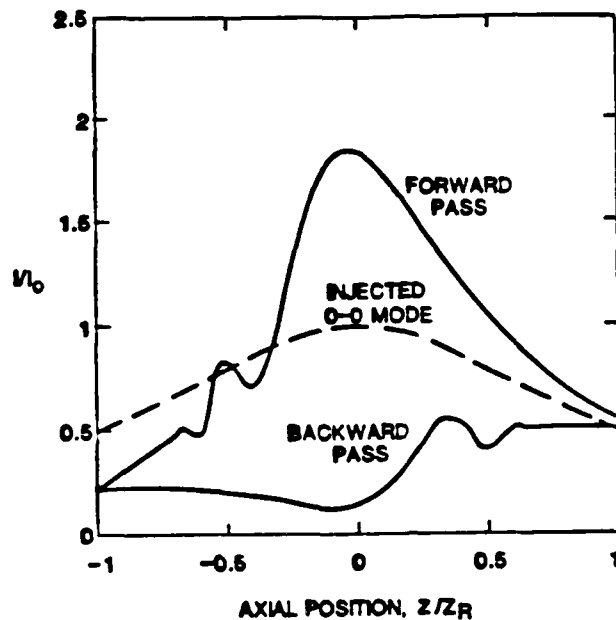


Figure 6. Comparison of on-axis intensity distributions of steady mode structure and injected 0-0 mode.

The on-axis intensity on the output mirror is over two times that of the back mirror. This difference cannot be accounted for by gain, which is only 10 percent, but results from interference between the dominant 0-0 and 1-0 modes. The relative phases of the two modes are such that they constructively interfere on-axis on forward passes and at the output mirror while destructively interfering on backward passes and at the back mirror.

The radial structure of the output beam is shown by the intensity and phase profiles in Fig. 7.

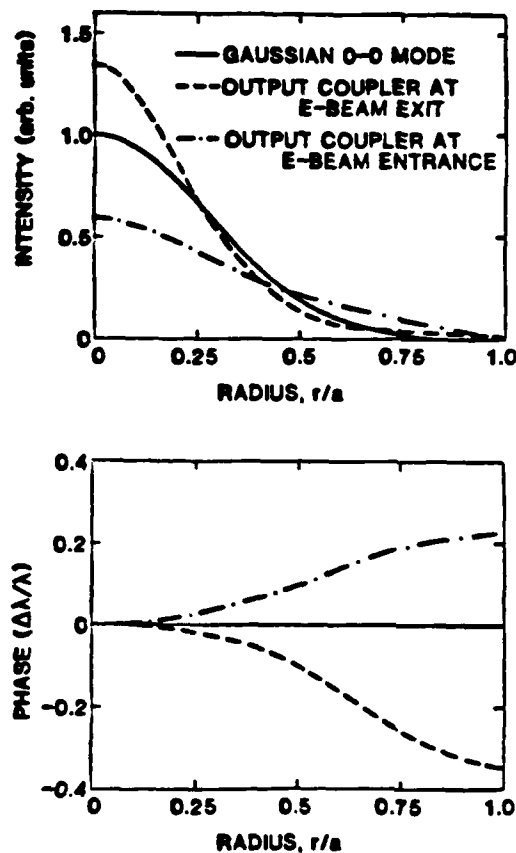


Figure 7. Intensity and phase profiles at output coupler for conditions of Table I. Phase profile has spherical curvature of output mirror removed. Intensity profiles are normalized for equal power.

The conditions are those of Table I, except that data is included for outcoupling at either end of the cavity. The axial structure and Gaussian-Laguerre mode content of the two cases is essentially identical; the differences in the intensity and phase profiles may be attributed to different relative phases between the 0-0 and 1-0 modes. When the spherical curvature of the output mirror is removed from the phase distributions of the two nearly Gaussian output beams, each beam contains some additional residual spherical curvature. Evidently the beam at the

e-beam exit has somewhat more spherical curvature than the output mirror and the beam at the e-beam entrance has somewhat less curvature.

A useful measure of the focusability of the beams is made by examining their amplitude-weighted rms phase deviations at the output mirror. When all spherical curvature is removed from the phase profiles, the residual phase aberrations shown in Fig. 8 are found.

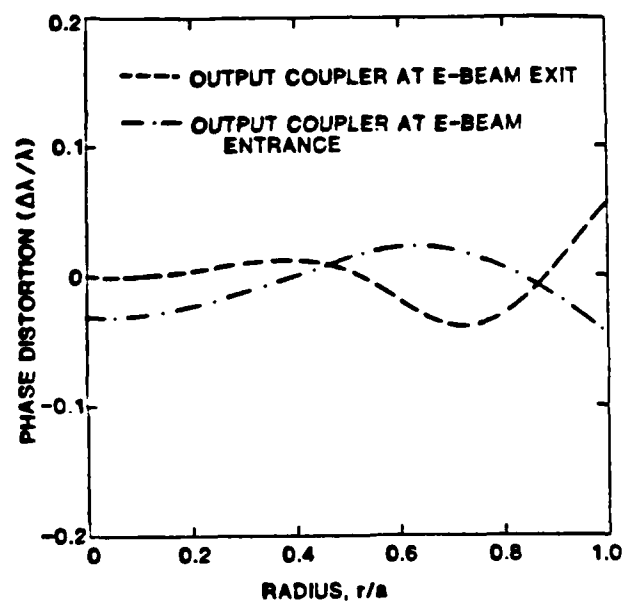


Figure 8. Residual wave-front distortion at output mirror with all spherical curvature removed.

All phase differences across the aperture are less than 1/10 of a wavelength. Since the aberrations are predictable rather than random, they could be corrected by use of properly designed optical components. Such an effort is probably unnecessary, however, since the aberrations are so small. The amplitude-weighted rms wave-front distortion[13] is approximately 1/50 of a wavelength at both the e-beam exit and entrance. This phase deviation results in a far-field peak intensity loss of less than 2 percent. Equivalently, the Strehl ratio is greater than 98 percent.

An additional demonstration of output beam quality is the calculation of power delivered to a far-field target. Conceptually, such a test is made using the laser together with a focusing lens. An appropriate figure of merit is the power which can be delivered within a specified target area using a lens of specified aperture size. A nearly equivalent mathematical figure of merit involves the fraction η of total power P_{TOT} which can be delivered within a radius R_t on the target

$$\eta = \frac{1}{P_{TOT}} \left(\frac{f}{\alpha} \right)^2 \int_0^{R_t} I(r) 2\pi r dr. \quad [15]$$

Here f is the distance from focusing lens to target, and α is the mean radius of the beam as it exits the focusing optics.

$$\alpha = \frac{1}{P_{TOT}} \int_0^{\infty} r I(r) 2\pi r dr. \quad [16]$$

Results are shown in Fig. 9 as a function of the target radius. The target radius has been normalized to α/f .

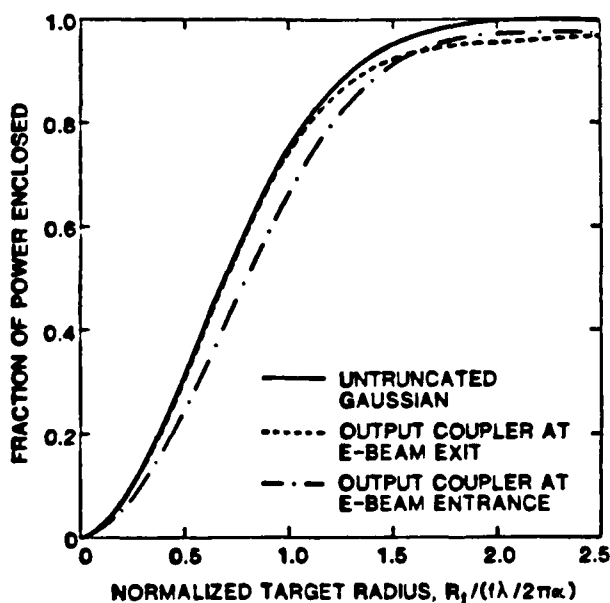


Figure 9. Fraction of power enclosed at focal plane as a function of normalized radius.

Results for a diffraction-limited TEM_{00} beam are included for comparison. The difference in power delivered to the target for these two output beams is very small. The high focusability of each beam is evident.

Such a conclusion may appear to contradict the mode decomposition of Fig. 2, which shows about 20 percent of the energy to be in the 1-0 mode. The apparent discrepancy lies in the fact that Fig. 2 is a decomposition based on the basis set determined by the mirror geometry. The choice of different basis sets, i.e., a change of Rayleigh range and waist location, will result in different energy partitions. We have made an empirical search of Rayleigh range and waist location parameters for the purpose of finding the highest projection into the 0-0 mode. The result, for the case of outcoupling at the e-beam exit, is that 96.7 percent of the total energy can be projected into the 0-0 mode using the best matched Rayleigh range and waist location. Physically, this means that the intracavity beam is of nearly diffraction-limited quality, but its curvature is not matched to that of the fundamental cavity mode. The mismatched wave front does not reflect back on itself, resulting in the front-to-back asymmetry.

4.2 Parametric Variation

We have seen that for a nominal phase angle, θ_0 , of 20.7 degrees, approximately 22 percent of the total energy of the stable transverse mode lies in the 1-0 cavity mode. The phase angle is a design parameter, depending primarily on the wiggler taper, cavity Q, and e-beam current. Analysis of the mode structure variation as a function of θ_0 is of interest, since a range of design values will be achievable in practice. This has been investigated with two simulations in which phase angles of 90 degrees and 0 degrees were used. These two limiting cases correspond to pure gain and pure refraction, respectively. In both cases, the phase angle was fixed everywhere in r and z so that there is no possibility of electron detrapping. All other parameters are those of Table I. The results are shown in Fig. 10.

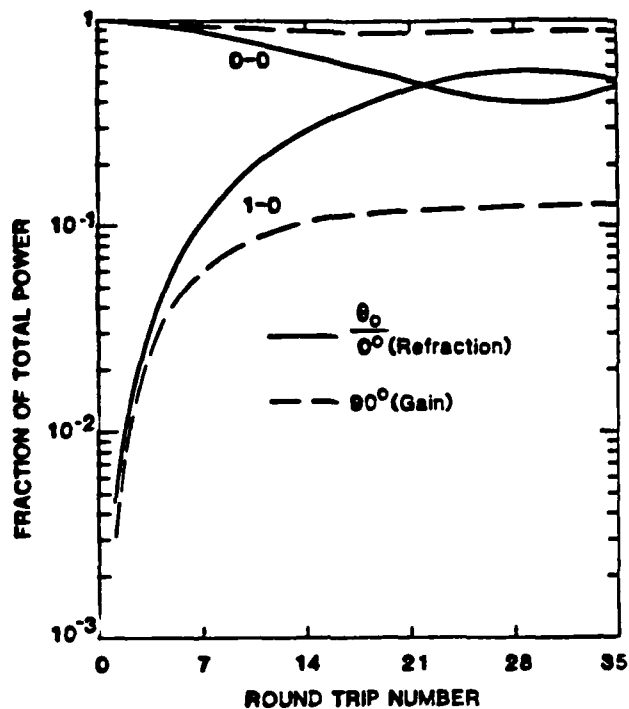


Figure 10. Mode structure evolution for various FEL interaction phase angles with fixed trapped electron density. Phase angle is everywhere uniform with no electron detrapping. $Z_R/Z_R^b = 10$, $a_w/w = 1.80$, $L_C/Z_R = 2$.

When compared to the earlier results, the pure refraction case develops a large fraction of higher order modes. In fact, the round-trip diffraction losses, i.e., power falling outside the mirror radius, approach 10 percent. Evidently, refraction is a much stronger mechanism for beam spreading than gain. While large phase angles appear to be desirable for minimizing the higher mode content, there are fundamental limitations on how large a design phase angle can be used. For example, as discussed in Sec. III, larger design phase angles are more susceptible to detrapping due to mode beating.

This variation in phase angle was made with a fixed trapped electron density. It could be achieved in practice by variation of the cavity Q , thereby changing the cavity flux level and rotating the locally generated electron E-field phasor with respect to the applied E-field phasor. A related variation is the change in length of the electron E-field phasor with the angle fixed.

Results are shown in Fig. 11.

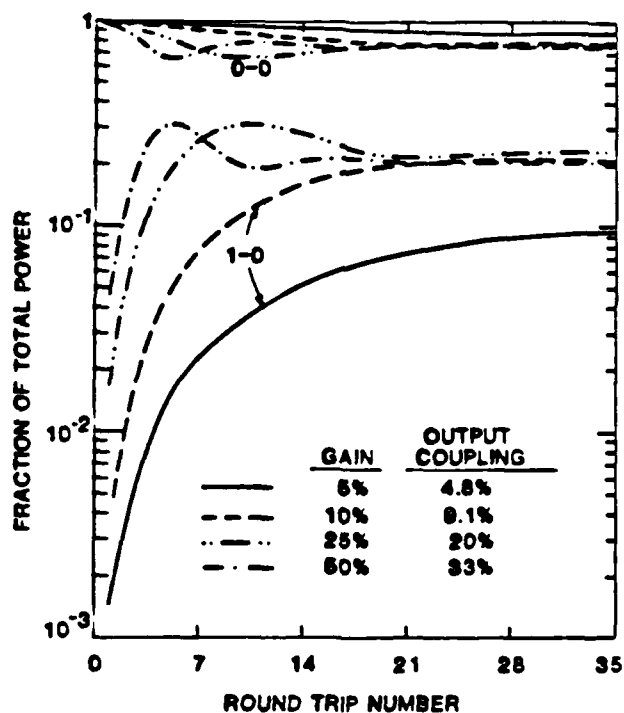


Figure 11. Mode structure for various output couplings with fixed phase angle. $\theta_0 = 20.7^\circ$, $Z_R/Z_R^{eb} = 10$, $a_w/w = 1.80$, $L_c/Z_R = 2$.

In this case, use of low output coupling results in a general reduction in higher order mode content, since both gain and refraction are reduced. As the gain is increased above 10 percent, the content of 1-0 mode appears to reach a plateau. Apparently, there is a mechanism for either increasing the losses of 1-0 mode or decreasing its production, causing the 1-0 mode content to saturate at a level independent of the length of the electron E-field phasor.

The effect of changing the electron-beam size with fixed gain is shown in Fig. 12.

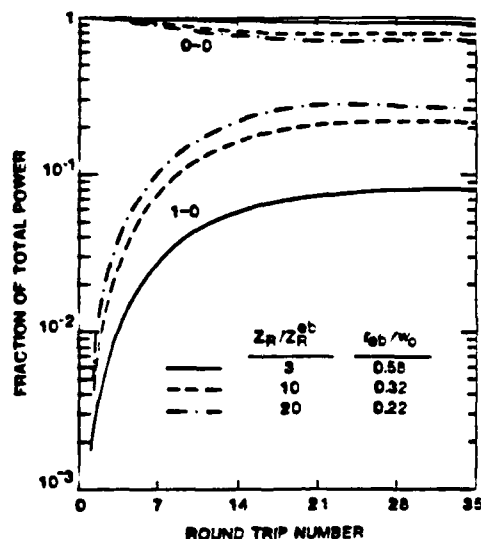


Figure 12. Mode structure for various e-beam sizes with fixed gain. Gain = 10 percent, 9 percent output coupling, $\theta_0 = 20.7^\circ$. $a_w/w = 1.80$, $L_c/Z_R = 2$.

As the e-beam diameter is varied, the trapped electron density is changed so as to keep the gain constant. The e-beam size is not increased to the point that detrapping of the wings of the e-beam density distribution becomes significant. Increasing the size of the e-beam decreases the content of higher modes. This is consistent with the notion that a small diameter gain media leads to high diffraction angles and hence high order modes. However, in this case, the e-beam constitutes an antenna of sufficient length that the angular spread of its emission is nearly length

dominated and independent of transverse size. Accordingly, we expect that reduction of the e-beam size to zero will not produce mode structure dramatically different from that of the $Z_R/Z_R^{eb} = 20$ curve of the figure.

The steady-state mode structure is also a function of the aperture size. As shown in Fig. 13, the use of small apertures strongly suppresses higher order modes.

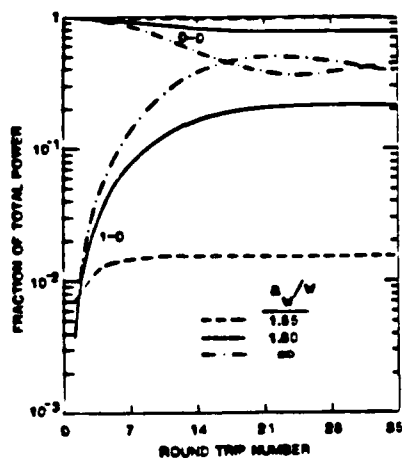


Figure 13. Mode structure for several aperture sizes. $\theta_0 = 20.7^\circ$, 10 percent gain, 9 percent output coupling, $Z_R/Z_R^{eb} = 10$, $L_C/Z_R = 2$.

The diffraction losses, defined as the fraction of the beam power falling outside the mirror radius, actually decrease for the smaller mirror size. The round-trip fractional diffraction loss is 0.0310 for $a_w/w = 1.80$ and 0.0221 for $a_w/w = 1.55$. Apparently there is a finite aperture size for which the diffraction losses are minimized. For the infinite mirror size there is no mode selection, since the output coupling is mode independent. In this case, it is interesting to note that the relative content of 0-0 and 1-0 modes oscillates.

The last variation considered is that of cavity length. As discussed in Sec. III, mode beating in confocal and concentric cavities

has special properties since the round-trip phase slippage between modes is an integer multiple of 2π . This is seen in Fig. 14 where confocal and concentric cavities support large fractions of TEM_{10} mode, but for intermediate cavity lengths the fraction of 1-0 mode decreases dramatically.

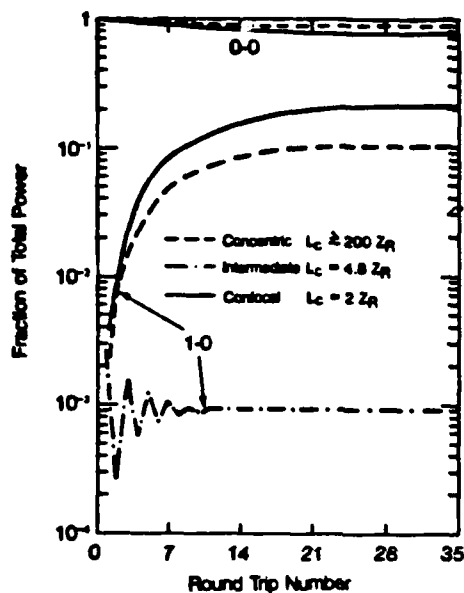


Figure 14. Mode structure for various cavity lengths, $\theta_0 = 20.7^\circ$, $Z_R/Z_R^b = 10$, $a_w/w = 1.80$, $a_m/w = 3$, gain = 10 percent, 9 percent output coupling.

It was shown previously (Fig. 6) that the presence of higher order modes has unusual effects on the intensity distribution within the wiggler. In the case of the concentric cavity, the optical beam, when compared to the fundamental cavity mode, is relatively broad and low intensity where it enters the wiggler. Before exiting the wiggler, the beam then focuses to a relatively narrow, intense waist. This is analogous to the behavior seen on forward passes in the confocal cavity (see Fig. 6). But in contrast to the confocal results, the spot sizes on the two mirrors and the intensity distributions on forward and reverse passes are very similar in the concentric cavity.

The lack of higher order mode content in cavities of intermediate length results from the phase of the 1-0 mode being determined by the

ponderomotive potential, which is formed by the dominant 0-0 mode. Thus, the 1-0 phase is tied to the 0-0 mode, and the 1-0 wave produced on a given round trip is not in phase with 1-0 waves produced on earlier or subsequent round trips in a cavity of intermediate length. A further manifestation of the varying phase relationship between modes is that the intensity distribution on the mirrors, and hence, the cavity losses, are variable from one round trip to another. This results in the ripple seen in Fig. 14.

Nevertheless, a steady mode structure develops which has a constant relative phase between any two modes at any given location on any pass. This is because the production of higher order modes, either by mirror truncation or FEL gain and refraction, always occurs at a constant phase angle relative to the existing pump beam (i.e., coherently). The higher order mode which is produced (say 1-0 mode, for example) will continue to undergo phase slippage relative to the 0-0 mode as it propagates around the cavity. However, it is also gradually attenuated and during its lifetime it has a fixed phase relative to the 0-0 mode at any given location.

Of the three cavity lengths considered, the confocal and concentric cavities have the highest content of higher order modes. The round-trip diffraction losses are also highest for these cavities, as indicated in Table II.

Table II
Round-Trip Aperture Losses for
Various Cavity Lengths

Cavity Length, L_c/Z_R	Round-Trip Fractional Diffraction Loss
≥ 200	0.036
4.8	0.009
2	0.031

These losses pertain to energy passing beyond the edges of the mirrors and energy lost due to aperturing by the wiggler magnet or other elements in the beam line. For the confocal and concentric cases, the loss is about one-third of the output coupling, representing relatively inefficient energy extraction.

V. SUMMARY AND CONCLUSIONS

The transverse structure of the tapered-wiggler FEL optical field has been analyzed by numerical solution of a paraxial wave equation. The optical cavity is initially injected from an external source at its full saturated intensity and the subsequent transverse structure evolution is of interest. Unusual features of the FEL geometry, as compared to conventional lasers, include the narrowness, or more precisely the low Fresnel number of the gain media, the small diameter of the gain media with respect to that of the optical field, and the lack of gain on return passes. These factors tend to produce a steady-state mode structure different from the pure TEM_{00} injected wave.

The higher order mode content is especially evident in confocal and near-concentric optical cavities, i.e., those with mirrors separated by one or two times their radius of curvature. For such cavities, the round-trip phase shift between modes is an integer multiple of 2π , a special situation resulting in constructive addition of higher order modes produced on different round-trips. The presence of higher order modes can significantly affect the photon beam shape, providing unusual effects. For example, in the confocal cavity case, the beam exhibits different radial structure on forward and reverse passes, as well as different spot sizes on the front and rear mirrors. Practical FEL's operating at substantial average power levels are likely to require near-concentric cavities in order to provide sufficiently large spot sizes at the mirrors. In this case, 2π shift occurs between the dominant TEM_{00} and

TEM₁₀ modes in one pass, rather than a round trip, so that spot sizes on the front and rear mirrors and forward and reverse propagating waves differ from those of the fundamental mode but are comparable to each other.

The quality of the output beam is excellent for the cases studied, being of nearly diffraction-limited quality. This result is somewhat surprising in view of the TEM₁₀ mode content which complicates the intracavity structure. This apparent contradiction may be understood by noting that the intracavity wave-front curvature is not matched to that of the fundamental mode of the cavity, while the intracavity beam is essentially diffraction limited.

Additional findings involve the choice of synchronous phase angle, a parameter chosen, within limits, at the discretion of system designers. It is found that for a given electron density, a synchronous phase angle chosen to maximize gain results in much less TEM₁₀ (or higher order) mode production than does a phase angle chosen to maximize the phase shift. In the former case, the e-beam acts as an extended antenna which produces a field much like that already in the cavity, while in the latter case, the e-beam acts like a series of focusing lenses.

A useful application of the techniques described would be analysis of the effects of hole coupling as a means of output coupling in cavities compatible with high average power. Extension of these techniques to include the unbunched nature of electrons entering the wiggler and subsequent oscillation of the phase angle in the ponderomotive potential well, would be useful. A related effect of interest is the slippage of photons relative to electrons when short pulses are considered. In this case, the transverse structure is modified due to reduction of the effective interaction length.

Acknowledgements

The authors wish to thank Dr. D.D. Lowenthal of Mathematical Sciences Northwest, Inc., for several helpful discussions.

This research was supported by AFOSR Contract Number F49620-81-C-0079 and DARPA Contract Number ONR: N00014-80-C-0443.

References

1. D.A.G. Deacon, L.R. Elias, J.M.J. Madey, G.J. Ramian, H.A. Schwettman, and T.I. Smith, Phys. Rev. Lett. 38, 892 (1977).
2. See for example, N.M. Kroll, P.L. Morton, and N.M. Rosenbluth, "Enhanced Energy Extraction in Free-Electron Lasers by Means of Adiabatic Decrease of Resonant Energy," in Physics of Quantum Electronics 7, Editors S.F. Jacobs, H.S. Pilloff, M. Sargent, M.O. Scully, and R. Spitzer, (Addison-Wesley, Reading, Mass., 1980), p. 113.
3. Tapered wiggler verification experiments in progress include those at Los Alamos National Laboratory, Mathematical Sciences Northwest, Inc. and TRW.
4. See for example, W.B. Colson and S.K. Ride, "The Free-Electron Laser: Maxwell's Equations Driven by Single-Particle Currents," in Physics of Quantum Electronics 7, Editors S.F. Jacobs, H.S. Pilloff, M. Sargeant, M.O. Scully, and R. Spitzer, (Addison-Wesley, Reading, Mass., 1980), p. 377.
5. See for example, P. Sprangle and C.M. Tang, Appl. Phys. Lett. 39, 677 (1981), or J. Elliott, "Optical Mode Control in the Free-Electron Laser," in Physics of Quantum Electronics 8, Editors S.F. Jacobs, G.T. Moore, H.S. Pilloff, M. Sargent, M.O. Scully, and R. Spitzer, (Addison-Wesley, Reading, Mass., 1982), p. 531.
6. J.M. Slater and D.D. Lowenthal, J. Appl. Phys. 52, 44 (1981).
7. J.M. Slater, IEEE J. Quantum Electron. QE-17, 1476 (1981).
8. D.B. Rensch, Appl. Opt. 13, 2546 (1974).

9. A.E. Siegman, An Introduction to Lasers and Masers, (McGraw-Hill, New York, 1971), p. 305-330.
10. R.D. Richtmyer and K.W. Morton, Difference Methods for Initial Value Problems, (Interscience, New York, 1967), 2nd Ed., pp. 198-201.
11. M.R. Siegrist, M.R. Green, P.D. Morgan, and R.L. Watterson, Appl. Opt. 19, 3824 (1980).
12. J.P. Blewett and R. Chasman, J. Appl. Phys. 48, 2692 (1977).
13. M. Born and E. Wolf, Principles of Optics, (Pergamon, Oxford, 1970), 4th Ed., pp. 463-464.

APPENDIX D

Scaling of alignment tolerances for free-electron laser oscillators

W. M. Grossman and D. C. Quimby

Mathematical Sciences Northwest, Inc.
2755 Northup Way, Bellevue, Washington 98004

Abstract

Simple scaling laws for free-electron laser oscillator mirror alignment tolerances are given based on geometric optics. The effect of geometric walk-off and diffractive scraping are discussed. In cavities that are nearly concentric, the effect of diffraction can relax the alignment tolerances.

Introduction

Free-electron laser (FEL) oscillator cavities are typically going to be near-concentric; the centers of curvature of the cavity endmirrors will nearly overlap. As will be explained, near-concentric cavities are alignment-sensitive.⁽¹⁾ In designing a FEL cavity, an optical waist extending several meters or more through the wiggler may be desirable for good gain and energy extraction, giving the beam a low far-field divergence. The cavity must be long enough to avoid mirror damage. For a simple two-mirror symmetric cavity, the choice of optical waist parameters and cavity length fixes the required radius of curvature of the end mirrors. The alignment sensitivity of this cavity is found by determining when mis-alignments degrade performance. Degradation may be due to loss of electron-beam/optical-beam overlap, off-axis optical aberration, or losses at apertures defined by the wiggler bore, the mirror size, or a scraping outcoupler. In the analysis to follow, the scaling of alignment sensitivity with FEL parameters will be found based on the effects of electron-beam/optical-beam overlap or losses at apertures.

Length requirements and cavity design

The cavity design for a FEL oscillator is constrained by the choices of optical power, wavelength, and the efficiency of the laser. Large electron-beam energy extraction is needed for high efficiency. For large extraction, high peak optical intensities are needed at a long optical waist in the wiggler for the duration of the electron-beam micropulse. The length of the waist region is described in terms of the Rayleigh range, Z_R , the distance over which a Gaussian beam radius grows by a factor of $\sqrt{2}$. A Rayleigh range chosen to optimize laser performance is typically from $1/2$ to $1/4$ the wiggler length. Larger wigglers tend to give superior laser performance but at increased wiggler cost, at possibly increased electron-beam steering difficulty in the wiggler, and as shown later, at increased cavity length to avoid mirror damage. Rayleigh ranges, in present experiments, vary from 0.1 to 1m , and may be considerably larger in advanced oscillator designs. Choosing the Rayleigh range and wavelength determines the shape of an unaberrated freely-propagating Gaussian beam diverging from a waist.

The minimum cavity length, L , is computed below based on the requirement that the optical beam radius at the endmirror be large enough to keep the optical flux below the damage or degradation limits of the mirror. A simple two-mirror cavity will be considered, as shown in Figure 1. Mirror alignment tolerances will be derived subsequently using this analysis, and the tolerances will be shown to hold even if the cavity is shortened using a high flux intracavity beam expander, such as with glancing incidence optics. To avoid damage or

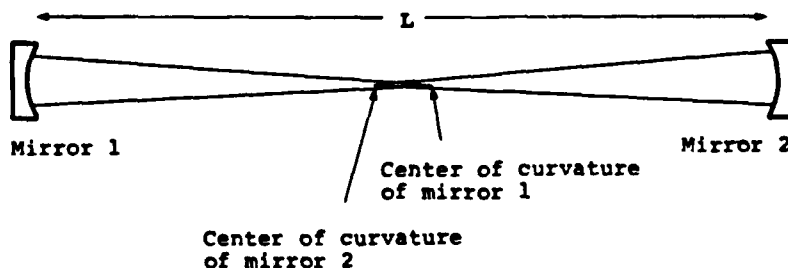


Figure 1. FEL cavities are near-concentric and alignment sensitive.

degradation of the endmirrors, which are assumed to be used at normal incidence, the beam radius, ω , at the endmirror must often be far larger than at the waist. The constraint is that the flux or power density be less than the damage or degradation limit

$$\pi\omega^2 > 2\Gamma/\Phi_D, \quad (1)$$

where Γ is either the average power or single-pulse integrated energy exposure within the cavity, whichever is damage limiting; Φ_D is the damage limit for either power density (W/cm^2) or for single-pulse integrated energy density (J/cm^2), whichever is damage limiting. At a distance $L/2$ (half the cavity length) from the centered beam waist, the beam radius is (2)

$$\omega = L\omega_0/2Z_R \quad (2)$$

for $L \gg Z_R$. The wavelength, λ , Rayleigh range, Z_R , and radius at the waist, ω_0 , are related by (2)

$$\pi\omega_0^2 = \lambda Z_R. \quad (3)$$

Using Equations 1, 2, and 3, the minimal cavity length set by damage

$$L > \left(\frac{8\Gamma Z_R}{\lambda\Phi_D} \right)^{1/2}. \quad (4)$$

The result of the previous analysis is that a cavity may tend to be very long. For example, consider a pulsed oscillator with 30 ps micropulses, and 10^4 micropulses in a macropulse. If the circulating peak power is 5 GW, Z_R is 1m, λ is $0.5\mu m$, and the macropulse damage limit on a coating is taken as $10 J/cm^2$ (which may be conservative for very long pulses but is above typical for short pulse limits) then the total flux, Γ , is $10^4 \times 30 \text{ ps} \times 5 \text{ GW} = 1.5 \text{ kJ}$ and the required cavity length would be about 500m. This cavity length is many Rayleigh ranges long, and average power requirements could lengthen it further.

The radius of curvature of the mirrors is designed to match the optical wavefront curvature for a self-replicating Gaussian wavefront. (2) For a free-electron laser, this is a good approximation but is not exactly true. (3) The radius of curvature, R , of the wavefront at the cavity endmirror is given by

$$R = \left[\frac{L}{2} \right] \left[1 + \frac{Z_R^2}{[L/2]^2} \right]. \quad (5)$$

When Z_R is small compared to the cavity length

$$Z_R \ll L/2, \quad (6)$$

then Equation 5 reduces to

$$R = L/2. \quad (7)$$

Alignment tolerance scaling using geometric optics

Near-concentric cavities are highly alignment sensitive because their geometric axis, defined by the line joining the centers of curvature of the two endmirrors, undergoes highly leveraged tilting when either endmirror is tilted. This is shown in Figure 2 where the cavity mirror to the right has been tilted by an angle θ , and the optical axis is tilted by an angle ϕ . The optical axis shown is almost cut by apertures at the ends of the wiggler and is misaligned. If the Rayleigh range is much less than the cavity length, the centers of curvature of the mirrors are spaced by far less than the wiggler length, and the optical axis can be considered to pivot about the middle of the wiggler. The alignment tolerances on the endmirrors can be defined by requiring the optical axis stay within some fraction of

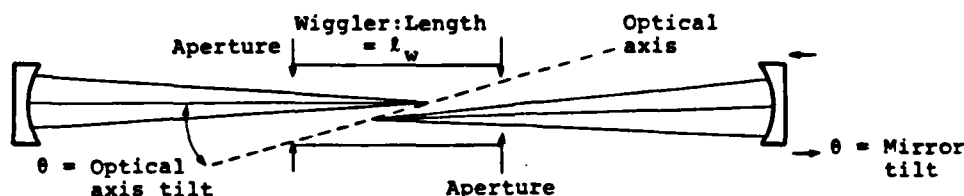


Figure 2. Near-concentric resonators are alignment sensitive.

ω_0 ($\omega_0/3$) is used here) of the wiggler axis at the wiggler ends, thus preserving electron beam overlap and eliminating losses at the apertures. The tolerance is

$$\phi \frac{l_w}{2} < \frac{\omega_0}{3}, \quad (8)$$

where l_w is the length of the wiggler and ω_0 is again the beam radius at the waist. From Equations 5 and 7, it is apparent that the mirror centers of curvature are displaced from the cavity center by $2Z_R^2/R$, so that the mirror tilt (θ) and the optical axis tilt (ϕ) are related by

$$\theta R = \phi \left[\frac{2Z_R^2}{R} \right]. \quad (9)$$

Assuming the wiggler length is about two Rayleigh ranges:

$$l_w = 2Z_R. \quad (10)$$

Then a tolerance on θ can be found in terms of Z_R , λ , ϕ_D , and Γ for a cavity where the length (L) is the minimum allowed to avoid mirror damage. Using Equations 4 and 7 to eliminate P and L from Equation 9, and Equations 3 and 10 to eliminate ω_0 and l_w from Equation 8, the tolerance on mirror tilt is:

$$\theta < \frac{Z_R^{1/2} \lambda^{3/2} \phi_D}{3\pi^{1/2}\Gamma}. \quad (11)$$

This is the main scaling equation for alignment tolerances based on geometric optics. The mirror alignment sensitivity is seen to be tightened at short wavelengths, short Rayleigh ranges, and at higher powers or energies.

The tolerance on alignment is derived using geometric, or ray, optics. The tolerances do not change if a telescope is inserted between the wiggler and the endmirror in order to shorten the cavity. The same endmirrors would be used, having the same radius of curvature and area. The alignment sensitivity depends only on the allowed tilt for the optical axis, the relative location of the centers of curvature of the two mirrors, and the degree to which the mirror centers of curvature are displaced when the mirrors are tilted. To first order, the allowed tilt of the optical axis is unchanged by use of a telescope, and the distance between the centers of curvature of the two mirrors is also unchanged. As shown in Figure 3, the lateral displacement of the center of curvature of a mirror, when that mirror is tilted, is also unchanged by a beam expander because a magnification, m , in image size corresponds to demagnification, $1/m$, in angle. The lateral displacement is given by the radius of curvature multiplied by the angle through which it is tilted. As the cavity length is demagnified, the angle is magnified and the displacement does not change with magnification.

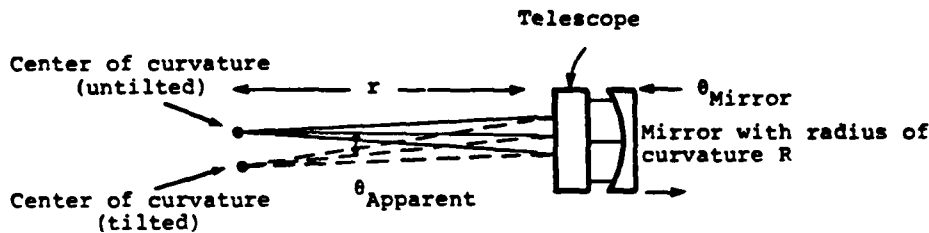


Figure 3. Intracavity telescopes do not affect the first order alignment tolerances because a given tilt, θ , on a mirror with radius of curvature R results in the same displacement of the mirror center of curvature (θR) with or without a telescope.

Diffractive effects

For the example cited earlier of $Z_R = 100$ cm, $\lambda = 0.5 \times 10^{-4}$ cm, $\phi_D = 10$ J/cm², and $\Gamma = 1.5$ kJ, the alignment tolerance using Equation 11 is about 4 nrad. The diffraction limit of the mirror is roughly equal to the wavelength of the light divided by the mirror diameter. The diameter is about four times the beam radius at the mirror and using Equation 1, the radius is about 11 cm. The diffraction limit on pointing is about 1 μ rad, over two orders of magnitude larger than the alignment tolerance. To sense such a tight tolerance, the beam must circulate many times in the cavity.

If the optical beam actually falls on the geometric optical-axis, then the alignment tolerance given by Equation 11 is valid. However, if a ray aligned to the wiggler axis, but misaligned to the cavity axis takes many cavity round trips before seeing the losses associated with the misalignment, then diffractive effects may cause the true optical axis, defined by the intensity centroid, to be displaced from the geometric axis. To calculate how long it takes an off-axis ray to locate the geometric axis, consider the situation shown in Figure 4. An off-axis ray is circulating paraxially in a near-concentric bare

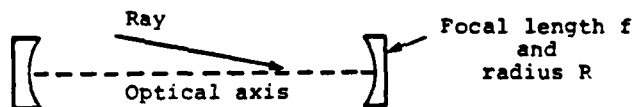


Figure 4. An off-axis ray propagating paraxially in a near-concentric cavity.

cavity. The mirror radius of curvature, R , is related to its focal length, f , simply by

$$R = 2f. \quad (12)$$

And for a near-concentric cavity

$$R = \frac{L}{2} (1 + \epsilon), \quad (13)$$

where

$$\epsilon = \frac{4Z_R^2}{L^2} \ll 1. \quad (14)$$

Again L is the cavity length. An off-axis ray in the cavity can be described by a vector, r ,

$$r = \begin{bmatrix} x \\ x' \end{bmatrix} \quad (15)$$

where x is the transverse position of the ray and x' is the transverse angle. Propagating this ray paraxially can be modeled by operating on the ray with the matrix, M , for a cavity round trip.

$$M = \left[\begin{bmatrix} 1 & L \\ 0 & 1 \end{bmatrix} \begin{bmatrix} -1 & 0 \\ -1/f & 1 \end{bmatrix} \right]^2 = \begin{bmatrix} -3 + 4\epsilon & 4f(1-\epsilon) \\ -1/f & 1 \end{bmatrix}. \quad (16)$$

By examining the action of this matrix on eigenvectors, it can be found that in the limit of large n

$$M^n r = \frac{(-1)^n}{2\sqrt{\epsilon}} \sin(-2\sqrt{\epsilon} n) (M + I)r, \quad (17)$$

where I is the identity matrix. The number of cavity round trips, n , needed for a ray to self-replicate is therefore given by

$$2\sqrt{\epsilon} n = 2\pi, \quad (18)$$

or

$$n = 1.5L/Z_R. \quad (19)$$

The ray can be said to find the axis in roughly half this number of passes. Geometrically it takes L/Z_R round trips for a ray to find the axis. Diffractive beam steering may be important if L/Z_R is very large because many diffractive cuts occur prior to large intensity loss. These effects were studied using a diffractive analysis of wavefront propagation in a near-concentric cavity.

A model of wavefront propagation in a near-concentric gain-free FEL cavity was used to determine alignment sensitivity. In the test case shown, the cavity is 500 Rayleigh ranges long, the wiggler 3 Rayleigh ranges long, and the wiggler bore $4w$ at the exit. The Rayleigh range is $1m$. Optical propagation is modeled using a fast Fourier transform expansion of the wavefront into a series of plane waves traveling at different spatial angles.⁽⁴⁾ A TEM_{00} wave is injected into the cavity and one mirror is suddenly tilted. The diffractive loss due to clipping at each end of the wiggler is calculated and evolution to a steady mode structure is observed. For the best test case shown in Figures 5 and 6,

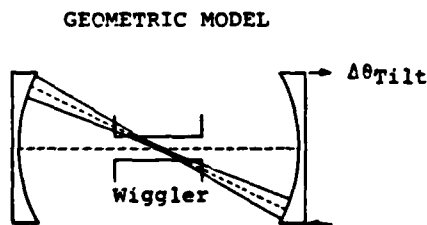


Figure 5. Geometric picture of the case studied to determine diffractive effects. The cavity was misaligned so that the optical axis was upon the aperture and losses were near 100 percent.

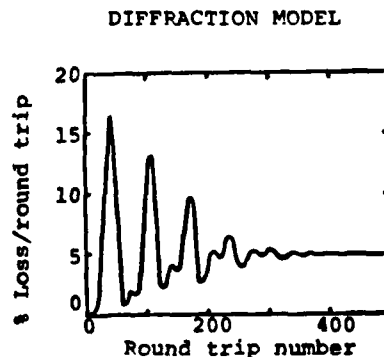


Figure 6. Optical losses per round trip for the case shown in Figure 3.

A_0 was 55 nr, enough to put the geometrical optical axis onto the aperture at the wiggler, and create ~100 percent loss per pass. The losses computed are far lower, equilibrating at about 5 percent per round trip. Consequently, the alignment tolerance defined by the geometric analysis is far too tight. This is true in just the cases when L/Z_R is very large, perhaps 10^2 or greater. Even so, the tolerances are still far tighter than the diffraction limited pointing tolerance. This is possible because the laser resonator, like an etalon, allows the optical beam to sample the mirror surface many times over many round trips, and more finely sense misalignment. Diffractive effects are caused by the beam being cut by apertures at the edge of the beam where the fields are lower, and the intensity which is proportional to the square of the field, is lower still. The cutting can steer the beam without severe losses. The optical axis is then not located where the geometric analysis would predict.

Conclusions

The alignment tolerances for a FEL scillator built to the minimal length allowed by optical damage scale roughly as $Z_R^{1/2} \lambda^{1/2} (\Phi_D/\Gamma)$ where Z_R is the Rayleigh range, λ is the wavelength and Φ_D/Γ is proportional to the reciprocal of the mirror area required to avoid optical damage due to energy or average power effects. Short wavelength, high power FFL oscillators will have the most demanding alignment requirements. In near-concentric FEL cavities which are many Rayleigh ranges long, the geometrically derived tolerances may be overly tight and diffractive scraping at apertures will act to keep the beam along a lower loss axis. The alignment sensitivity of these cavities is always comparable to, or tighter than, the diffraction-limited pointing accuracy.

Acknowledgment

The authors gratefully acknowledge the advice and motivation provided by Jack Slater. The work was supported by ONR Contract Number N00014-82-C-0704.

References

1. For a general treatment of alignment sensitivity based on geometric optics, see P. Hauck, H.P. Kottz, and H. Weber, Appl. Opt., Vol. 19, p. 598 (1980).
2. A.E. Siegman, An Introduction to Lasers and Masers, McGraw-Hill, New York (1971).
3. D.C. Quimby and J. Slater, IEEE J. Quantum Electron., Vol. QE-19, p. 800 (1983).
4. E.F. Sziklas and A.E. Siegman, Appl. Opt., Vol. 14, p. 1874 (1975).

APPENDIX E

PUBLICATIONS AND PRESENTATIONS

Scientific publications directly resulting from this contract include:

1. D.C. Quimby and J.M. Slater, "Transverse Mode Structure of a Tapered-Wiggler FEL Oscillator," in Proceedings of the International Free-Electron Laser Conference, Bendor, France, September 27 - October 1, 1982, J. de Physique, 44, p. C1-397 (1983).
2. D.C. Quimby and J.M. Slater, "Mode Structure of a Tapered-Wiggler Free-Electron Laser Stable Oscillator," IEEE J. Quantum Electron., QE-19, pp. 800-809 (1983).
3. J.M. Slater, J. Adamski, D.C. Quimby, W.M. Grossman, T.L. Churchill, and R.E. Center, "Tapered-Wiggler Free-Electron Laser Demonstration," in the Proceedings of the International Conference on Lasers '82, New Orleans, LA, December 15-17, 1983, R.C. Powell, ed., McLean, VA: STS Press, 1983, pp. 212-217.
4. W.M. Grossman, J.M. Slater, D.C. Quimby, T.L. Churchill, J. Adamski, R.C. Kennedy, and D.R. Shoffstall, "Demonstration of Large Electron-Beam Energy Extraction by a Tapered-Wiggler Free-Electron Laser," Appl. Phys. Lett., 43, pp. 745-747 (1983).
5. W.M. Grossman, T.L. Churchill, D.C. Quimby, J.M. Slater, J. Adamski, R.C. Kennedy, and D.R. Shoffstall, "Demonstration of Large Electron-Beam Energy Extraction by a Tapered-Wiggler Free-Electron Laser," in Free-Electron Generators of Coherent Radiation, C.A. Brau, S.F. Jacobs, and M.O. Scully, eds., Proc. Soc. Photo-Optical Instrum. Engrs., 453, pp. 51-58, 1984.

6. D.C. Quimby and J.M. Slater, "Electron-Beam Quality Requirements for Tapered-Wiggler Free-Electron Lasers," submitted to IEEE J. Quantum Electron., April 1984.
7. D.C. Quimby, J.M. Slater, and J.P. Wilcoxon, "Suppression of the Sideband Instability in Long, Highly-Tapered Free-Electron Lasers," to be submitted to IEEE J. Quantum Electron.
8. D.C. Quimby, "Transverse Mode Structure in Free-Electron Lasers," a review to be presented at the International Free-Electron Laser Conference, Castelvandologo, Italy, September 3-7, 1984.

Additional unpublished conference presentations include:

1. J.M. Slater, D.D. Lowenthal, and D.C. Quimby, "Wiggler Design and Diffraction Effects in the Tapered-Wiggler Free-Electron Laser," presented at the International Conference on Lasers, '80, New Orleans, LA, December 15-19, 1980.
2. J.M. Slater, "MSNW Tapered-Wiggler FEL Program," presented at the Office of Naval Research Workshop on Free-Electron Lasers, Sun Valley, ID, June 22-25, 1981.
3. J.M. Slater, "MSNW Tapered-Wiggler FEL Program," presented at the Office of Naval Research Program Review, Santa Barbara, CA, March 15-16, 1982.
4. D.C. Quimby and J.M. Slater, "Analysis of Free-Electron Laser Mode Structure," presented at the Conference on Lasers and Electro-Optics, '82, Phoenix, AZ, April 14-16, 1982.

5. J.M. Slater, J. Adamski, R.C. Kennedy, J.M. Eggleston, and D.C. Quimby, "Boeing-MSNW FEL Program," presented at the Free-Electron Laser Program Kickoff Meeting, Los Alamos, NM, January 30 - February 1, 1984.

Additional publications related to development of the models and experiments used in this contract include:

1. J.M. Slater and D.D. Lowenthal, "Diffraction Effects in Free-Electron Lasers," J. Appl. Phys., 52, pp. 44-47 (1981).
2. J.M. Slater, "Tapered-Wiggler Free-Electron Laser Optimization," IEEE J. Quantum Electron., QE-17, pp. 1476-1479 (1981).
3. D.C. Quimby, "Floating Wire Measurement of Transverse Magnetic Field Errors in a Planar Free-Electron Laser Wiggler," J. Appl. Phys., 53, pp. 6613-6619 (1982).
4. J.M. Slater, J., Adamski, D.C. Quimby, T.L. Churchill, L.Y. Nelson, and R.E. Center, "Status of the MSNW Tapered-Wiggler FEL Experiment," in Proceedings of the International Free-Electron Laser Conference, Bendor, France, September 27 - October 1, 1982, J. de Physique, 44, pp. C1-73 through C1-83 (1983).
5. J.M. Slater, J. Adamski, D.C. Quimby, T.L. Churchill, L.Y. Nelson, and R.E. Center, "Electron Spectrum Measurements for a Tapered-Wiggler Free-Electron Laser," IEEE J. Quantum Electron., QE-19, pp. 374-379 (1983).
6. W.M. Grossman and D.C. Quimby, "Scaling of Alignment Tolerances for Free-Electron Laser Oscillators," in Free-Electron Generators of Coherent Radiation, C.A. Brau, S.F. Jacobs, and M.O. Scully, eds., Proc. Soc. Photo-Optical Instrum. Engrs., 453, pp. 86-91, 1984.

7. D.C. Quimby and J.M. Slater, "Emittance Acceptance in Tapered-Wiggler Free-Electron Lasers," in Free-Electron Generators of Coherent Radiation, C.A. Brau, S.F. Jacobs, and M.O. Scully, eds., Proc. Soc. Photo-Optical Instrum. Engrs., 453, pp. 92-99, 1984.

END

FILMED

9-84

DTIC